The Dissertation Committee for Chao Liu Certifies that this is the approved version of the following dissertation:

Precision Manipulation of Organic and Inorganic Nanoentities for Enhanced Optical Biodetection at Deterministic Positions

Committee:

Donglei (Emma) Fan, Supervisor

Paulo J. Ferreira

Charles Buddie Mullins

Jianshi Zhou

Arumugam Manthiram

Precision Manipulation of Organic and Inorganic Nanoentities for Enhanced Optical Biodetection at Deterministic Positions

by

Chao Liu, B.E.; M.E.

Dissertation

Presented to the Faculty of the Graduate School of

The University of Texas at Austin

in Partial Fulfillmentz

of the Requirements

for the Degree of

Doctor of Philosophy

The University of Texas at Austin
May 2016

Dedication

To my loving family for the love and support throughout my study

Acknowledgements

The first person I would like to thank is my supervisor, Prof. Donglei Fan, for all the guidance, insights, and opportunities she has provided for me throughout my graduate career. It is remarkable to reflect on how much I have learned during the past five years. Thanks for being so patient to teach me how to be an excellent researcher. From you, I learnt that the right attitude is the key to make research work. Thanks for exposing me to so many wonderful projects, which I really enjoyed working on. Looking back to my graduate career, I am very grateful to be your student. I would also like to thank Prof. Paulo J. Ferreira, Prof. Charles Buddie Mullins, Prof. Jianshi Zhou and Prof. Arumugam Manthiram, for agreeing to serve on my committee, and providing valuable advice on my proposal and dissertation.

There are dozens of Fan group members who deserve recognition for their contributions to my success. I am indebted to Xiaobin Xu and Kwanoh Kim, who did not only teach me how to synthesize nanowires, nanocapsules, and fabricate microelectrodes at the beginning of my Ph.D. study, but also worked as great partners for the rest five years. I would like to thank Jianhe Guo who works closely with me; Wesker Lei who taught me how to assemble quantum dots in a large array. I also want to express my gratitude to the current and previous members of Fan group, including Jing Ning, Weigu Li, Zexi Liang, Jiawei He, Kipyo Hong, Jing Liu, Tao Liu and Guilan Feng. It is a great pleasure to work with you all during my study.

I would also like to thank all of my collaborators: Dr. Yufeng Hao who helped me to build my CVD furnace at the beginning of my Ph.D. study; Dr. Jim Werner and his group at Los Alamos National Laboratories for the collaboration on single quantum dot tracking experiments; Prof. Alan Wang and his group at Oregon State University for the optical simulation of our photonic crystal substrates and nanocapsules; Prof. Ray T. Chen and his group for the collaboration on optical devices; Prof. Charles Buddie Mullins and his group for the collaboration on water splitting project; and Prof. Arumugam Manthiram and his group for the collaboration on energy devices. I am also indebted to my fellows: Kwanoh Kim, Jing Ning, Jianhe Guo, Xiaobin Xu, Zheng Wang, and Longjun Li. Your dedicated collaboration and friendship are very important to my life and career.

I also own thanks to the research scientists in CNM and TMI for helping me with the cleaning room procedures, instrument trainings, material synthesis and characterizations along my study: Dr. Shouliang Zhang for SEM and STEM, Dr. Damon Smith for cleaning room training, Dr. Joshua Bolinger for AFM and UV-vis absorption spectroscopy trainings.

There are none more deserving of thanks than those who work behind the scenes to make my research smooth: Prof. Desiderio Kovar for his great advising to keep me on the right track since I started my study; Rebecca Christian, Bonnie Stewart-Richlen and Liz Myrick for making sure my registration, appointment and paperwork always in order; Joan Haddena and Lindsay Murphy for helping me to place orders and making sure they arrived on time.

I would like to thank my master degree advisor, Dr. Haiping He at Zhejiang University, who introduced me to the academia and encouraged me to study abroad. Last, but most importantly, I would like to thank my family and friends for their love, support and encourage over the years, making me the person I am today.

Precision Manipulation of Organic and Inorganic Nanoentities for Enhanced Optical Biodetection at Deterministic Positions

Chao Liu, Ph. D.

The University of Texas at Austin, 2016

Supervisor: Donglei (Emma) Fan

In the last decade, considerable research interests are focused on applying semiconductor quantum dots (QDs) for bioimaging, sensing, and therapeutic delivery. Compared to traditional organic dyes, semiconductor QDs exhibit higher fluorescent brightness, better resistance to photo-bleaching, tunable sizes/colors, wider absorption peak and larger stokes shifts. However, the applications of QDs as biosensors are still largely conducted in bulk colloidal suspensions, which present considerable difficulties in sensing a minute amount of bioanalyte. It is highly desirable if the QDs can be registered at designated locations for position-predicable optical analysis and sensing.

Raman scattering spectroscopy has been utilized to unambiguously identify molecules based on their intrinsic vibrational "fingerprint" states. However, due to the relatively small Raman scattering cross-section, the intensity of Raman signal is usually $1/10^6$ of that of Rayleigh scattering. The recent discovery of Surface enhanced Raman scattering (SERS) dramatically improves the Raman signal and rejuvenates this field. An

enhancement factor (EF) as high as 10^{12} have been reported, which can readily detect various single molecules, essential for early-stage disease detection, warfare agent detection, environmental pollutant detection, and biomolecule detection. However, SERS substrates with such high EF usually suffer from reproducibility and uniformity issues. Moreover, SERS detection is still largely conducted in a seek-and-find manner which substantially limits the detection efficiency. Most SERS detections are carried out by drying analyte solutions on SERS substrates to force molecules to attach to hotspots before the detection. The employed drying methods can be different among individual research groups. Quantitative comparison of these results should be conducted carefully. It is highly desirable to directly detect molecules in suspension to accurately evaluate the performances of different SERS substrates. However, when directly measuring SERS signals of molecules in suspension, due to the inefficient diffusion based binding process, much less molecules can closely interact with hot spots compared to those on dried SERS samples. As a result, direct SERS detection from suspension can often be less sensitive by a few orders of magnitudes compares to those in dried condition. It is of great interest to investigate new mechanisms to detect analyte molecules directly from analyte solutions with high sensitivity.

In this research, I rationally designed and synthesized various types of nanostructures, including ZnO, Si, and Au nanowires, ZnO nanosuperstructures, and hybrid nanocapsules. Such materials have unique optical/plasmonic properties and could be used in various applications, particularly in biochemical sensing. Two types of optical

nanobiosensors have been designed, fabricated, characterized, and investigated. They are fluorescence-based QD-on-nanowire assemblies and SERS-photonic-crystal hybrid nanosensors. The QD-on-nanowire florescent nanosensors operated uniquely by focusing analyte molecules to the assembled QDs on tips of nanowires before detection via specific biochemical conjugation. Molecules, such as biotin, can be revealed unambiguously in a location deterministic manner with substantially enhanced sensitivity. In the development of SERS-photonic-crystal hybrid nanosensors, two enhancement mechanisms, including guided-mode resonance (GMR) and electrokinetic effect, were studied and applied in improving the sensitivity and efficiency of molecule detection, respectively. Such a hybrid device has been proposed and studied for the first time, which can readily improve the detection sensitivity by a robust 4-5 times in addition to the 10^9-10^{10} SERS enhancement. This dissertation work, exploring innovative materials design, synthesis, and manipulation, has made an important forward step in the next-generation biochemical detection platform.

Table of Contents

List of Figures

List of Illustrations

Chapter 1: Introduction*

In this dissertation, I focus on the fabrication of various nanostructured materials, such as semiconductor and metallic nanowires, highly branched nanosuperstructures, and designed composite nanocapsules and the manipulation and assembling of these nanostructures for applications in biochemical detection with optical spectroscopies.

1.1 FLUORESCENCE QUANTUM DOT BASED BIODETECTION

Fluorescence-based detection method is widely used in biosensing and bioimaging areas due to high detection efficiency, simple experimental procedure, and high detection accuracy. Such detection method heavily relies on the availability of sensitive and bioselective fluorescent probes. Fluorescent molecules, proteins, and dyes, which are widely used as the fluorescent probes have their own drawbacks, including susceptibility to environmental changes and photobleaching, short Stokes shifts, narrow absorption peaks and broad emission bands. In contrast, semiconductor nanocrystals (quantum dots, QDs) provide unprecedented photophysical properties[1]. Due to the quantum confinement effect, colors of QDs can be systematically tuned from the visible to infrared optical regime by varying the sizes and material compositions. The quantum yield of QDs are usually higher than other chemical fluorophores which makes them brighter. Moreover, the photostability of QDs is much better due to the core/shell structures which makes it more chemical-resistant. In addition, the wide absorption band and large Stokes shifts of QDs make it

---

*Portions of this chapter have been previously published in X. Xu, K. Kim, C. Liu, D.L. Fan, Sensors, 15, 10422-10451, (2015) possible to stimulate QDs of different colors simultaneously by a single excitation source, which can be used for optical barcoding of biomolecules[2]. These unique properties are applied for imaging and tracking extracellular events, including cellular motility[3], protease activity[4], and signal transduction[5]. They were also applied as nanosensors for detection of viruses[6], cytokines[7], and pH variations[8].

1.1.1 Quantum Dot Biosensing Mechanisms

When QDs are applied as biosensors, the transduction scheme involves the energy flows between different sensing components. Depending on how to generate the initial excitation energy for the energy flow, the sensing mechanism can be categorized as Föster resonance energy transfer [also called fluorescence resonance energy transfer (FRET)] and bioluminescence resonance energy transfer (BRET).

1.1.1.1 Föster Resonance Energy Transfer Mechanism (FRET)

Föster resonance energy transfer is a non-radiative transition of energy from a donor to an acceptor that is in its close proximity. The FRET efficiency depends on the distance between the donor and the acceptor, typically in the range of 1-10 nm, the relative orientation between donor and acceptor dipole moment, as well as the spectral overlap of the donor emission with the acceptor absorption. The FRET efficiency (E) can be given as[9]:

$$E = \frac{1}{1+(\frac{r}{R_0})^6} \qquad 1.1$$

where R_0 is the Föster distance at which FRET efficiency is 50%, and the FRET efficiency depends on the extent of overlap between donor emission and the acceptor absorption; r is the actual donor-acceptor distance. This equation indicates that the FRET efficiency is inversely proportional to the sixth power of the distance between the donor and the acceptor.

Since the first demonstration of the energy transfer from QDs to organic chromophores[10], QDs have proved to be an excellent type of donors in the FRET system due to a high quantum yield, a broad absorption band and a narrow emission peak. While, QDs performance complicatedly when they serve as acceptors. When exciting donors, there is a co-excitation of QD acceptors due to the broad absorption band, which could complicate the analysis of the FRET efficiency.

QDs-based FRET systems have been extensively studied as pH probes[11], metal ion sensors[12], and organic compound detectors. The first ratiometric QDs-based FRET pH sensor was developed by Snee[11]. This system was built on the CdSe/ZnS QDs encapsulated by a hydrophobically modified poly-(acrylic acid) which is conjugated to a pH-sensitive squaraine dye. The signal transduction is based on the energy flow from the QDs to squaraine dyes and the FRET efficiency is modulated by engineering the pH-sensitive dye absorption spectrum. Due to the pH dependence of the dye absorption spectrum, the spectral overlap between the dye absorption and the QD emission increases as the pH decreases which indicates in the fluorescence spectra that the emission from dyes increase as the emission from QDs decreases. This ratiometric approach is much superior to other typical chemo- and biosensors which only display a single intensity-based response to analytes because sensing is self-calibrated. Recently, Dennis[13] developed a QDs-fluorescence protein-based pH sensor for intracellular pH monitoring. In this system, the QDs are linked to pH sensitive proteins which are either mOrange or its homologue mOrange M163K. These protein response to the pH changes uniquely by changing both the intensity and wavelength of the emission peak and absorption peak. In the base solution, when the pH value decreases, the acceptor to donor emission ratio increases. The emission intensity ratio between fluorescence protein and QDs larger than 12 folds can be achieved within the pH region from 6 to 8. By modifying the fluorescence protein, they were able to monitor the acidification of endosomes in living cells following polyarginine-mediated uptake which sheds light on intracellular image and biosensing.

Some of the metal ions are environmental hazards and detrimental to the human health. Many groups investigate the feasibility of applying QDs-based FRET to detect the metal ion. When the metal ion such as Cu^{2+}, Ag^{+}, Hg^{2+}, Fe^{2+}, or Pb^{2+} approaches to the QDs, the emission of the QDs is passively quenched through non-radiative recombination path. As a result, the detection of metal ion based on QDs is non-specific and impractical. Despite this, Li[12a] created the QDs-based FRET system to detect Hg^{2+} ion. In their system, CdTe QDs donor linked to the butyl-rhodamine B (BRB) (acceptor) with an assistant of cetyltrimethylammonium bromide (CTAB) which helps to enhance the bond between QDs and BRB as well as improves the FRET efficient. Upon the introduction of Hg^{2+} ions, the emission intensity of QDs and BRB are both quenched. However, the emission intensity of BRB decreases much greater than that for QDs. The possible signal transduction mechanism is due to the chemical displacement of Cd^{2+} by Hg^{2+} on the QDs surface which consequently quenches both QDs and BRB. In order to protect QDs and eliminate the quenching effect from the metal ions, Liu[12b] innovatively designed a robust FRET-based ratiometric senor system by using the reverse microemulsion approach. The CdTe QDs were embedded in silica spheres and a positive charged space layer was coated outside which prevents the Hg^{2+} ion contacting the inside QDs. The final touch of this design is the spirolactam rhodamine which can be turned on and off by Hg^{2+} ion as the acceptor or inert dye. This method can also be applied to detect other metal ion.

1.1.1.2 Bioluminescence Resonance Energy Transfer Mechanism (BRET)

Bioluminescence resonance energy transfer is a non-radiative energy transfer process which resembles FRET in many aspects except that the external light source is not required to excite donors. Instead, a donor is excited by a biochemical reaction. Usually, the donor is a light emitting enzyme which catalyzes the oxidation of its substrate. The energy transfer efficiency is inversely proportional to the sixth power between a donor and an acceptor which is similar to FRET. The BRET is mostly applied to sense the proteolytic activity of proteases. Xia[14] implemented the intein-mediated nanoconjugation chemistry, successfully linked the bioluminescent protein Luc8 to the QDs via a protease peptide substrate. Once the matrix metalloproteinase (MMP) was added to the medium, it cleavages the link between Luc8 and QDs, and result in the releasing of the QDs and decreasing of the BRET ratio. This QDs-based BRET sensing platform have successfully demonstrated the detection of MMP-7 activity in buffer and Serum; furthermore, by varying the peptide substrate, other proteases can be detected in a similar manner including MMP-2 and urokinase-type plasminogen activator (uPA). Since the QDs have a broad absorption peak, the platform can detect multiple proteases. For example, multiplex detection of MMP-2 and uPA have been accomplished.

Compared to FRET, BRET does not require an external light source to excite the donor which eliminates the autofluorescence effect in biological samples and dramatically increase the signal to noise ratio. Hence, BRET has been employed in the bioimaging area to monitor protein-protein interactions[15], tracking labelled cells[16].

However, the applications of QDs as biosensors are still largely conducted in bulk colloidal suspensions, which presents considerable difficulties in sensing a minute amount of bioanalyte. In Chapter 3, we investigate controllable manipulation and assembling of

QD-nanowire hybrid nanostructures in suspension by electric fields and applied the assemblies for the location deterministic biochemical detection. This method could be a critical step towards a rational bottom-up approach for fabricating various QD-based biomedical devices

1.2 SURFACE ENHANCED RAMAN SCATTERING

When light shines on atoms or molecules, most photons are elastically scattered, which means that the scattered photons have the same frequency as the incident light, i.e., $\nu_{\text{incident}} = \nu_{\text{scattered}}$. This phenomenon is called elastic Rayleigh scattering. However, as discovered by the Nobel Prize laureate, Dr. Venkata Raman, there is a small fraction of light that undergoes inelastic scattering (~1/1,000,000 or less), which gains or loses energy due to the absorption or release of quantized vibrational or rotational molecular energy as shown in Figure 1.1. This effect is the so-called Raman scattering.

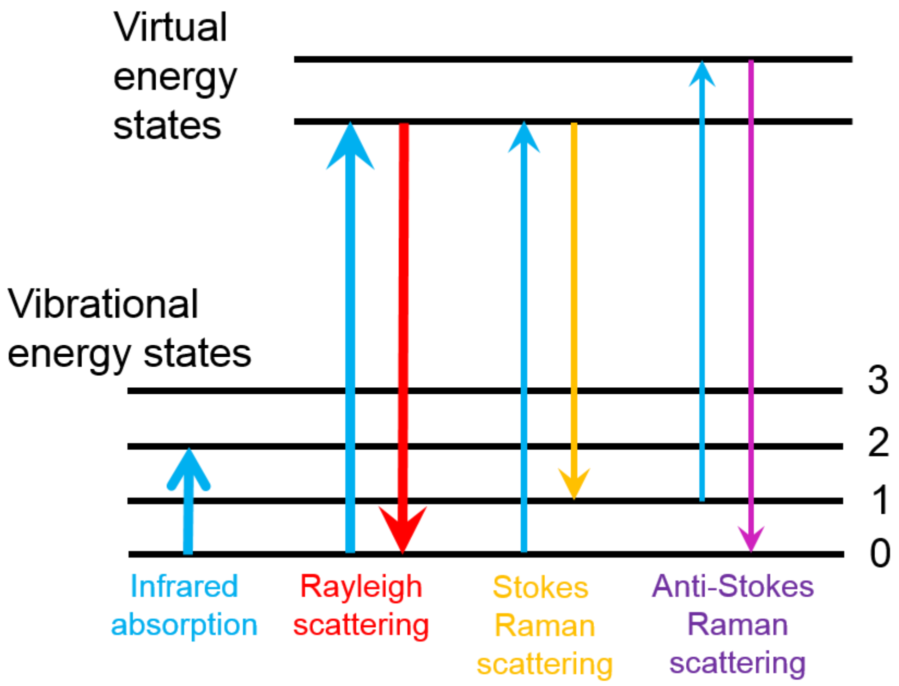

Figure 1.1: Diagram of energy band of Raman scattering.

It has been over 40 years since 1973 that Fleischmann et al., first observed the substantial enhancement of Raman scattering spectrum of sub-monolayer pyridine molecules on electrochemically roughened silver (Ag) electrodes[17]. Four years later, in 1977, two research groups independently reported that the substantial enhancement of Raman scattering could not be understood either by the concentration increment of molecular species or by the increased surface area due to the electrochemically roughened process[18]. Jeanmaire and Van Duyne pioneerly proposed that the enhancement is due to the enhanced localized electric fields in closely positioned Ag nanoparticles, the so-call hot spots[18a], while Albrecht and Creighton suggested that the enhancement is due to charge transfer between plasmonic nanoparticles and analyte chemicals[18b]. Both theories are proved and widely accepted today and this phenomenon is now known as surface enhanced Raman scattering (SERS)[19].

The investigation of SERS in the early years has been largely focused on phenomena occurring on electrochemically roughened Ag substrates. However, electrochemically roughened Ag substrates cannot provide significant SERS enhancement for single-molecule detection. Until the recent decades, the design and synthesis of SERS substrates have been remarkably improved, largely due to the vigorous advances in micro- and nanofabrication. An enhancement factor (EF) of ~10^{10} and above has been reported, which can readily detect single molecules of various species[20]. Also owing to the advantage in determining molecules in a label-free and multiplex manner, SERS was applied in detection of various bio-relevant species, such as DNA/gene [21], anthrax [22], chemical warfare–stimulant [23], and glucose level in patients [24]. It has also been explored for environmental protection [25], study of chemical catalysis, [26] and trace of explosive-agents for safety and defense purpose [27]. However, until now, the great potential of SERS biochemical detection has not been fully materialized due to four challenges: (1) it is extremely difficult to make surface-plasmonic-resonant (SPR) nanostructures that can provide a large number of uniform and well-reproducible hotspots for repeatable SERS enhancement; (2) it is even more arduous to robustly obtain ultrahigh sensitivity from the plasmonic structures to detect a broad spectrum of species; (3) most of the state-of-the-art SERS sensing requires the searching effort for hot-spots, which is time-consuming and irrational; (4) it remains a grand challenge to directly test the Raman signal from the suspension with high sensitivity.

1.2.1. SERS Enhancement Mechanisms

As discussed before, the effect of SERS can be generally attributed to two mechanisms: the electromagnetic enhancement and chemical enhancement mechanisms.

1.2.1.1. Electromagnetic Enhancement

When an electromagnetic wave interacts with metal nanoparticles, the localized surface plasmon occurs, where the conduction-band electrons in a metal nanoparticle collectively oscillate. (Figure 1.2a) As a result, substantially enhanced *E*-fields can be found in the vicinity and junctions of the nanoparticles (Figure 1.2b). The locations that have the enhanced *E*-field are also called hotspots. For molecules in the hotspots, their Raman scattering signals can be dramatically boosted. The enhancement factor of a single molecule (*SMEF*) due to such an effect can be simply expressed as[28]:

$$SMEF \approx M_{Loc}(\omega_L) M_{Rad}(\omega_R) \approx \frac{|E_{Loc}(\omega_L)|^2}{|E_{Inc}|^2} \frac{|E_{Loc}(\omega_R)|^2}{|E_{Inc}|^2} \qquad 1.2$$

where M_{Loc} is enhancement of the local field intensity, M_{Rad} is the radiation enhancement factor, ω_L and ω_R are the resonant angular velocities of the local (E_{loc}) and radiation field (E_{rad}), respectively. E_{inc} is the incidental *E*-field. In many cases, the Raman shift is small and thus an approximation of $\omega_L \approx \omega_R$ can be made. This lead to the widely known expression of the SERS enhancement factor as $SMEF \approx |E_{Loc}(\omega_L)|^4 / |E_{Inc}|^4$.

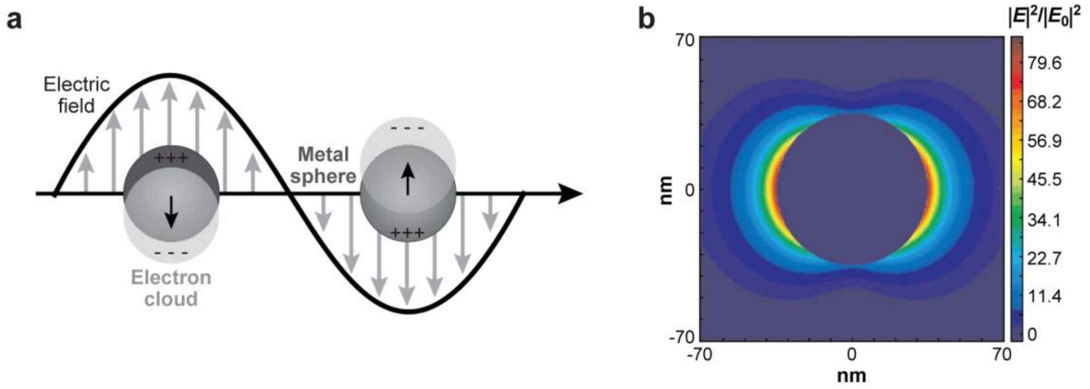

Figure 1.2. (a) Illustration of localized surface plasmon resonance; (b) Extinction coefficient (ratio of cross-section to effective area) of a spherical silver nanoparticle of 35 nm in radius in vacuum. $|\boldsymbol{E}|^2$ contours for a wavelength corresponding to the plasmon extinction maximum. Peak $|\boldsymbol{E}|^2/|\boldsymbol{E}_0|^2 = 85$.[29]

Therefore, it can be readily known that enhancement of the localized *E*-field is the most effective method to increase the SERS sensitivity. For instance, if the plasmonic resonant enhances the localized *E*-field by 10 times, the Raman signals of molecules can be increased by 10,000 times. Indeed, by optimizing the size, materials, and junction features of plasmonic nanoentities, a SERS enhancement factor (EF) of 10^{10} and above can be achieved [30]. The electromagnetic enhancement is the dominating mechanism for the as-observed ultrahigh EF.

According to Equation 1.2, it can be readily seen that both the incident and the Stokes scattered fields should be enhanced to achieve the maximum enhancement factor. It is of great interest to systematically study the optimum excitation wavelength relative to the spectral position of the localized surface plasmon resonance (LSPR) extinction. With the wavelength-scanned surface-enhanced Raman excitation spectroscopy (WS SERES), McFarland et al.[31], experimentally proved that the highest SERS EF can be obtained when the wavelength of the excitation source has a higher energy than that of the spectral maximum of the LSPR extinction and is blue shifted to it. For each individual vibrational mode, the maximum enhancement can be obtained when the energy of the excitation laser is in the middle of the Raman shift and the LSPR spectral maximum, where both the incident and Raman scattered photons can be strongly enhanced. Therefore, not all the vibrational modes of molecules can be uniformly enhanced in one SERS test[31-32]. These understandings are important for rational design and optimization of SERS substrates.

1.2.1.2. Chemical Enhancement

The electromagnetic enhancement mechanism cannot fully explain the magnitude of SERS enhancement. Evidences showed that there should be a second enhancement mechanism which works independently of the electromagnetic enhancement. For instance, the SERS intensities of CO and N_2 molecules differ by a factor of 200 at the same experimental conditions[33], while electromagnetic enhancement should not depend on molecular species.

These observations can be explained by a resonance Raman mechanism (chemical enhancement) in which the new electronic states arising from chemisorption serve as resonant intermediate states in Raman scattering. The highest occupied molecular orbital (HOMO) and lowest unoccupied molecular orbital (LUMO) of the adsorbate can be symmetrically positioned in the energy band diagram with respect to the Fermi level of the metal (Figure 1.3). In this case charge-transfer excitation (either from the metal to the molecule or vice versa) can occur at around half of the energy of the intrinsic excitation energy of the adsorbate, which greatly increase the number of excited electrons and thus Raman signal. Research showed that the magnitude of the chemical enhancement is usually 10–100[33].

Researchers worked on the development of a comprehensive theory to describe the SERS enhancement mechanisms and factors for a long time. Recently, Lombardi et al.[34] derived a single expression for SERS enhancement based on Herzberg-Teller coupling, which includes contributions from: (1) the surface plasmon resonance in the metal nanoparticle; (2) a charge-transfer resonance involving transfer of electrons between molecules and the conduction band of the metal; and (3) resonances within the molecules themselves. In the study, they demonstrated that the three types of resonances were tightly bonded by Herzberg-Teller vibronic coupling terms and could not be treated individually. However, they did not consider the non-resonance changes in the molecular polarizability that occurs upon adsorbing to the metal surface. Valley and his co-workers[35] studied both normal and surface-enhanced Raman spectra for a set of substituted benzenethiols. They found that the enhancement obtained by experiments varies by a factor of 10 as a result of chemical substitution. Stronger electron donating groups on the benzene unit lead to higher enhancement. The experimental results agree well with the calculation from the static polarizability derivatives determined by the time-dependent density functional theory (TDDFT).

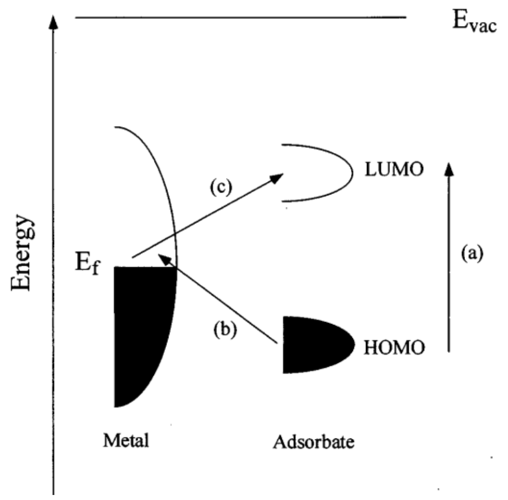

Figure 1.3. Typical diagram of energy band of a molecule adsorbed on a metal surface. The occupied and unoccupied molecular orbitals are broadened into resonances by their interactions with the metal states; orbital occupancy is determined by the Fermi energy. (a-c) A possible charge transfer excitation is shown[33].

1.2.2. Review of the State-of-the-Art Substrates for Biodetection with Raman Spectroscopy

Based on the understanding of the fundamental mechanisms of SERS, intensive interest is focused on fabricating SERS nanostructures with optimal materials, sizes, and configurations for significant enhancement of Raman signals of molecules (Figure 1.4).

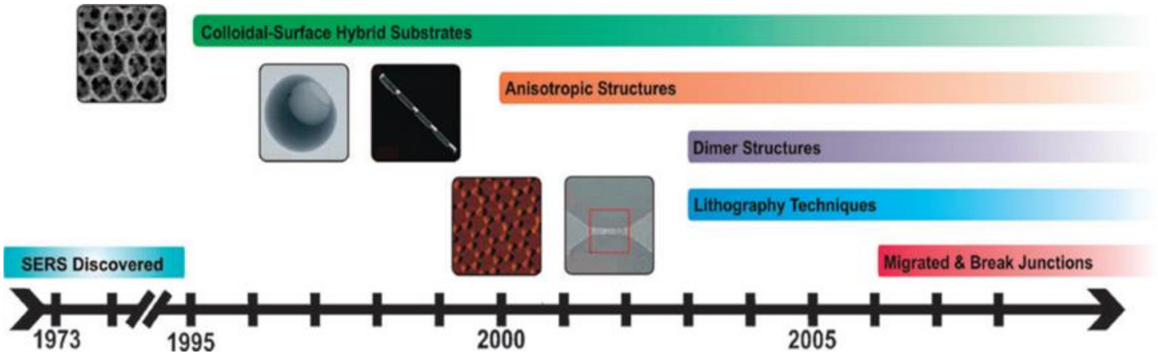

Figure 1.4. Progress on development of suitable SERS substrates[36].

In general, four typical types of SERS nanostructures emerged with large electromagnetic enhancement: (1) roughened surfaces, e.g., rough Ag surfaces; (2) nanoparticles with controlled aggregations that form nanogaps, e.g. dimers and trimers; (3) nanostructures with sharp tips; and (4) designed core-shell nanostructures[37]. As a few thousand papers have been published on the fabrication of SERS substrates in the last decade, we will not discuss all approaches used for fabricating SERS substrates but focus on the recent advances according to the most commonly employed synthesis techniques, including wet chemical synthesis, lithography patterning, and bio-assisted fabrication, with elaboration on representative work.

1.2.2.1. Wet Chemical Synthesis

Wet chemical synthesis methods such as hydrothermal fabrication have been broadly adopted for large-scale efficient growth of monodispersed plasmonic nanoparticles[38]. The sizes and shapes of the plasmonic nanocrystals can be precisely controlled by the temperature, concentration and stoichiometry of reagents, as well as surfactants or additives. However, most of the as-synthesized nanoparticles are dispersed as suspensions without controlled aggregations, while nanoparticle pairs with narrow junctions are of dire needs due to the ultra-strong localized surface plasmon resonance (LSPR). In the early days, salt solution was added during the drying process of nanoparticles, which can result in compact aggregation of the plasmonic nanoparticles and narrow junctions between the nanoparticles. Although, SERS EF as high as 10^{12} to 10^{14} has been reported [20], the control of the junctions of nanoparticles (hotspots) are adversely random in EF enhancement, quantity, and location[39]. Interestingly, to obtain dimer/trimer/small aggregate structures, transparent silica or polymers were designed to enclose or link two or more plamonic nanoparticles in individual capsules[40]. Moreover, assisted with the nanoporous templates, nanopeapods were synthesized and used for intracellular pH sensing[41], which represents a great advance in creating controllable hotspot junctions with colloidal nanoparticles, although the number of nanoparticles in each peapod is random.

In another approach, Au (or Ag) nanoshells received consideration attention. Typically, Au (or Ag) nanoshells were synthesized via deposition of Au seeds (1-2 nm) on monodisperse silica spheres followed by the growth of Au nanoshells to fully cover the entire surface of the silica spheres. Based on this structure, Au/Ag hollow shell assemblies were fabricated and applied as the near infrared SERS probes which can readily detect Raman signals of molecules in 8 mm deep animal tissues[42]. However, nanoparticles in suspension can degrade over time and thus jeopardize their SERS enhancement. It is essential to create plasmonic nanoentities that can be stored in suspension for a long time. Shell-isolated nanoparticles, e.g., Au particles coated with ultrathin silica or alumina shells, that are well protected from molecule contamination and reaction with the solution were synthesized, and thus offer long shelf lifetime[43]. Related to such structures, a large number of core/shell based nanoentities were synthesized, including multilayer Au nanoshells, the so-called nanomatryoshka (Figure 1.5a)[44]. By tuning the dimensions of cores and shells, the plasmonic resonant frequency of the nanoparticles can be monotonically controlled from the visible to the infrared regime[45]. Particularly, bimetallic and bi-functional core/shell structures received considerable interest. In such structures, one of the metallic components is SERS active and can be readily applied to monitor the catalytic reactions on the other material component. The bimetallic core/shell structures are fabricated into different shapes, including nanoraspberries[46] and starfish[47]. Finally, besides the chemical synthesis as mentioned above, template-assisted[48] and polymer mediated wet-chemical growth[49] were also employed for the fabrication of SERS nanoparticles.

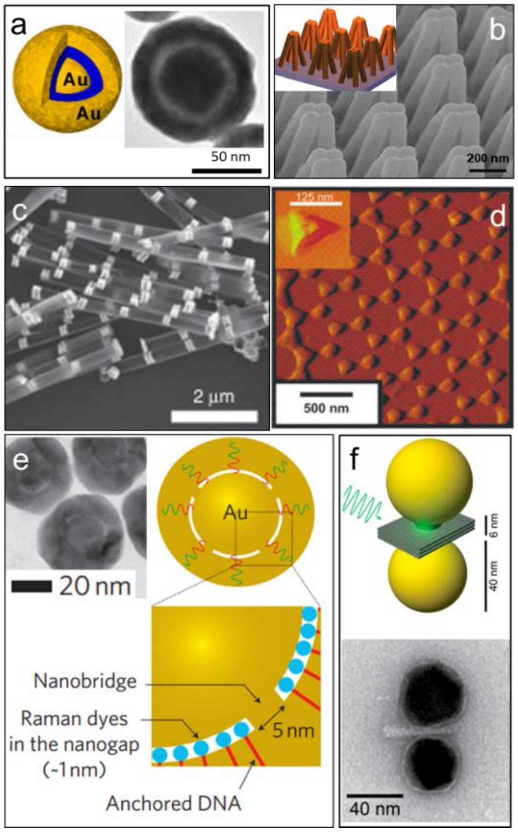

Figure 1.5. (a) Schematic and SEM image of a gold Nanomatryoshka particle[44]; (b) Schematic and SEM images of gold nanofingers arrays[50]; (c) On wire lithography: pairs of gold nanodisk with nanogaps[51]; (d) Nanosphere lithography: tapping-mode AFM image of a representative nanoparticle array. Inset: a close up image of one triangle[52]; (e) Schematic and SEM images of the gold shell particles template on DNA molecules[53]; (f) Schematic and SEM images of DNA-origami nanoantennas built from two gold nanoparticles linked via a three-layered DNA origami block at a separation distance of 6 nm[54].

1.2.2.2. Top down Lithography Methods

Lithographical techniques, such as photolithography, are broadly used in semiconductor industry. Among all the lithography techniques, the-state-of-the-art electron beam lithography (EBL) can make ultrafine plasmonic nanostructures in an ordered array[55]. However, the high cost of EBL limits the practical applications of the devices. In addition to EBL, Gartia et al., demonstrated that freestanding nanopillars coated with silver can be fabricated by laser interference lithography on a six inch wafer and applied such structures for effective SERS detection. The SERS substrate offers an ultrahigh-uniformity and an average homogeneous enhancement factor close to 10^8.[56] With such kind of SERS substrates, even volatile compounds, such as toluene vapor, can be detected. A simple adsorption model was also developed from the temporal evolution of SERS signals.[57] In parallel, the nanoimprint lithography, developed by Chou et al. [58], emerged as an economic alternative technique of EBL for mass production of nanostructures with high precision. A notable work is reported by Hu et al., who successfully created ordered arrays of gold-capped-polymer nanofingers in a large scale by nanoimprint lithography [50, 59], where designed numbers of nanofingers can be snapped together on the finger tips and form narrow junctions due to the surface tension generated in the process of solvent evaporation (Figure 1.5b). The EF in the junctions is estimated as $\sim 10^{10}$, one of the highest among the state-of-the-art.[50, 59] Similar to the concept of snapped fingers, Schmidt et al., explored another route to economically create hotspots on a wafer scale in assembled silver-capped Si nanopillars via maskless reactive ion etching [60]. By assuming that only a few molecules are trapped in the hot spots, which account for the detected Raman signals, an EF of $\sim 10^{11}$ is estimated. Recently, silver nanoparticle islands over a silver mirror with a SiO_2 spacer layer was fabricated by the standard sputtering and evaporation techniques. Such SERS substrates can detect an unprecedented number of single molecule events (>7000) [61].

1.2.2.3. Reductive Fabrication Based on Selective Etching

In addition to the aforementioned approaches, unique etching methods, such as on-wire lithography[51, 62] were developed to make SERS substrates with junctions of a few nanometers for ultrahigh and well reproducible enhancement (Figure 1.5c). The on-wire lithography technique relies on fabricating designed multi-segment nanowires with segments made of distinct chemistry before removing selected segments to create gap structures. Note that the nanowires are conformably coated with a silica film to fix the relative positions of the metal segments and thus the gap sizes before the selective etching. As a result, arrays of a few nanometer junctions can be rationally created between the unetched nanodisk/rod pairs (Figure 1.5c), which demonstrate single-molecule sensitivity in detecting various biochemicals such as methylene blue[62c], p-mercaptoaniline[63], and Cy-3-labeled DNA[64]. However, the number of hotspots that can be created on each nanowire is limited to a few. Also the positions of the nanowire gaps are largely random on a substrate. Therefore it takes great efforts to find hotspots before detecting molecules. The earlier work including nanosphere lithography[52], (Figure 1.5d) porous template-assisted deposition[65], and nanosphere templated nanocrescent fabrication[66] were also explored to create controlled hotspots in a large array for sensitive SERS detection.

1.2.2.4. Bio-Assisted Fabrication

Recently, the state-of-the-art DNA-origami[53-54, 67] assisted assembling of plasmonic nanoparticles emerges for fabrication of plasmonic nanoparticle pairs with precise geometry, gap size and number of particles. For instance, Lim et al.[53] successfully prepared DNA-tailored nanoparticles with 1 nm junctions for highly uniform and reproducible SERS as shown in Figure 1.5e; Kühler et al.[54] innovatively coupled plasmonics with DNA-origami and obtained nanoantennas from two gold nanoparticles linked by a three-layered DNA origami block with a separation distance of 6 nm (Figure 1.5f).

1.2.3. Problems in the SERS Sensors

Despite all the aforementioned progress in the fabrication of SERS substrates, the practical applications of SERS for biochemical detection remain a grand challenge because: (1) it is difficult to create a large number of uniform hotspots for well-repeatable SERS detection at a low cost. We note that a major effort in all of the previously discussed fabrication explorations is to obtain reproducible SERS substrate with controlled sizes of hotspots. This task is extremely challenging. According to Equation 1.2, the enhancement of Raman signals increases with E^4 and the strongest SERS are largely obtained from nanojunctions of a few nanometers in sizes. As a result, variation of the junctions of a few nanometers can result in SERS fluctuation as high as an order of magnitude. This presents a grand challenge to obtain reproducible and uniform SERS substrate with current fabrication techniques; (2) it remains arduous to obtain ultra-sensitivity from the hotspots for detection of a broad spectrum of species due to the difficulties in controlling the sizes of hotspots to as small as a few nanometers; (3) It is even more challenging to realize location predicable sensing for rapid detection without the time-consuming searching effort; (4) it remains a grand challenge to directly test the Raman signal from the suspension with high sensitivity. In chapter 2 and 3, I will discuss my work on addressing these issues in SERS detection.

1.3 ELECTROKINETICS FOR NANOPARTICLE MANIPULATION AND ASSEMBLING

Electrokinetics refer to the migration of electrically charged or uncharged particles with sizes on the scale of micrometers or nanometers in liquid by an applied electric field provided via immersed microelectrodes in suspension, The related phenomena[68] include so-called electroosmosis[69], electrophoresis[70], and dielectrophoresis[71] as shown in Fig 1.6. Here, I will focus on the discussion of electroosmosis and dielectrophoresis, which are employed in the manipulation and assembling of various aforementioned synthesized nanoparticles in the dissertation works.

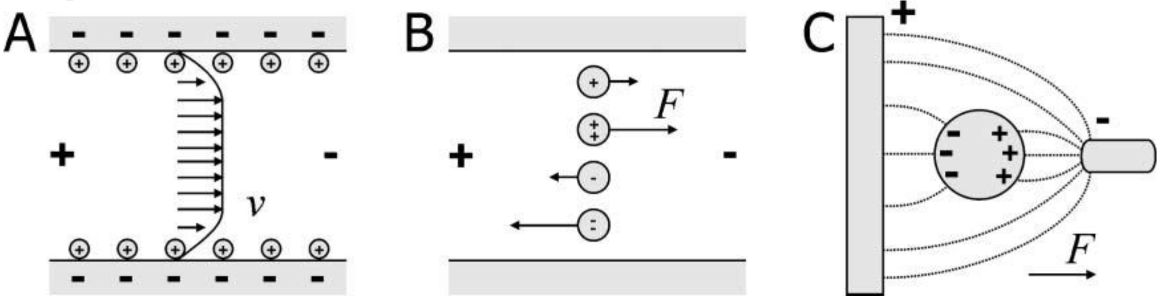

Figure 1.6 Basic electrokinetic effects. (a) Electroosmosis or Electroosmotic flow (EOF), (b) electrophoresis (EP), (c) dielectrophoresis (DEP)[72].

1.3.1 Dielectrophoresis

Although DEP was first understood and named by H. A. Pohl back to 1950s[73], it has intrigued intensive interest recently due to its highly desired implications on sorting, separating, and concentrating nanoparticles, microparticles and various biomaterials. For a neutral or charged particle which exposed to a non-uniform electric field, depending on frequency of applied electric field, the DEP forces can be categorized to AC DEP[74], DC isolator-based DEP[75], Combined AC/DC DEP[76], and traveling wave DEP (tw-DEP)[77].

The mechanism of DEP can be understood by the distinct polarizability between nano/microparticles of interest and the suspended medium. In an electric field, a neutral particle polarizes and accumulates positive and negative charges on the opposite side of the particle. In a uniform electric field, these accumulated charges experience Columbic forces of the same magnitude in opposite directions, which cancel each other as shown in Fig. 1.7a. As there is no net force, the particle remains stationary. However, in a non-uniform electric field, these Columbic forces which exert on the accumulated charges have distinct magnitude and hence result in a net force as shown in Fig. 1.7b and c. This net force drives the particle toward higher or lower electric field gradient. The transport direction of a particle depends on the polarization of the particle and the surrounding medium. If the particle is more polarizable than the surrounding medium, the particle will move towards to the high electric field gradient region, which is called the positive DEP effect (pDEP) as shown in Fig 1.7b; on the other hand, if the surrounding medium is more polarized than the particle, the particle will be repelled towards the low electric field gradient region, which is called the negative DEP effect (nDEP) as shown in Fig 1.7c.

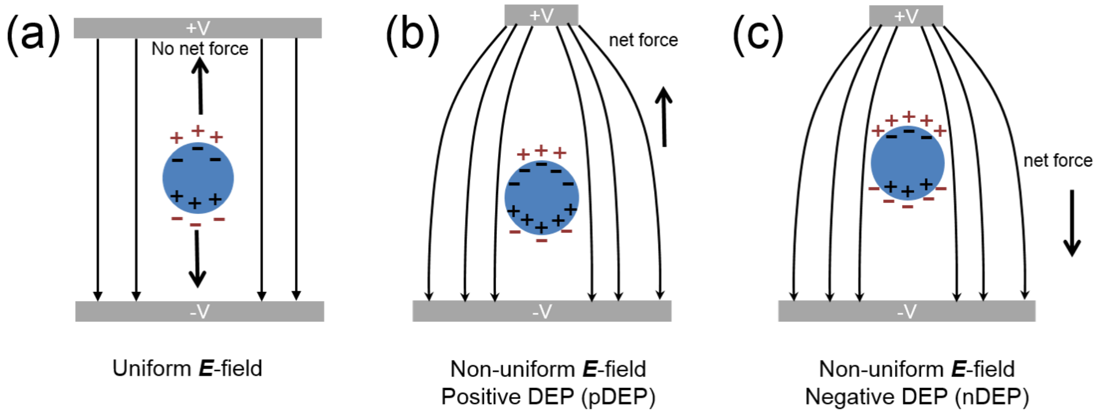

Figure 1.7 Schematic diagrams illustrate particle polarization in (a) a uniform electric field. In a non-uniform electric field, (b) when the particle is more polarizable than that of the medium and it experiences a net force towards the high electric field gradient region, it is known as pDEP. (c) when particle is less polarizable than that of the medium, and the net force on the particle acts towards the low electric field gradient region, it is known as nDEP.

The DEP force can be expressed as[78]:

$$F = p \cdot \nabla E \qquad 1.3$$

where p is the effective dipole moment, ∇E is the electric field gradient. For a spherical particle, the DEP force can be given as:

$$F = p \cdot \nabla E = 2\pi\varepsilon_m R^3 Re(K) \nabla E^2 \qquad 1.4$$

where $p = 4\pi\varepsilon_m R^3 Re(K)E$ is the effective dipole moment, ε_m is the dielectric constant of the suspension medium, R is the radius of the spherical particle, and $Re(K)$ is the real part of the Clausius-Mossotti factor of the particle which determines whether DEP force is positive or negative. If $Re(K) > 0$, the particle is attracted towards to the highest E-field gradient; if $Re(K) < 0$, the particle is repelled towards to the lowest E-field gradient.

Since the real part of the Clausius-Mossotti factor is determined by the intrinsic properties of the particle and the suspension medium, such as conductivity and dielectric constant - various particles have different dielectric constants and conductivities - We should expect that the DEP force experienced by different particles or cells at the same AC *E*-field is totally different which can be utilized to sort or separate particles or cells. Meanwhile, at different *E*-field frequencies, the Clausius-Mossotti factor can be either positive or negative. Therefore, we can either collect and concentration the interested entities or toss them as they subject to the repel force.

Currently, DEP is widely applied in the characterization of the bioparticles and colloidal particles. For example, DEP can be used to determine the cell viability change or cell death[79]. It was found that the plasma membrane of a viable cell has a very high electric resistivity which is typically greater than 1 MΩ m. Thus at a low frequency, the viable cell appears as insulator[80]. However, when the cell goes through the apoptosis or necrosis, it becomes more conductive. By monitoring the related change of the DEP behavior of the cells, one can readily know whether the cell is dead or not. In addition, this method is label-free which is favorable in cell analysis. Suehiro et al group successfully separated the viable and non-viable *Escherichia coli* cells using the DEP effect on an interdigitated microelectrode[81]. Fintschenko has demonstrated that not only dead and live *Escherichia coli* were distinguishable using the iDEP method, they can also differentiate the 1 and 0.2 µm colloid spheres from the bacterial cells[79a]. Other bioparticles are also separated based on the DEP effect. For example, various viruses can be effectively separated by the DEP force. Morgan et al group has demonstrated that two types of viruses - the plant virus which is tabacco mosaic virus (TMV), and the mammalian virus which is herpes simplex virus (HSV) type 1 - were separated based on their different responses to *E*-field on the same polynomial electrode. The TMV experienced positive DEP and were collected at the high field regions at the edge of the electrodes, while the HSV received the negative DEP and were repelled towards to the low field region in the center of the electrode[82]. The same group later reported that the DEP effect even can be utilized effectively to separate two nonenveloped plant viruses of different geometry. This time they chose TMV which is a rod-shaped virus and Cow Pea Mosaic Virus (CPMV) which is a spherical-shaped virus. Although these viruses possess the similar dielectric and conductive properties, due to different geometry shapes, their crossover frequencies are totally different which makes it possible to separate them under the same *E*-field[83]. Furthermore, the DEP effect was also explored to differentiate other bioparticles, such as: DNA[84] and protein[85].

Dielectrophoresis is also used to sort colloidal particles. Green demonstrated continuously sorting of latex particles with sizes of 2 µm, 1 µm and 500 nm in a V-shaped or Chevron-shaped microelectrode arrays. The colloidal particles with various sizes were deflected by the nDEP effect into different outlet channel[86]. Lam et al group innovatively integrated the conductive sidewall electrode to the Y-shaped channel, which enhanced the DEP force in three dimensions. With such design, they are able to continuously sort and separate 5, 10 and 15 µm particles.[87]. In addition to sorting and separating the colloidal particles, the DEP effect is used to manipulate colloidal particles, and form various assembled structures such as particle chains, quasi-2D colloidal crystals and 3D colloidal crystals[88].

1.3.2 Electroosmosis

Electroosmosis usually refers to the movement of liquid relative to a stationary charged surface due to an applied electric field in the low frequency regime of < 100 kHz. The discovery of this phenomenon is credited to Reuss[89] who, in 1809, reported water migration through porous clay under applied electric field. Later, Hermann von Helmholtz[90] quantitatively explained this phenomenon based on an electric double layer (EDL) model. The EDL concept was further expanded by Louis Georges Gouy[91] and David Leonard Chapman[92] who introduced the diffusive charge layer concept into the original model and their model was named as Gouy-Chapman (GC) model. Otto Stern[93] further developed this model and suggested the combination of the Helmholtz model with the Gouy-Chapman model, which is now known as the Gouy-Chapman-Stern (GCS) model (Fig. 1.8). Since then, the EDL model has been used as the fundamental theory to interpret the electrokinetics.

In the classical electroosmosis model, solid surfaces acquire a finite density of electrical charges when they are in contact with an aqueous solution. In order to maintain electroneutrality, the charged surface attracts counterions from solution and repel coions, resulting in the formation of an electrical double layer. When an external electric field is applied parallel to solid surface (E_0), cations are forced to migrate along the direction of the electric field. Due to the viscosity of fluidic, flow which is surrounding the ions is dragged by the ions and moves along with ions which results in the so-called electroosmosis flow (EOF). At the steady state, the velocity of the bulk fluidic reaches a constant value, which can be expressed as[94]:

$$u_s = -\frac{\varepsilon_f \zeta}{\mu} E_0 \qquad 1.5$$

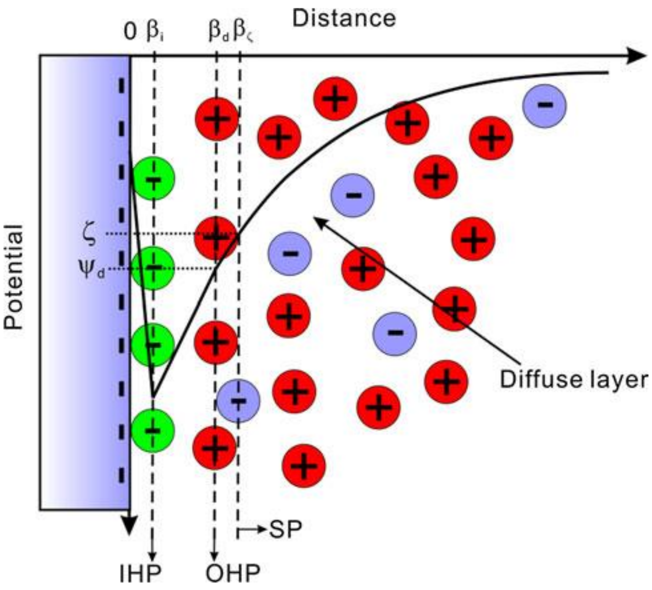

Figure 1.8 Schematic illustration of an electric double layer (EDL) of a negatively charged interface according to the Gouy-Chapman-Stern model[69a].

where ε_f and μ are the permittivity and viscosity of the fluid, respectively. ζ is the zeta-potential, and E_0 is the applied electric field. This equation indicates that the velocity of the fluid is linear proportional to the applied E-field. Unlike the pressure-driven flow, the EOF does not depend on the dimension of the channel; the EOF velocity profile outside the electric double layer is usually flat or plug-like. Normally, EOF is generated by a DC electric field. However, the application of the DC electric field has a great disadvantage.

As mentioned before, the velocity of fluid is proportional to the applied DC field. In order to achieve a high speed and more efficient fluid transportation in a relatively large scale, a high electric field need to be generated which may result in side effects such as joule heating and electrolysis. Meanwhile, only a few specific types of solution can be used under such conditions which dramatically limited the usage of the technique. In order to solve the above issue, the alternative current electroosmosis (ACEO) is developed.

In 1999, Ramos[69b] discovered the non-linear electroosmosis flow due to the exerted AC electric field on the fluid. As the AC electric field was applied on the coplanar electrodes which was deposited on a glass substrate, the static flow pattern which consisted of counter rotating vortices formed (Fig 1.9). The experimental, theoretical, and numerical analysis of this phenomenon were further developed later by Green and González in their papers[95].

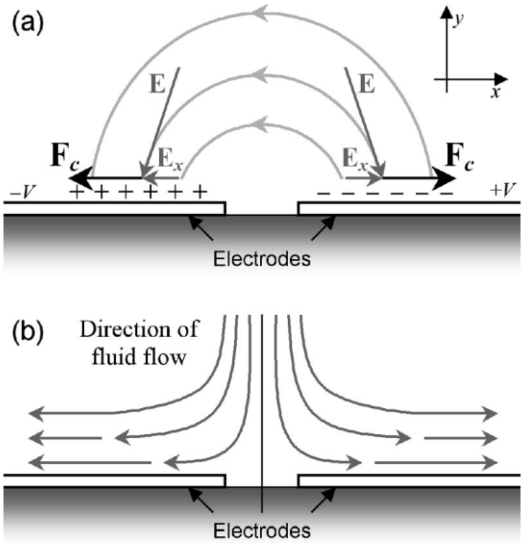

Figure 1.9 A schematic diagram of the mechanism of ACEO of electrode arrays used in experiments. The electrodes consist of two long plate electrodes separated by a narrow gap. (a) shows the induced charge layers and the electric field E at a time point, resulting from a potential difference applied to the two electrodes. The electric field has a tangential component E_x at the surface of the electrodes, producing a force F_c on the surface charges. The time averaged value of this force for an alternating potential is nonzero, producing a steady fluid flow pattern shown schematically in (b). The fluid flow is driven at the surface of the electrodes, moving across the surface and dragging fluid down to the center of the gap[**95c**]**.**

In principle, the ACEO flow is due to the interactions of the *E*-field and the electrical double layers next to the electrodes. The fluid velocity in the horizontal direction is given by[96]

$$v_{fluid} = \varepsilon_m V_{rms}^2 / [\eta(1+\delta)L\left(\frac{\omega}{\omega_c}+\frac{\omega_c}{\omega}\right)^2], \qquad 1.6$$

where V_{rms} is the root mean square of applied voltage; ε_m and η are the permittivity and viscosity of the suspension medium, respectively; L is the electrode spacing; δ is the capacitance ratio of the diffusion and compact layers (assumed as constant for both); ω_c

and ω are the peak and applied E-field frequency, respectively. Equation 1.6 indicates that the fluid velocity is not linearly proportional to the electric field, instead, is proportional to the V_{rms}^2 which dramatically increases the velocity at a low voltage condition, and makes it favorable in the microfluidic devices. In addition, here the AC electric field is applied to avoid the electrolysis problem which will occur at a few voltages under the DC electric field. However, the ACEO flow formed in this symmetric electrode setup only generates local flows which may be employed for mixing liquid, but cannot generate a net flow in microfluidic channel. Ajdari[97], in 2000, predicted theoretically that a net ACEO flow can be generated by breaking the symmetric of electric geometry. He also envisioned that ACEO can be used as a pump. Based on this idea, Brown[98] designed the asymmetric electrode arrays, and experimentally observed net flow of water across designed electrodes for the first time. Mpholo[99] further improved this design and achieved a net flow velocity as high as 450 μm/s at 2.2 V_{rms}. Recently, Wu[100] built an ACEO micropump based on the asymmetric electrode with a DC offset which dramatically increased the flow velocity since the flow velocity exponentially depends on the applied voltage. Ng[101] applied the DC assisted ACEO for mixing, which efficiently improved the mixing rate of the two laminar flows. In addition to micromixing and pump, Wu[102] demonstrated that ACEO can be used to trap and concentrate bacteria in the middle of the electrode gap, and can potentially improve the detection sensitivity.

In this dissertation, the ACEO effect is utilized to assist the attraction of nanoparticles as well as molecules which will be elaborated in Chapter 3.

Chapter 2: Synthesis of Optically Active Nanomaterials†

In the past five years, I have investigated the synthesis of various optically active materials, including semiconductor ZnO, Si nanowires, ZnO nanosuperstructures, Au nanowires, and composite nanocapsule structures. In this chapter, I will discuss the design, synthesis, and characterization of the above nanomaterials.

2.1 ZNO NANOSUPERSTRUCTURES

ZnO has been widely used for various kinds of applications in electronics and optoelectronics, not only for its wide bandgap (3.37 eV) and high exciton binding energy (60 eV), but also due to its diversified morphology. A wide range of ZnO nanomaterials have been synthesized including nanowires[103], nanorings[104], nanosheets[105], and nanosuperstructures (NSSs)[106]. Among them, NSSs are of particular interest due to their higher surface area compared to other structures. A commonly used method to synthesize NSSs is based on multi-step catalyst-seeding assisted deposition in a chemical-vapor or hydrothermal system.[107] The branches of ZnO NSSs can be grown on pre-fabricated nanowire trunks by deposition of metal nanoparticle catalysts or seed nanoparticles[108]. NSSs made of various materials such as ZnO and silicon have been synthesized in this manner.[108-109] However, this method requires a multi-step reaction and exposes samples to atmosphere during fabrication, which may result in contamination, impairing the

---

† Portions of this chapter have been previously published in C. Liu, X. Xu, Alex Rettie, C. Mullins and D. L. Fan, Journal of Materials Chemistry A, 1 , 8111- 8117 (2013); C. Liu, X. Xu, K. Kim, D.L. Fan, Advanced Functional Materials, 24, 4843–4850 (2014), C. Liu, X. B. Xu and D. L. Fan, ASME-Journal of Nanotechnology in Engineering and Medicine, 5, 040906, (2015)

performance of nanodevices. ZnO NSSs were also directly synthesized on nanowires without catalytic seeding, such as on ZnO[110], Si[109d] and Ga_2O_3[111]. None, however, achieve controlled growth on each segment of the trunk nanowires.

To investigate a general mechanism for 3-D NSSs synthesis, we rationally designed an approach for one-pot, one-step, and large-scale synthesis of ZnO 3-D NSSs by tuning the catalyst morphology and chemistry. By using this approach, 3-D nanosuperstructures were readily obtained from 1-D nanowire and large-area 2-D network catalysts. By tuning the chemistry of each segment of the nanowire catalysts, high morphological complexity with micrometer precision can be achieved. Waferscale 3-D NSSs can be fabricated in one step. The growth mechanisms of the ZnO NSSs and the roles of chemistry of catalysts were investigated, suggesting a general paradigm for one-step synthesis of highly-branched semiconductor nanosuperstructures.

Numerous studies have shown that suitable 0-D accommodation sites (nanodots) can catalyze nucleation and growth of 1-D semiconductor nanowires, such as ZnO, Si, and GaN in a chemical vapor deposition system.[103, 112] We hypothesized that 1 and 2-D catalysts, such as nanowires and nanonetworks, could promote the growth of 3-D semiconductor nanosuperstructures. We employed Au nanowires as catalysts (diameters of 55-300 nm fabricated by electrodeposition), dispersed these Au nanowires on a p-type Si (100) substrate, and then placed the silicon substrate into our CVD system. In a typical experiment, metal zinc powders 0.5 g (100 mesh, 99.9%, Alfa Aesar) were placed in the center of a tube furnace as the source material. A p-type Si (100) substrate carrying designed catalysts was loaded 12 cm from the source materials downstream of the carrier gas. The tube was purged with nitrogen gas (99.5%) and the pressure was lowered to 360 mTorr. The temperature of the furnace was gradually ramped to 550 °C in 30 min. Then gaseous oxygen (10 sccm, 99.5%) was introduced into the nitrogen stream (50 sccm, 99.5%) and maintained for 30 min. After the reaction, arrays of brush-like 3D NSSs with ZnO nanowire branches rooted on Au nanowire catalysts were synthesized as shown in Fig. 2.1b. The ZnO branches (lengths of 900 ± 100 nm and diameters of 60 ± 10 nm) were grown uniformly along the stems. EDX mapping confirmed that elemental Au is present in all the stems of ZnO NSSs, suggesting that it was Au nanowires that catalyzed the reaction. To further understand the role of Au for ZnO growth, we synthesized ZnO NSSs using a reaction time of only 1 min to observe the early stages of growth. As shown in Fig. 2.1d-e, short ZnO branches grew on the nanowire stems. However, the stems (Fig. 2.1e) had a larger diameter (125 nm) than that of the original Au nanowire (55 nm), which suggested that a layer of polycrystalline ZnO film grew around the Au nanowires before ZnO branch growth. High-resolution transmission electron microscope (HRTEM) characterization confirmed the existence of the ZnO film where the interface between the stems and branches can be identified as ZnO with the same lattice fringes of $(01\bar{1}\bar{2})$ and $(10\bar{1}1)$ in Fig. 2.2c-d. Fast fourier transformation (FFT) (in the inset) further verified the indexing. Using HRTEM on free-standing ZnO branches (prepared by sonication), we found the single crystalline branches grew along the [0001] direction similar to those catalyzed by larger diameter Au nanowires (diameter: 300 nm) (Fig 2.2a-b).[113] The lattice fringes of

$(01\bar{1}\,\bar{2})$ and $(10\bar{1}1)$ were observed because the branches were not perfectly flat on the TEM grid. The above HRTEM characterization indicates that ZnO branches grew epitaxially from a conformal ZnO polycrystalline film around the Au nanowires.

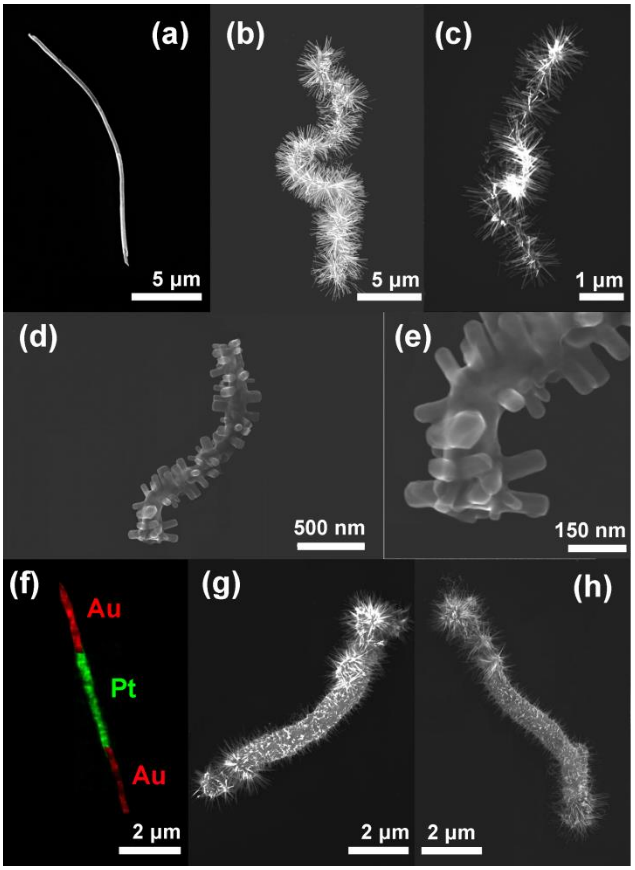

Figure 2.1. SEM images of (a) a 300 nm diameter Au nanowire, (b) ZnO NSSs grown on a 300 nm diameter Au nanowire, (c) ZnO NSSs grown on a 55 nm diameter Au nanowire, (d) SEM image of a single ZnO NSSs grown on Au 55 nm nanowire with short reaction time (1 min), (e) is the enlarged SEM image, (f) EDX mapping of a Au-Pt-Au nanowire, red represents Au, green represents Pt. (g) and (h) are SEM images of NSSs grown from the Au-Pt-Au nanowire.

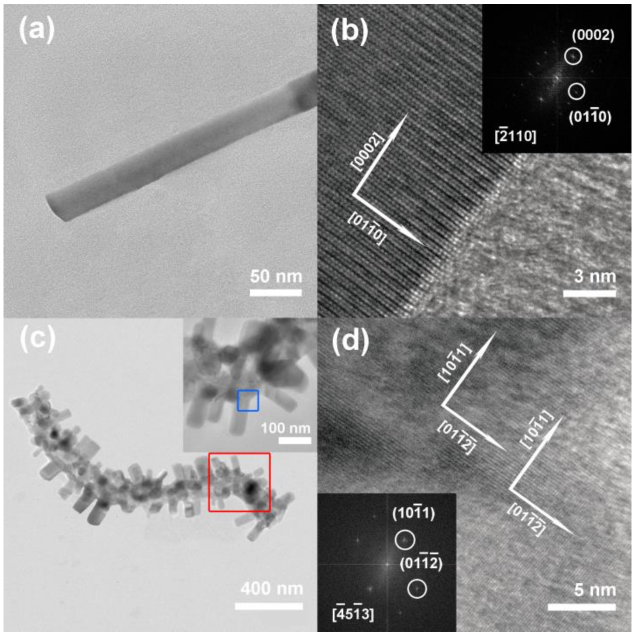

Figure 2.2 (a) a low magnification TEM image of individual ZnO nanobranch grown from Au 300 nm nanowire, (b) is the HRTEM image of (a), inset is the corresponding FFT image. (c) is the low magnification TEM image of a single ZnO NSSs at the initial stage. Inset is the enlarged image in the red rectangle area, (d) is the HRTEM of the blue rectangle region in (c) which corresponds to the interface between the stem and the ZnO nanowire, inset is the corresponding FFT image.

The TEM characterization suggests that the ZnO NSSs grow via a Vapor-Solid (VS) growth mechanism as opposed to the classical Vapor-Liquid-Solid (VLS) mechanism which has been widely used for synthesis of various semiconductor nanostructures including ZnO nanowires.[114] In the VLS mechanism, catalyst particles act as seeds for nanowire growth. The growth front is generally located between eutectic alloys, such as Au/Zn, and the growing material (ZnO). According to the phase diagram of Au-Zn, the lowest eutectic temperature of Au-Zn is 673 °C, much higher than the 550 °C used in our reaction. This implies that Au-Zn in our system remains in the solid state. Others also show that Au nanoparticles can stay in a solid state even at 950 ºC for catalysis of ZnO growth.[115] Also note that the dimensions of our Au nanowire catalysts are too large to show decrement of eutectic temperature due to size effects, as such an effect is only noticeable for particles less than 10 nm.[116] Furthermore, in VLS, the seed nanoparticles (Au for example) are typically located either at the tips or the roots of nanowires depending on the adhesion strength of the catalysts to the substrate. In practice, it is more common to find catalytic nanoparticles on the tips of nanowires.[113a, 117] As we see no evidence of Au in our ZnO branches, our results are not consistent with typical materials synthesized via the VLS mechanism. From the afore-analysis, we suggest that the growth of ZnO NSSs on nanowire catalysts is via VS mechanism.

But whether the VS mechanism can indeed be a viable route for ZnO NSS synthesis by 1-D catalysts? To verify the above analysis, we applied Pt nanowires as catalysts for ZnO NSS growth. It is known that the eutectic temperature of Pt-Zn (1645 °C) is significantly higher than that of Au-Zn (673 °C), which prohibit ZnO synthesis via the VLS mechanism. While, in our work, we readily obtained ZnO NSSs from Pt nanowires, which showed a branched structure, similar to those catalyzed by Au, but with shorter lengths. A previous study also demonstrated that ZnO nanowires can be catalyzed by Pt dots via the VS mechanism.[118] These results further support that the VS mechanism is the governing mechanism for synthesis of ZnO NSSs on Au nanowires. Also based on this understanding, we rationally designed a route to precisely control the complexity of ZnO 3D NSSs. By alternating catalytic materials along the length of the nanowires, e.g. using multi-segment

Au-Pt-Au nanowires as catalysts (as shown by EDX mapping in Fig. 2.1f), ZnO NSSs with distinct morphologies on different nanowire segments were fabricated (Fig. 2.1g-h, 2.3d). The branches on Au segments (~500 nm) are clearly longer and denser than those on Pt segments (<300 nm). As a result, tuning the chemistry of the 1-D catalysts via VS growth mechanism, we can further modulate the NSS morphology with microscale precision (Fig. 2.3d).

To understand how the materials chemistry of Au and Pt catalysts results in distinct morphology of ZnO, we studied the early growth of ZnO NSSs on Au-Pt-Au nanowires (reaction time: 1 min). It was found that the shapes of the Au segment backbones were clearly altered, while those from the Pt segments remained relatively rigid (Fig. 2.1 g and h). This effect can be attributed to the considerably higher diffusion rate of Au than that of Pt at an elevated temperature, as the surface diffusion coefficients of Au can be several orders of magnitude greater than that of Pt[119]. Therefore, Au can keep diffusing and exposing new nucleation sites during reaction, which encourages higher nucleation density and earlier emerging of ZnO nanowire branches compared to those catalyzed by Pt. As a result, denser and longer ZnO nanowire branches were obtained on Au segments than those on Pt segments. This understanding is consistent with previous work that surface diffusion plays a significant role in the VS mechanism.[115, 120]

In summary, we suggest that the growth of 3D ZnO NSSs is via VS mechanism in three steps: (1) Metallic (Au, Pt) nanowires act as the accommodation sites for Zn-vapor absorption [Fig. 2.3(a)]; (2) with the presence of oxygen, ZnO nucleates on the surface of nanowires, growing into a polycrystalline film on the entire surface of the nanowires [Fig. .2.3b]; (3) with abundant supply of Zn vapor and oxygen, the growth of ZnO nanowires occurs out of ZnO seeds along the [0001] direction,[114] which is a high-speed growth direction that is often found in ZnO nanostructures. (4) The chemistry of the nanowire catalysts play an important role in tuning the morphology of the catalysts, i.e. Au nanowires with higher surface diffusion coefficient than that of Pt assist growth of denser and longer ZnO NSSs structures.

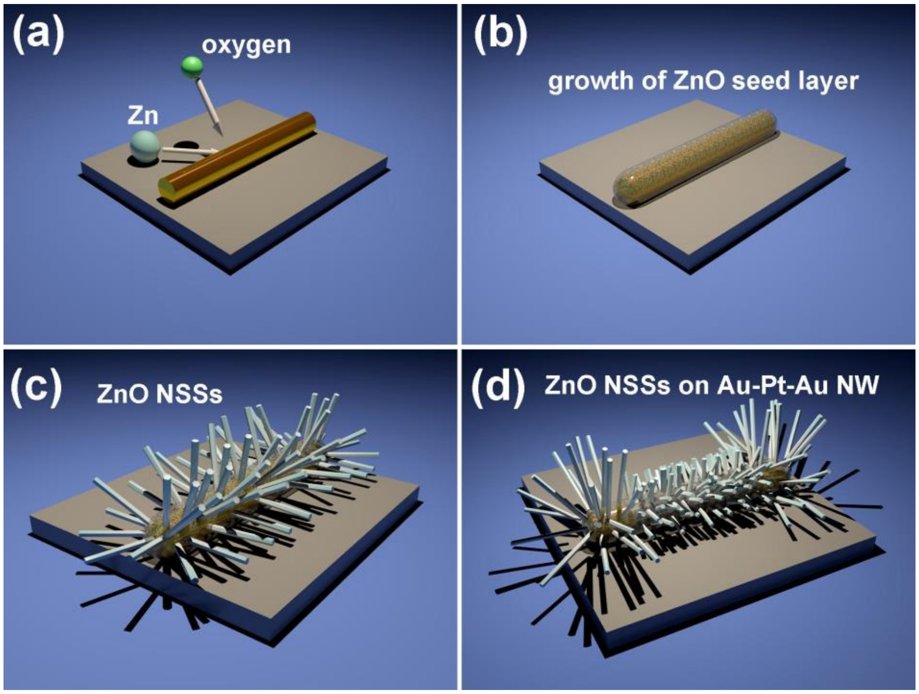

Figure 2.3. Schematic illustration of 3-D ZnO NSSs growth process. (a) Au nanowires act as the accommodation sites for Zn-vapor absorption; (b) with the presence of oxygen, ZnO nucleates on the surface of nanowires, growing into a polycrystalline film on the entire surface of nanowires; (c) with abundant supply of Zn vapor and oxygen, the growth of ZnO nanowires occurs out of ZnO seeds along the [0001] direction and form into 3-D NSSs on the nanowire catalysts. (d) 3-D ZnO NSSs morphology can be modulated with microscale precision by controlling the chemistry of the 1-D catalysts (Au-Pt-Au) via VS growth mechanism.

Large-area semiconductor NSSs are highly desirable owing to their high surface-to-volume-ratio and unique electronic properties. By properly tuning the morphology and chemistry of catalysts, we can readily obtain controlled NSSs on individual nanowire catalysts. However, it is very costly to make a large area of nanowire catalysts for wafer-scale applications. We noticed that porous Au films, which can be considered as a large-area nanowire network, can be fabricated by selective dealloying $Au_{49}Ag_{51}$ films in nitric acid (70%) as reported previously[121]. The as-fabricated porous Au was uniform with ligament diameters of approximately 50 nm. At the reaction condition of 550 °C and 30 min, the ligaments were further increased to 200 nm (Fig 2.4a). Applying porous Au thin films as catalysts we successfully obtained dense ZnO NSS arrays over the entire wafer surface in one-step fabrication as shown in Fig. 2.4b-c. This approach is highly facile compared to previous work[107, 109b] and originally designed based on our understanding of 3-D ZnO NSSs growth assisted by 1-D nanowire catalysis via the VS mechanism.

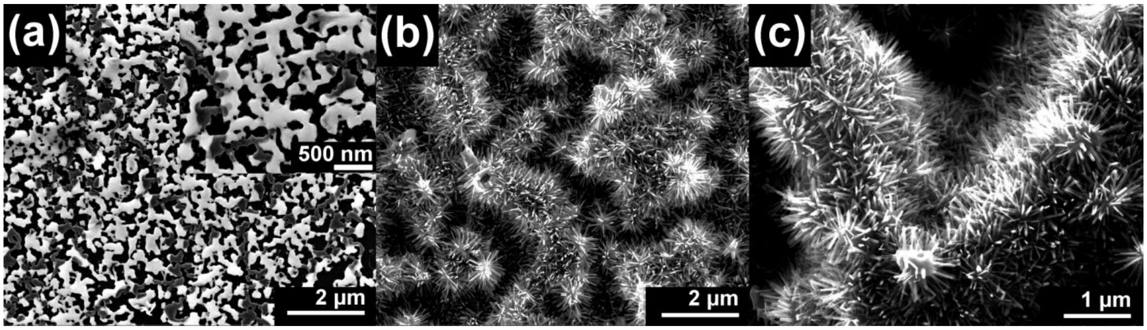

Figure 2.4. SEM images of (a) porous Au film annealed at 550 °C for 30 min, the inset is the enlarged image; (b) and (c) show ZnO NSSs grown on porous Au film.

2.2 SI NANOWIRE ARRAYS

Silicon nanostructures are under extensive study due to their potential applications in optoelectronics, renewable energy, and biosensors[122]. In particular, significant efforts have been made to synthesize silicon nanowires (Si NWs) due to their brilliant photonic, electrical, mechanical, and thermal properties and good compatibility with integrated circuits[109d, 123]. To date, Si NWs have been prepared by various methods. Among those methods, metal-assisted chemical etching is considered as an ideal one for highly ordered Si NW arrays because it is simple, effective, and cheap. However, it is still difficult to fabricate the Si nanowire arrays with a controllable size. Here, we innovatively applied colloidal lithography method, and successfully demonstrated the fabrication of Si nanowire arrays with precise size control. This method sheds light on a new fabrication routine.

The silicon nanowires were fabricated by Ag assisted chemical etching[124]. Different from previous work, Ag catalysts were strategically patterned on the entire Si wafer with monodispersed nanoholes by using colloidal lithography[125]. Si underneath the Ag film can be readily etched while the areas not in contact with Ag remain intact. As a result, large arrays of silicon nanowires with controlled diameters and lengths can be readily formed on the wafer. The distribution of the diameters of the silicon nanowires (200 nm ± 10 nm) is much narrower compared to previous reports[122d, 126], owing to monodispersity of polystyrene (PS) nanospheres [±5.5%, mean diameter 200 nm, Scheme 2.1, Figure 2.5c and its inset]. The detailed fabrication procedure consists of four steps as illustrated in Scheme 2.1 and Figure 2.5: first, a monolayer of PS nanospheres (Alfa Aesar, diameter

200 nm) was electrostatically coated on a Si (100) substrate without further treatment (Figure 2.5a). Then a thin silver film (~50 nm) was deposited via electron-beam evaporation at a base pressure of 5×10^{-6} Torr. Next, the PS nanospheres were sonicated in the toluene solution, exposing an array of nanoholes with controlled diameters on the Ag films (Figure 2.5b). Finally, the Ag patterned Si wafer was immersed in a mixture solution of HF (4.65 M, Acros organics) and H_2O_2 (0.25 M, J.T. Baker) for 30 min (Figure 2.5c). The etchant selectively removes Si underneath Ag and forms arrays of Si nanowires. The catalytic mechanism was attributed to Ag-assisted chemical reaction[124]. The Ag-assisted chemical reaction involves three steps (Scheme 2.2): 1. the reduction of hydrogen peroxide occurs preferentially on the surface of the Ag layer and generates holes, which is the cathode reaction and can be described as:

$$\frac{n}{2}H_2O_2 + nH^+ \longrightarrow nH_2O + nh^+ \qquad 2.1$$

2. the generated holes diffuse through the Ag layer and inject to the Si substrate which is underneath the Ag layer. 3. The Si substrate is oxidized by the injected holes and dissolved by the HF solution at the Si/Ag interface, which is the anode reaction and can be expressed by:

$$Si + HF + nh^+ \longrightarrow H_2SiF_6 + nH^+ + \frac{4-n}{2}H_2 \uparrow \qquad 2.2$$

In this manner, arrays of Si nanowires in the areas without Ag coverage can be formed with precisely controlled dimensions.

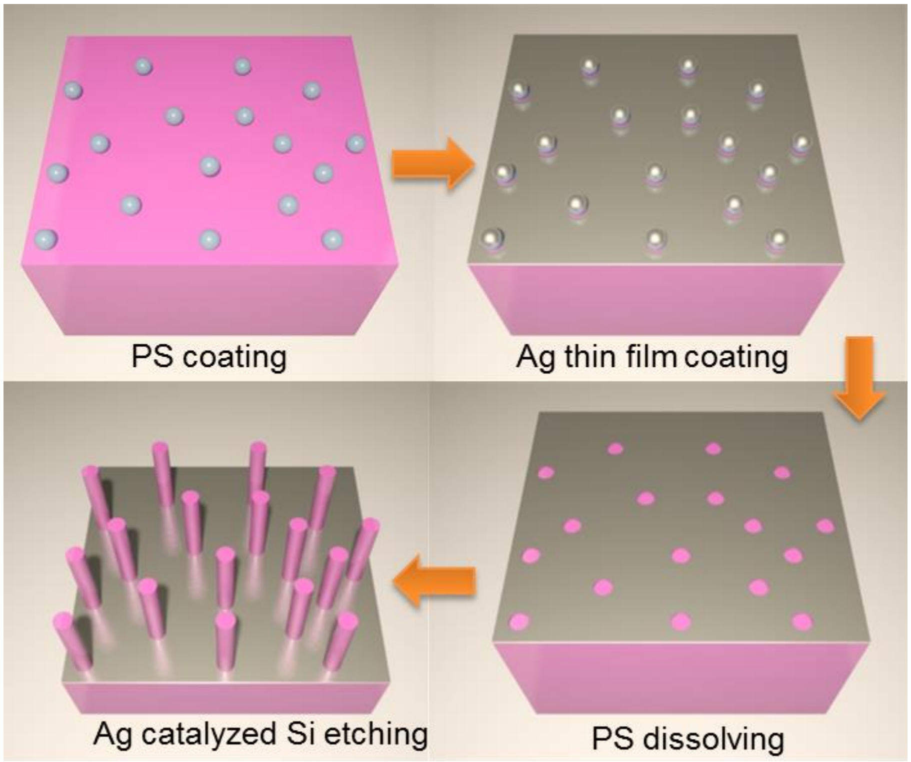

Scheme 2.1 Fabrication of silicon nanowires.

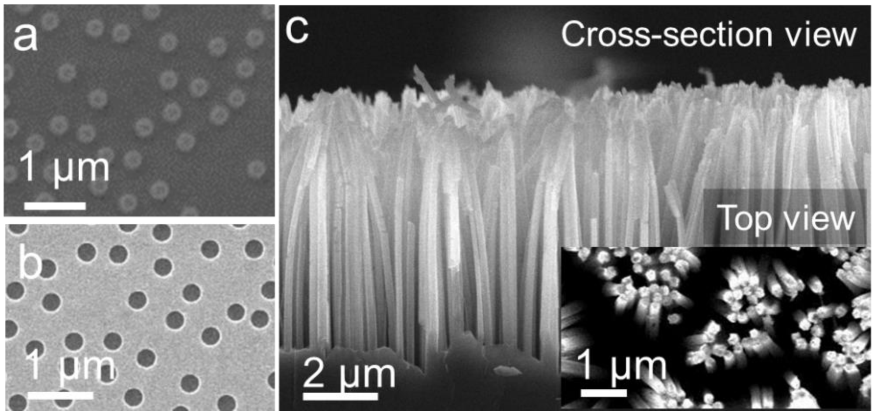

Figure 2.5 SEM images of (a) 200 nm diameter PS nanospheres dispersed on a silicon wafer. (b) Ag film on a silicon wafer with 200 nm diameter holes after removal of PS nanospheres. (c) Cross-section and top view SEM images of Si nanowires fabricated by the colloidal-assisted catalytic etching method in Scheme 2.1.Si nanowires have uniform diameters of 200 nm.

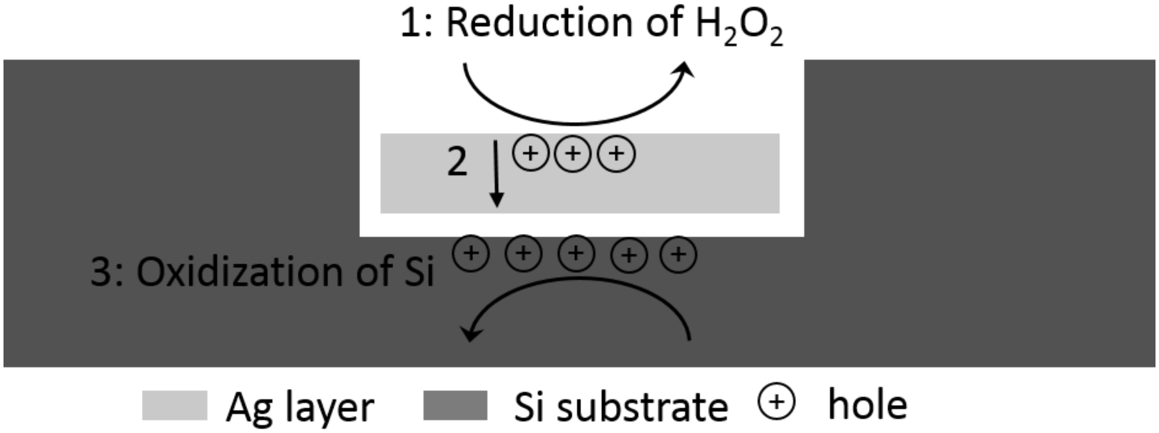

Scheme 2.2 Scheme of Ag-assisted chemical etching process. The numbers illustrate steps described in the text.

2.3 SYNTHESIS OF AU NANOWIRE ARRAYS AND COMPOSITE NANOCAPSULES

Localized surface plasmon resonance (LSPR) is an optical phenomenon generated by the interaction between an incident light and the electrons in the conduction band of nanoparticles. Thus interaction produces the collective oscillation of electrons with a resonance frequency which strongly depends on the nanoparticles' composition, geometry, size as well as the dielectric environment. LSPR greatly enhances the *E*-field in confined locations surrounding the nanoparticles which is widely applied in Surface enhanced Raman scattering (SERS), metal-enhanced fluorescence (MEF), and plasmon energy transfer (PET). Tremendous efforts have been made in synthesize different types of metal nanoparticles, including wet chemical synthesis, top down lithography method, selective etching method, bio-assisted fabricated method.

In this session, I will discuss the fabrication of metal nanowires, nanogap structure and nanocapsules structures based on the electrochemical deposition method.

2.3.1 Fabrication of Au Nanowires

Au nanowires are electrochemical deposited in an anodic aluminum oxide (AAO) template via a typical three-electrode cell setup. A 500 nm Cu layer is coated on the backside of an AAO template via electron-beam deposition at a base pressure of 5×10^{-6} Torr and works as the working electrode; Pt wire servers as the counter electrode, and Ag/AgCl/Sat. KCl works as the reference electrode (Scheme 2.3). An AAO template is sealed against an O-ring during deposition to prevent the leaking of electrolyte. Au nanowires are electrochemical deposited from commercially available cynide based electrolyte (434 HS RTU, Technic Inc.). The diameter of the nanowires can be controlled by the size of the AAO template from tens of nanometers to 300 nm, and the length of the Au nanowires is determined by the amount of electric charge passing through the circuit from hundreds of nanometers to a few micrometers as show in Fig. 2.6. After the electrochemical deposition, the Cu layer is etched by the Cu etchant, and the AAO template is dissoved in a 2 M NaOH solution. Then, Au nanowires are resuspended and sonicated in ethanol and deionized (D. I.) water alternatively twice before redispersed in D. I. water. Other types of nanowires such as Ag nanowires, Ni nanowires, also can be synthesized by this method.

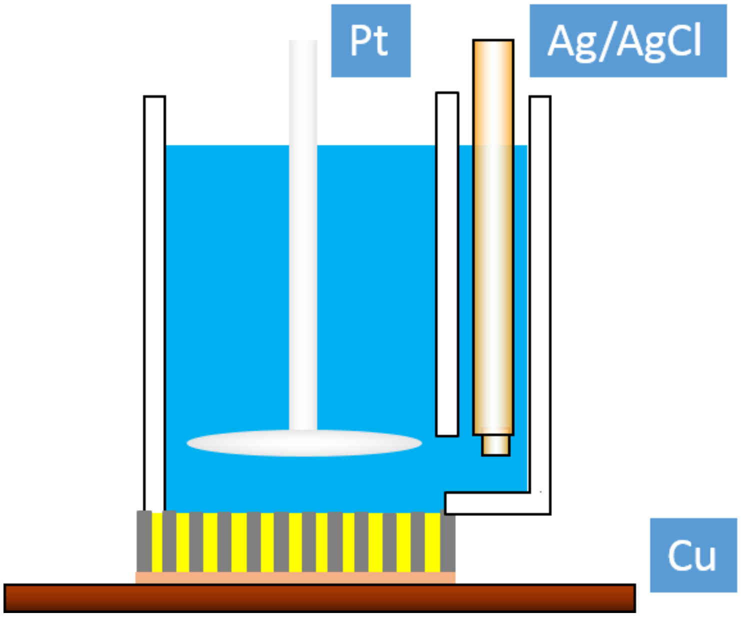

Scheme 2.3 A three-electrode electrochemical deposition setup.

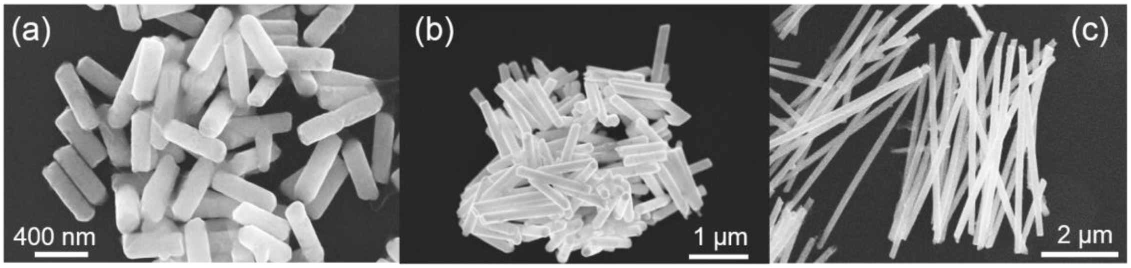

Figure 2.6 SEM images of Au nanowires with different lengths: (a) 500 nm Au nanowires, (b) 1 μm Au nanowires, and (c) 5 μm Au nanowires.

2.3.2 Fabrication of Nanogap Structures

Nanogap structures are synthesized based on the electrochemical deposition method. Instead of only depositing Au into the AAO template, here, we electrochemical deposit multi-segment Au/Ni/Au nanowires. Au segment and Ni segment are deposited alternatively from cynide based electrolyte and $NiCl_2$ based electrolyt. The length of each segment are well controlled by tuning the electric charge passing through the circuit. Multi-segment Au/Ni/Au nanowires with 100 nm and 40 nm Ni segment are successfully fabrication in this manner. Next, a layer of SiO_2 is coated on the multi-segment Au/Ni/Au nanowires via hydrolysis of tetraethyl orthosilicate (TEOS, Alfa Aesar, 99.999+%) in a mixture solution of ammonia (Fisher Scientific, Certified A.C.S. Plus), ethanol (3 ml, Pharmco-aaper, ACS/USP grade), and deionized water (1.8 ml) for 1 hour. Depending on the volume ratio between TEOS and ammonia, the thickness of the silicon layer can be tuned from 20 nm to 200 nm. After washing the obatined nanowires in D. I. water and ethanol for 2 times, respectively, the nanowires are then etched in the nitric acid solution for 30 mins to remove the Ni segments and generate the nanogap structure as shown in Fig 2.7 .

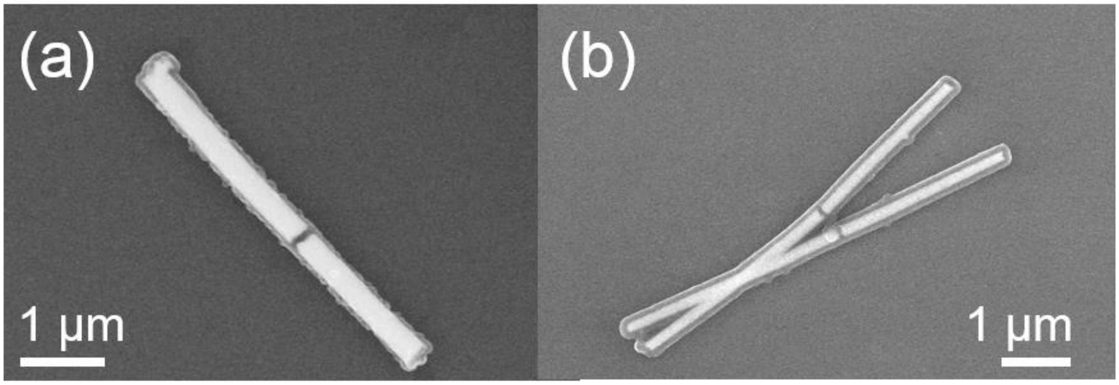

Figure 2.7 SEM images of Au/Ni/Au nanogap structures with a gap size of (a) 100 nm and (b) 40 nm.

2.3.3 Synthesis of Nanocapsules

As mentioned in Chapter 1.2.3, the practical applications of SERS for biochemical detection remain a grand challenge because: (1) it is extremely difficult to obtain a large number of hotspots for sensitive and reproducible detection; (2) it is arduous to achieve ultra-sensitivity detection of a single/few molecules; (3) it is challenging to assemble the hot-spots at designated positions for location predicable sensing; and (4) it remains a grand challenge to directly test the Raman signal from the suspension with high sensitivity.

To address these issues, we economically designed and synthesized SERS nanocapsules and assembled them into ordered arrays via electric fields for ultrasensitive and location-predictable biochemical sensing by using Raman spectroscopy. The nanocapsules consist of a tri-layer structure with a gold nanowire in the core, a thin silica layer on the surface of the nanowire core, and high-density Ag nanoparticles (NPs) grown on the silica layer providing Raman-sensitive hot spots (Scheme 2.4). Each layer in the nanocapsule serves for a specific purpose: the inner metallic nanowire core can be readily polarized in electric fields and manipulated by dielectrophoretic force[127]; the silica layer supports the synthesis of the Ag NP arrays, which also effectively eliminate possible plasmonic quenching between the Ag NPs and the metallic nanowire. The Ag NPs in the outmost surface have optimized size, density, and uniformity and can effectively detect Rhodamine 6G molecules dried on the surface with single molecule sensitivity[127b, 128].

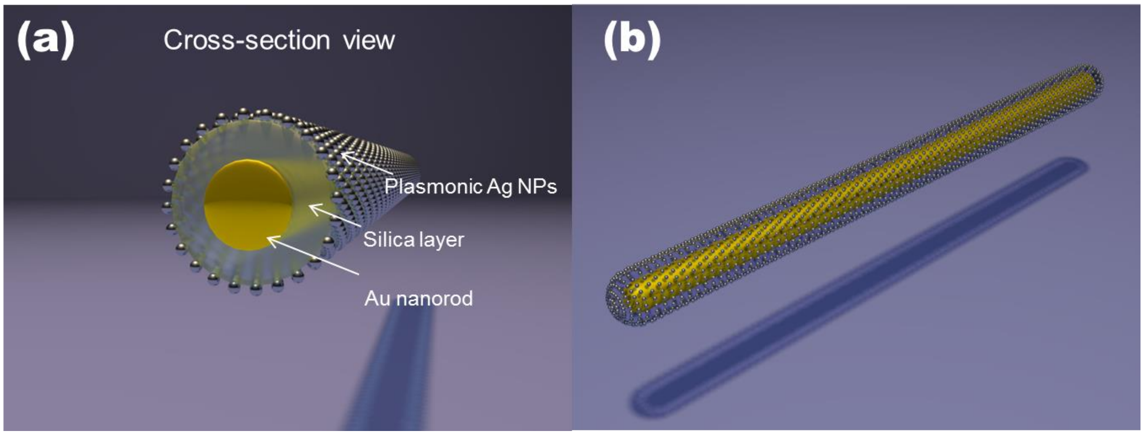

Scheme 2.4 (a) Cross-section schematic diagram of a nanocapsule where a metallic Au nanowire serves as the core, a silica layer grown on the surface of the metal core support the Ag NPs growth and Ag NPs uniformly grow on the silica layer. (b) Side view scheme of a nanocapsule.

The fabrication of nanocapsules starts with the electrochemical deposition of Au nanowires in AAO templates. As described above, Au nanowires are electrodeposited from commercially available cynide based electrolyte (434 HS RTU, Technic Inc.). Billions of nanowires can be fabricated at a time with length of 8.5 μm and diameter of 300 nm as shown in Fig.2.8a. Next, a 180 nm thick SiO_2 layer (Fig 2.8b) is coated on the surface of Au nanowires via hydrolysis of tetraethyl orthosilicate (TEOS, 0.8 ml, Alfa Aesar, 99.999+%) in ammonia (0.2 ml, Fisher Scientific, Certified A.C.S. Plus), ethanol (3 ml, Pharmco-aaper, ACS/USP grade), and deionized water (1.8 ml) mixture solution under sonication for 1 hour. Finally, Ag NP arrays are synthesized on the surface of silica by mixing $Au@SiO_2$ nanowires with freshly prepared 0.06 M silver nitrate ($AgNO_3$, ACROS Organics, 99.85%) and 0.12 M ammonia, stirring for 1 hour before adding polyvinylpyrrolidone (PVP, 10 ml of 2.5×10^{-5} M in ethanol, Sigma-Aldrich, M_w=40000) to promote the growth of Ag NPs at 70 ^{o}C. After 7-hour reaction, dense Ag NPs were obtained on the entire surface of the nanocapsules as shown in Fig. 2.8c and Fig 2.8d.

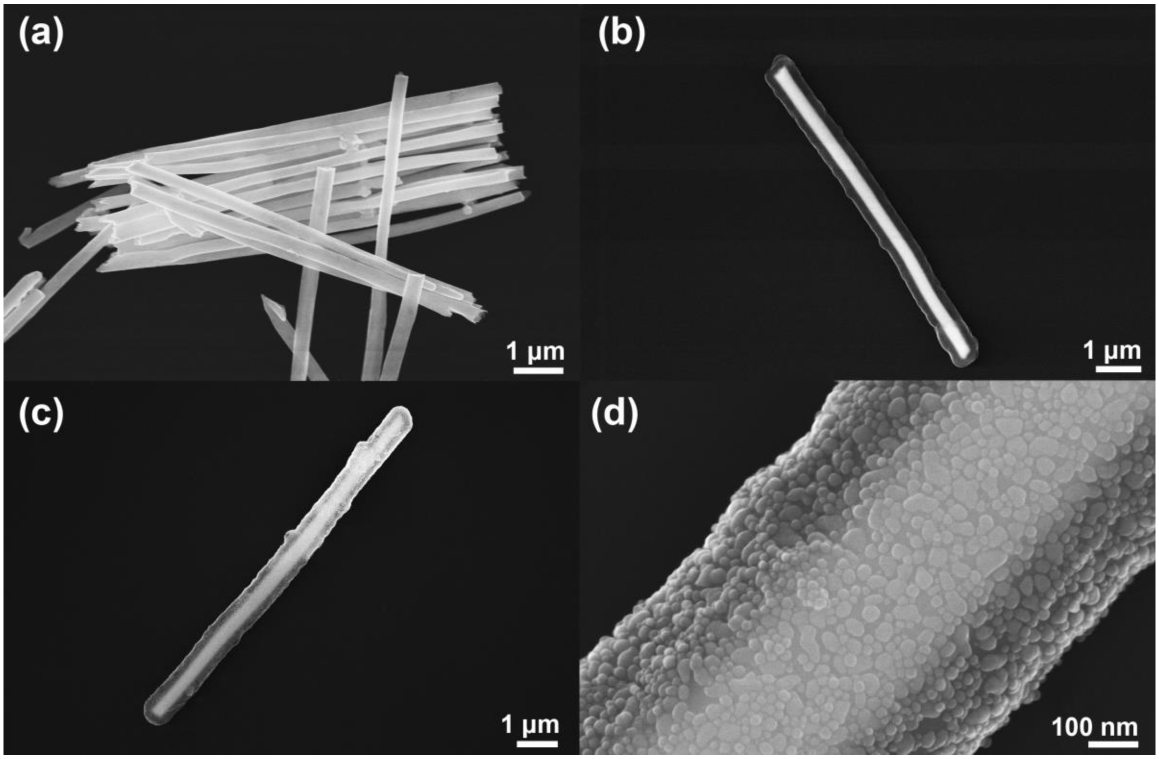

Figure 2.8 SEM images of (a) arrays of Au nanowires with an average length of 8.5 µm and diameter of 300 nm, (b) Au nanowire encapsulated by a 180 nm thick silica layer, (c) Au/silica nanocapsules coated with Ag NPs (d) the zoom-in images of the nanocapsule.

In order to confirm that the outmost layer are Ag NPs, the energy dispersive spectroscope analysis (EDS) is conducted. From the EDS mapping and spectrum, we can clearly confirm that the outermost layer are Ag NPs. (Fig 2.9)

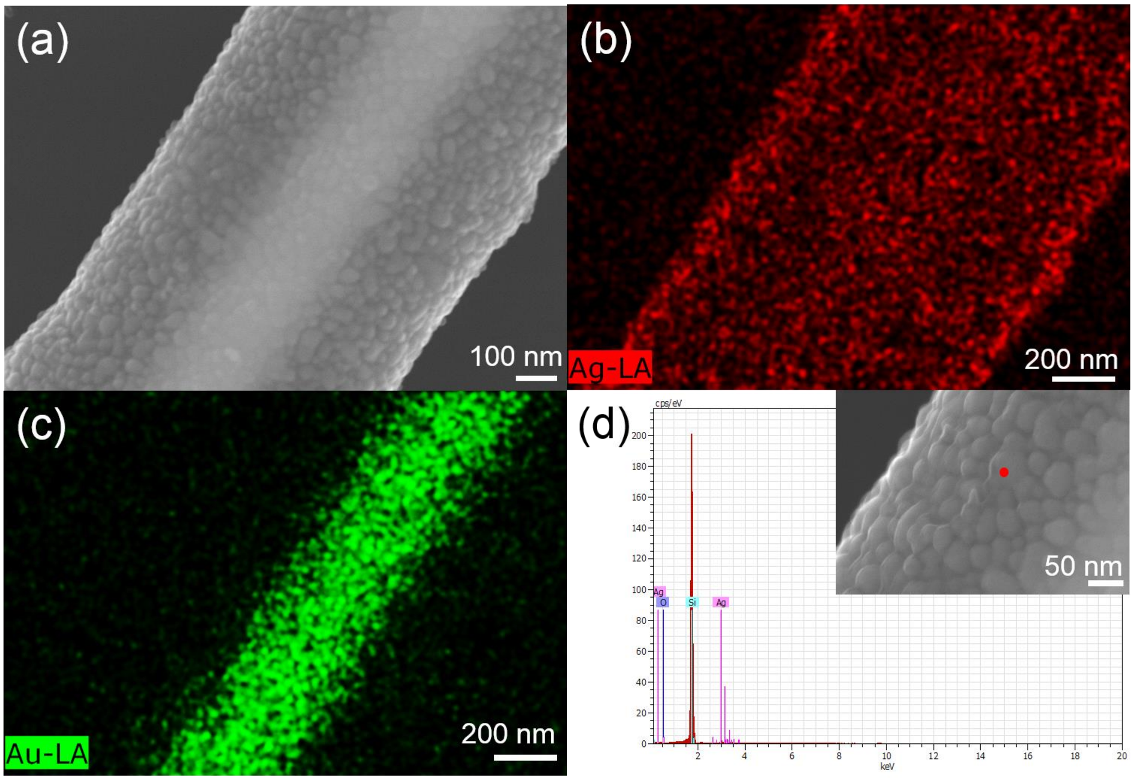

Figure 2.9 (a) SEM image of nanocapsules, (b) EDS mapping of element Ag and Au (c). (d) EDS spectrum detected from the outmost layer of a nanocapsule, the red dot in the inset shows the location where the test was conducted.

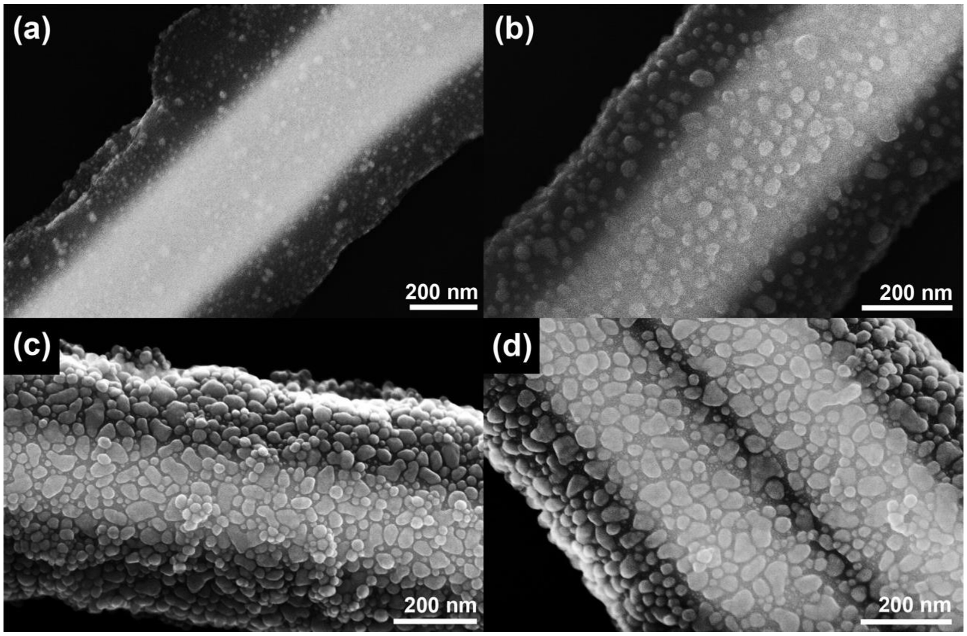

Figure 2.10 SEM images of nanocapsules fabricated at different conditions with reactant concentrations and volumes as: (a) $AgNO_3$ (0.06 M, 350 µl): NH_3•H_2O (0.12 M, 175 µl), (b) $AgNO_3$ (0.06 M, 400 µl): NH_3•H_2O (0.12 M, 200 µl), (c) $AgNO_3$ (0.06 M, 500 µl): NH_3•H_2O (0.12 M, 250 µl), and (d) $AgNO_3$ (0.06 M, 600 µl): NH_3•H_2O (0.12 M, 300 µl).

Since SERS enhancement highly depends on the sizes of Ag NPs, their junctions, and NP distribution[129], we systematically varies the reaction conditions to tune the morphology and dispersion of Ag NPs As shown in Fig. 2.10a-b, if the volumes of $AgNO_3$ (0.06 M) and NH_3•H_2O (0.12 M) are relatively low (350 µl: 175 µl or 400 µl: 200 µl) when mixed with 400 µl Au/SiO_2 nanowire suspension in D. I. water, the Ag NPs grow sparsely on the surface of the nanocapsules. If the volumes of $AgNO_3$ and NH_3•H_2O are increased to 500 µl: 250 µl or 600 µl: 300 µl, dense arrays of Ag NPs can be fabricated uniformly along the length of the nanocapsules as shown in Fig. 2.10c-d. The sizes of Ag NP and junctions are 30 ± 13 nm and 2.00 ± 0.5 nm, respectively, for reactants of $AgNO_3$ (500 µl) and NH_3•H_2O (250 µl). When the volumes of $AgNO_3$ and NH_3•H_2O are changed to 600 µl: 300 µl, the sizes of Ag NPs and junctions increased to 39 ± 13 nm and 2.5± 0.7 nm, respectively. The detailed SERS characterization of these nanocapsules are elaborated in Chapter 3.2.

In Chapter 3, we will discuss the manipulation and assembling of the nanocapsules into large ordered arrays by using electric fields for applications in enhanced SERS detection.

Chapter 3: Precision Manipulation and Assembling of Nanoparticles into Hybrid Nanosensing Devices for High Performance Biochemical Detection‡

In the following, I will discuss three projects that I have focused on in using electric fields (introduced in Chapter 1) to manipulate and assemble various designed nanoparticles such as nanowires, quantum dots, and composite nanocapsules (discussed in Chapter 2) for applications in high-performance biochemical sensing devices. The biodetection will be explored by using optical spectroscopies such as fluorescent and Raman techniques (introduced in Chapter 1).

3.1 LOCATION DETERMINISTIC BIOSENSING FROM QUANTUM-DOT-NANOWIRE ASSEMBLIES

As introduced in Chapter 1, in the last decade, considerable research interest was focused on applying semiconductor quantum dots (QDs) for bioimaging,[130] sensing,[131] and therapeutic delivery[132] due to their tunable sizes and unique optical properties.[1] Compared to traditional organic dyes, semiconductor QDs exhibit higher fluorescent brightness and better resistance to photo-bleaching due to the quantum confinement effect and chemical stability. The colors of QDs can be systematically tuned from the visible to infrared optical regime by varying the sizes and material compositions. The wide absorption band and large stokes shifts make it possible to stimulate QDs of different colors simultaneously by a single excitation source for optical barcoding of biomolecules.[2] These unique properties

---

‡ Portions of this chapter have been previously published in C. Liu, K. Kim and D. L. Fan, Applied Physics Letters,105, 083123 (2014); C. Liu, X. B. Xu and D. L. Fan, ASME-Journal of Nanotechnology in Engineering and Medicine, 5, 040906, (2015)

were explored for imaging and tracking extracellular events, including cellular motility,[3a, 133] protease activity,[4b, 134] and signal transduction.[5] They were also applied as nanosensors for detection of viruses,[6] cytokines,[7] and pH variations.[8] Nevertheless, the applications of QDs as extracellular biosensors were still largely conducted in bulk colloidal suspensions, which present considerable difficulties in sensing a minute amount of bioanalyte. A breakthrough was made by Wang et.al.,[131] who innovatively coupled fast optical detection, FRET of QD-organic dye hybrids, and microfluidics for unambiguous sorting DNA molecules at a concentration as low as 0.48 nM. Although sensitive and specific, such a method relies on the optical detection of fast flowing QDs and thus requires complex optical instrumentation. It is highly desirable if the QDs can be registered at designated locations for position-predicable optical analysis and sensing.

In this dissertation, I investigated controllable manipulation and assembling of QD-nanowire hybrid nanostructures in suspension by electric fields and applied the assemblies for location deterministic biochemical detection. By applying an external AC *E*-field on the designed microelectrodes, we precisely manipulated and positioned bio-functionalized semiconductor QDs on the tips of aligned Au nanowire arrays. The manipulation mechanism was quantitatively understood and attributed to a synergetic effect of DEP and ACEO. The as-obtained QD-nanowire hybrids operate uniquely by actively focusing bioanalytes to QDs with the *E*-field, followed by biodetection after the *E*-field removal, which offered substantially improved detection efficiency with a sensitivity of 20 nM (Cy5 labeled biotin molecules), in additional to the position deterministic rationality. This work could be a critical step towards a rational bottom-up approach for fabricating various QD-based biomedical devices.

Au nanowires (NWs) (300 nm in diameter, 5 μm in length), fabricated by electrochemical deposition into nanoporous templates, were assembled into aligned arrays by electric (*E*) fields and applied for attracting and positioning QDs. Water soluble CdSe/ZnS QDs (525 nm in emission, Invitrogen Inc.) were used for the investigation. The QD-nanowire hybrids were manipulated and assembled in a polydimethylsiloxane (PDMS) well in deionized (D.I.) water by an AC *E*-field with a frequency of 50 kHz to 2 MHz generated from strategically designed interdigital microelectrodes (gaps of 20-50 μm). The *E*-field was controlled by a waveform generator (Agilent 33250A) and the peak to peak voltage was set at 20 V.

Upon application of the *E*-field, randomly suspended Au NWs (concentration: 2.2×10^{7}/ml) were swiftly attracted, aligned and assembled on the patterned microelectrodes as shown in Fig 3.1. The chaining lengths of Au NWs depend on the applied AC frequency.[135] At 70 kHz, a single layer of nanowires can be formed with an average length of 5.46 μm. The length monotonically increased with the AC frequency, and reached an average value of 12.33 μm at 800 kHz.

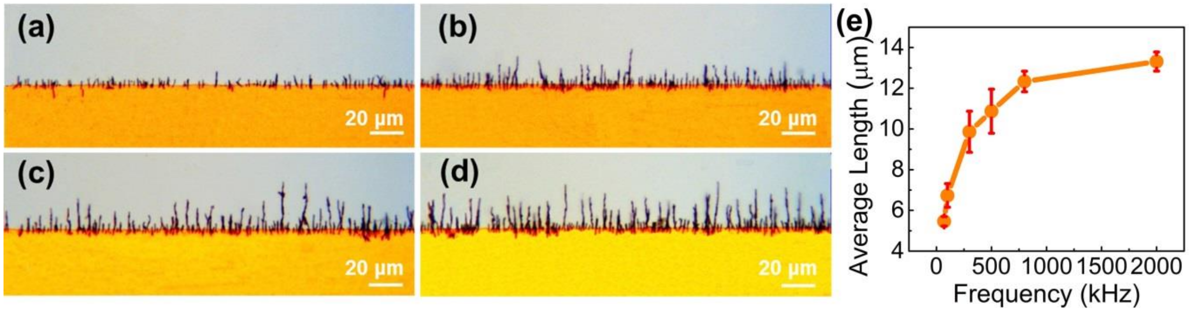

Figure 3.1 Au nanowires (5 µm in length, 300 nm in diameter) attracted and aligned on parallel microelectrodes at frequencies of (a) 50 kHz, 20 V, (b) 300 kHz, 20 V, (c) 500 kHz, 20 V, and (d) 800 kHz, 20 V. (e) The average chaining length as a function of the applied AC frequency.

The transportation and assembling of nanowires can be attributed to the dielectrophoretic (DEP) force, resulting from the interactions between the *E*-field and the electrically polarized nanoentities.[136] For a nanowire, which can be approximated as a prolate ellipsoid; the DEP force is given by[137]

$$F = p \cdot \nabla E = \frac{1}{3}\pi r^2 L \varepsilon_m Re(K) \nabla E^2, \qquad 3.1$$

where $p = \frac{2}{3}\pi r^2 L \varepsilon_m Re(K) E$ is the induced dipole moment on nanowires, *r* and *L* are the radius and length of nanowires, ε_m is the dielectric constant of the medium, and *Re(K)* is the real part of Clausius-Mossotti factor of the nanowire. The transport and alignment orientations of nanowires are along the directions of the *E*-field gradient and the *E*-field, respectively.[138] The distinct degree of the chaining effect at different AC frequencies (Fig 3.1) is due to the unique electric interactions among polarized nanowires, where the electric dipole moment *p*, proportional to *Re(K)*, is a frequency dependent factor. The chaining force between two polarized nanoparticles (F_c) is proportional to E^2 ($F_c \sim E^2$).[139] The number of chained particles, simplified as spheres, can be calculated according to $N = c\sqrt[3]{p_{eff}}$, where c is a constant and p_{eff} is the effective electric polarization moment.[137] The value of p_{eff} highly depends on the electric properties of the nanowires and the suspension medium, as well as the quality of the electric contact between neighboring nanoparticles. In our experiments, we can readily align and assemble a layer of single nanowires on the edges of the microelectrodes at 70 kHz and 20 V.

Next, the assembled nanowires were applied for positioning the semiconductor QD nanosensors. We dispersed the QDs (0.1 nM) in the suspension of the assembled Au nanowires in an AC *E*-field of 50 kHz and 20 V. As soon as the *E*-field was applied, the QDs coherently moved and circulated from the edges to the top of the microelectrodes, and some docked on the tips of nanowires [Figure 3.3a, the QDs transported on top of the microelectrode away from the electrode edges and moved upward (blurred image) until disappeared]. An array of QDs can be assembled on the tips of the aligned nanowires in a few minutes (Figure 3.2). During the assembling process, more than one QD could be attracted to the tips of nanowire which result in larger and brighter QDs. In principle, these QDs could also form the pearl-chain structures on the tips of Au nanowires, however, it is difficult to directly confirm the pearl-chain formation via microscope observation due to the ultrasmall diameters of QDs (< 10 nm).

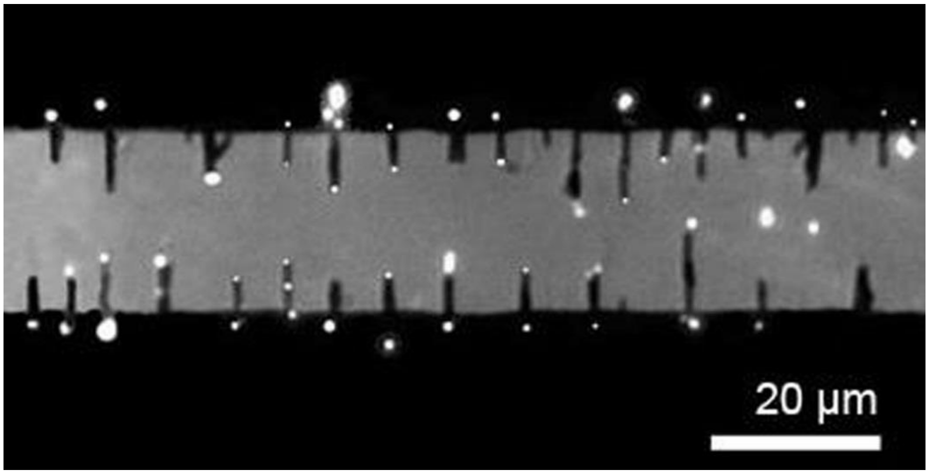

Figure 3.2: Quantum dots can be precisely positioned on the tips of arrays of nanowires by the AC *E*-fields.

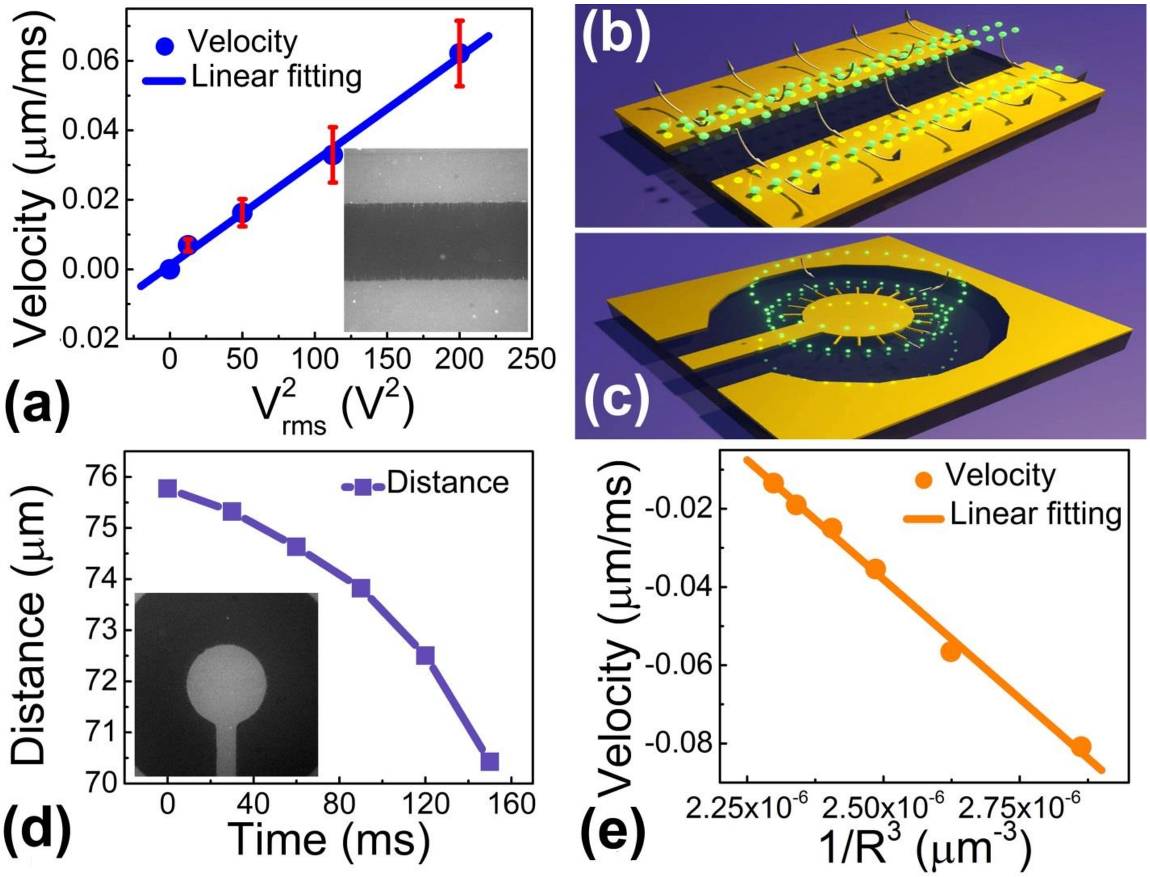

Figure 3.3: (a) The velocities of QDs linearly increase with V_{rms}^2, inset: snapshot of QD movement due to ACEO flows. (b) Schematic diagram of ACEO flows for QD manipulation. (c) Schematic diagram of manipulation QDs in the circular microelectrodes. (d) Distance of a QD to the center of the inner electrode versus time. Inset: snapshot of the circular microelectrode (e) Velocity of QD increases linearly with *1/R*^{3}.

The assembling of QDs *cannot* be explained simply by the DEP effect [140] It is known that DEP force increases with the volume of objects.[141] By the DEP force alone, it is extremely inefficient to move QDs with a diameter less than 10 nm over a region of tens of micrometers, where estimation shows that the speed of QDs should be only a few nm/s. Although the ultrafine tips of Au nanowires can enhance the *E*-field in their vicinities substantially, such an effect is highly localized and effective only in the vicinity of nanowires. A different electrokinetic mechanism other than the DEP force must be playing a role in circulating QDs around the edges of the microelectrodes, which brings QDs closer to the nanowires.

Among many electrokinetic phenomena, the alternating current electroosmosis (ACEO) effect drew our attention. ACEO results in electroosmotic flows circulating around microelectrodes due to the interactions of the *E*-field and the electrical double layers next to the electrodes. The fluid velocity in the horizontal direction is given by[96]:

$$v_{fluid} = \varepsilon_m V_{rms}^2 / [\eta(1+\delta)L\left(\frac{\omega}{\omega_c}+\frac{\omega_c}{\omega}\right)^2], \qquad 3.2$$

where V_{rms} is the root mean square of applied voltage; ε_m and η are the permittivity and viscosity of the suspension medium; L is the electrode spacing; δ is the capacitance ratio of the diffusion and compact layers (assumed as constant for both); ω_c and ω are the peak and applied *E*-field frequency, respectively. The movement pattern of QDs exhibits a great similarity with that of nanoparticles under the influence of ACEO effect (Figure 3.3b).[142]

To confirm that the circulating motion of QD is indeed due to the ACEO effect, we characterized the velocities of QDs as a function of the applied voltages from 5 to 20 V at 50 kHz. The velocities were determined from QDs on the top of the parallel microelectrodes. The velocities linearly increase with V_{rms}^2 (Figure 3.3a), agreeing with the relation of $v \sim V_{rms}^2$ given in Eq. 3.2. However, it remains difficult to attribute the high precision assembling of QDs on the tips of nanowires (only 300 nm in diameter) to the ACEO effect.

It is noted that for nanowires attached on parallel microelectrodes in an external *E*-field, the *E*-field strength can be substantially enhanced in the vicinity of the tips of nanowires, which result in a high *E*-field gradient as shown in the simulation in Fig 3.4. The attraction of small objects to the highest *E*-field gradient is a hallmark of positive DEP forces.[138] Our quantitative study of the transport of QDs to the tips of nanowires confirmed such an effect.

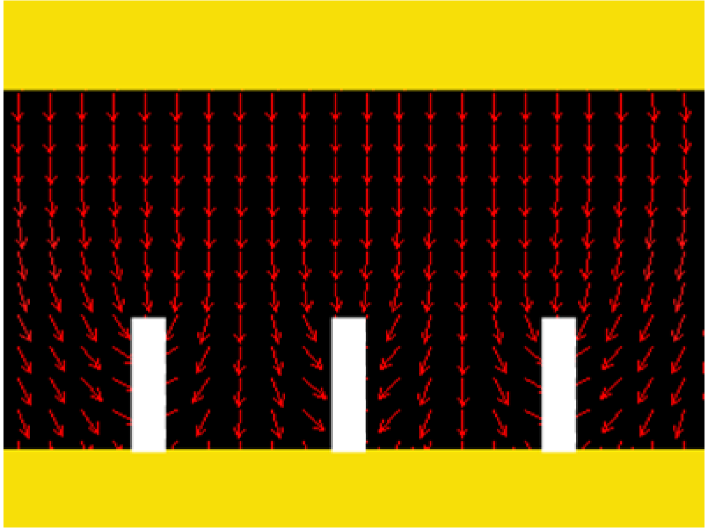

Figure 3.4. Simulation of the distribution of electric fields when nanowires are attracted to the edge of microelectrodes. The parallel electrodes are in yellow, the nanowires are in white, and the electric field lines are in red.

Since there is no analytical solution of the *E*-field distribution around a nanowire, we designed a pair of concentric microelectrodes with inner and outer radii of 65 µm and 200 µm, respectively (Figure 3.3c and d). In such a microelectrode, the DEP force (F_{DEP})

can be analytically obtained, which is proportional to $1/R^3$, given by $F_{DEP} \sim \nabla E^2 \sim 1/R^3$ according to Eq. 3.1, where R is the distance of the nanoobjects to the center of the inner electrode. After attaching the nanowires to the edge of the inner electrode at 70 kHz and 20 V, QDs can be readily assembled on the tips of the nanowires (90 kHz and 20 V) (Figure 3.3d). To clearly determine the nature of the attraction force, we analyzed the motions of QDs when they were a few micrometers away from the tips of nanowires. We consistently found that the velocities of such QDs (v) linearly increase with $1/R^3$. (Figure 3.3e) Given that the viscous drag force (F_{drag}) instantly balances the applied external forces, i.e. $F_{DEP} \approx F_{drag} \sim v$, for nanoparticles in the extremely low Reynolds number regime,[138] the as-observed $v \sim 1/R^3$ accounts for the dependence of $F_{DEP} \sim 1/R^3$. This analysis confirms that the attraction force received by the QD is the DEP force. As a result, the entire assembling process of QD-on-nanowires can be understood quantitatively, where the QDs in the suspension were coherently moved on top of the microelectrodes largely due to the ACEO influence, when they were brought close to the nanowires, the DEP force around the tips of nanowires dominated, attracting and positioning them precisely on the tips of nanowires. This result agrees with previous work on solely QD manipulation,[140] but was achieved in a nanowire-QD system and confirmed in a direct and quantitative manner. Also note that the assembling of QD/nanowire hybrid is highly facile and controllable, which took just seconds to minutes depending on the concentration of QDs.

The QD-nanowire assemblies were applied for position deterministic biochemical sensing, where the nanowires defined the positions of the QD biosensors. Note that in the aforediscussed study, regardless of the applied AC frequencies, the nanowires attached on the edge of microelectrodes were *not* assembled in an order array (Fig 3.1). We also notice that the fluorescent intensity of QDs and organic dyes can be quenched significantly if they directly contact metal surfaces.[143] To resolve these two issues before demonstrating the QD-nanowire assemblies for sensing applications, the surfaces of microelectrodes and Au nanowires were modified with a thin layer of PMMA (MicroChem 950k C2, ~200 nm in thickness) and silica (40 nm), respectively. The presence of the thin PMMA layer can maintain the mobility of Au nanowires attaching on the edges of the microelectrodes and result in an equally-spaced nanowire array due to the electrostatic repulsion between neighboring nanowires in an AC *E*-field (Figure 3.5).[144] The separation between QDs and metal nanowires by the silica coating can precisely tune the fluorescent enhancement of QDs due to the plasmonic Au nanowires, which will be discussed elsewhere.[145] With the above consideration and modification, we obtained an array of evenly spaced QD-nanowire devices at 20 V, 700 kHz. The average distance between neighbored QD-nanowire assemblies was ~ 8.5 μm for a nanowire suspension of 2.2×10^7 /ml and QDs of 0.1 nM (Figure 3.5a and b).

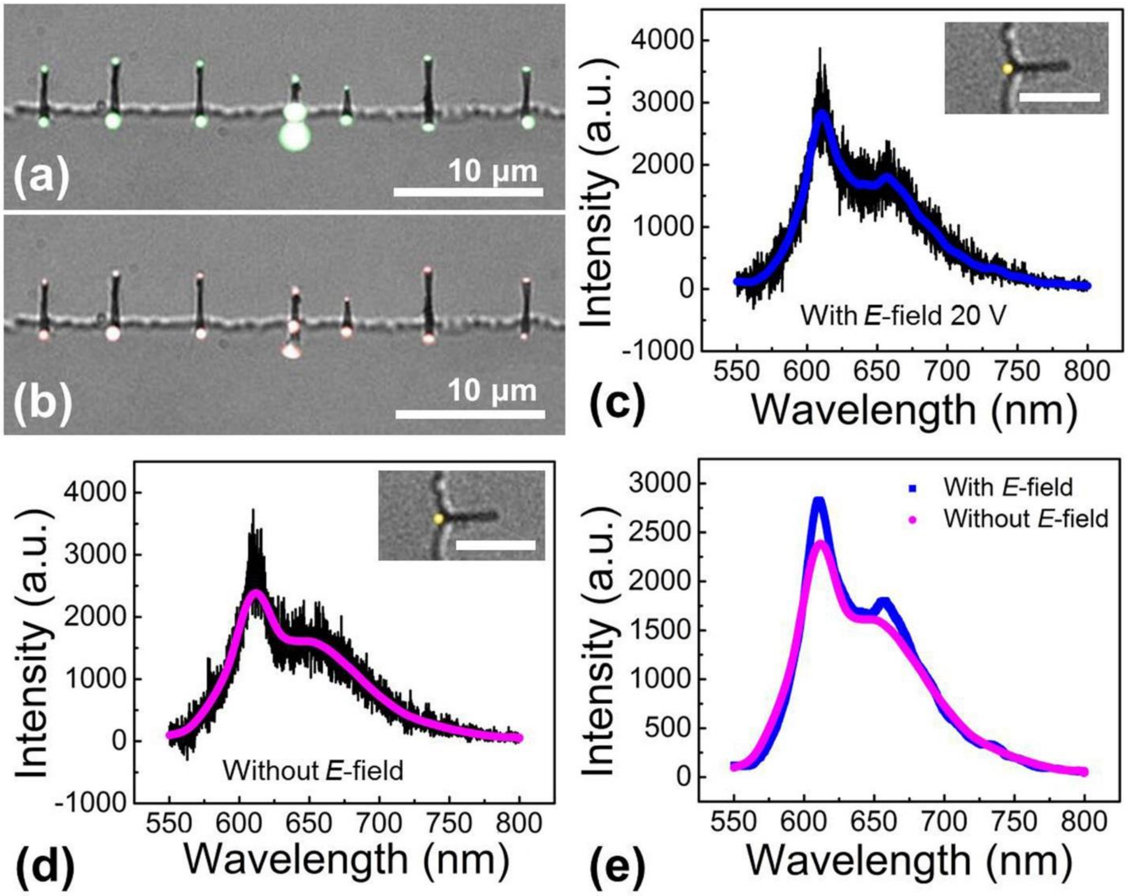

Figure 3.5 Under an AC *E*-field (700 kHz, 20 V), Cy5-biotin molecules can be efficiently focused on the tips of nanowires in suspension, co-localized with QDs coated with streptavidin for enhanced biodetection. (a) Fluorescent images of QDs on an array of assembled Au nanowires taken through a band pass filter of 605 nm (585 nm to 625 nm). (b) Fluorescent images of Cy5-biotin molecules on the same arrays of Au nanowires taken through a 650 nm long pass filter. Fluorescent spectra taken on the nanowire tips when the AC *E*-field is (c) on and (d) off, demonstrating the effective *E*-field focusing and specific conjugation of QD and Cy5-biotin. The insets show the corresponding fluorescent images with pseudocolors. The scale bar is 5 µm. (e) The signals of QD and Cy5 biotin with/without the *E*-field.

The as-obtained QD-nanowire assemblies were demonstrated as nanosensors for detection of biomolecules. Biotin molecules, bonding strongly with streptavidin, are commonly used for device demonstrations.[146] In the experiments, after assembling QDs which conjugated with streptavidin (0.1 nM, emission: 605 nm, Invitrogen Inc.) on the tips of nanowires in an AC *E*-field of 20 V and 700 kHz, Cy5-labeled biotin molecules (200 nM, 4 µL, Nanocs Inc.) were introduced in the same AC *E*-field. In a few minutes, the characteristic fluorescent signals of Cy5-biotin can be detected on the tips of nanowires, co-localized with that of QDs (Figure 3.5a and b). When the concentration of Cy5-biotin was reduced to only 20 nM, there were still 52.6% QD on the tips of nanowires showed the co-localized signals of Cy5-biotin. Note that the co-localization of QDs and biotin occurred in just a few minutes after the application of the *E*-field, which is much faster than those demonstrated previously, where a conjugation time of at least 30 min has to be taken before signals of both molecules can be successfully detected.[147] This suggests that the DEP force not only assemble QDs at the tips of nanowires as aforediscussed, but also could focus biomolecules, such as biotin, to the tips of nanowires to enhance the detection efficiency.

To confirm this understanding, we performed a series of control experiments. Cy5-labeled biotin of various concentrations from 200 pM to 20 pM was introduced to a simple array of assembled nanowires (without presence of QDs) at 700 KHz and 20V. In a few minutes, biotin could be readily detected at the tips of nanowires from both the fluorescence imaging and spectroscopy of Cy5 (Fig 3.6). This experiment showed that indeed analyte molecules can be concentrated at the tips of nanowires due to the AC *E*-field.

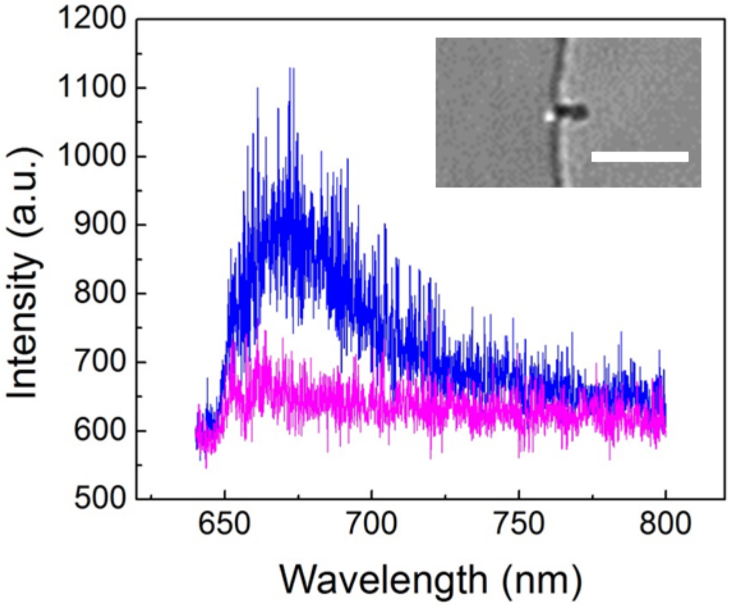

Figure 3.6 Direct attraction of Cy5-biotin in suspension (20 pM) on the tips of the Au nanowires. The fluorescent signals (in blue) of Cy5-biotin were detected from the tips of Au nanowires in an *E*-field of 700 KHz, 20 V. The fluorescent signals of the background Cy5-biotin solution (20 pM) is in magenta. Inset: the fluorescent image of Cy5-biotin on the tips of Au nanowires; scale bar: 5 µm.

It is critical to know if the molecules co-localized with QDs are the sought-after biotin molecules, which should specifically bond to the streptavidin-coated QDs. After incubation for 30 min, the *E*-field was carefully removed to release the non-specific molecules. Most QD-nanowire assemblies still remained (90%), which could be due to the non-specific bonding of functionalized QDs and nanowire tips. For a Cy5-biotin concentration of 20 nM and in more than 15 tested devices, after the *E*-field release, 55.6% QD-nanowires retained the original co-localized Cy5 signals with a slight decrease in the intensity of both QDs and Cy5-biotin (Figure 3.5e). In comparison, at the same condition, if by using bare QDs without streptavidin (QD 525), majority Cy5 labeled biotin disappear from the QDs on the tips of nanowires after the *E*-field release (Figure 3.7). Only ~14.3% QDs retained the original signals of Cy5-biotin, which is substantially lower than that obtained from the streptavidin coated QDs (55.6%). This result demonstrates that the QD-nanowire system can detect desirable molecules due to the specific conjugation between QDs and the analyte molecules.

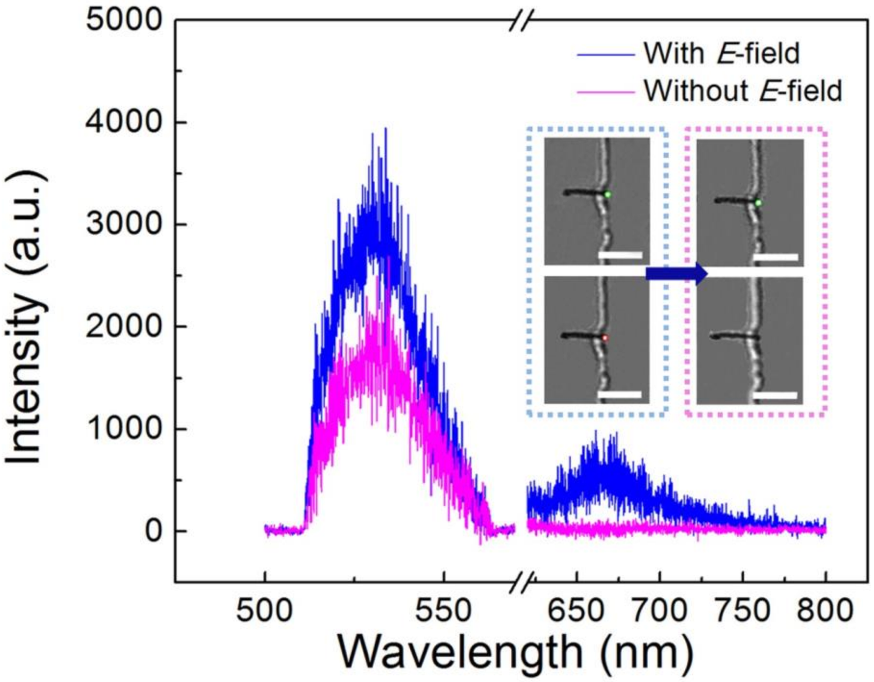

Figure 3.7 Control experiments: under the AC *E*-field (700 kHz, 20 V), fluorescent spectrum (in blue) shows both QDs (without streptavidin, emission: 525 nm, 535 nm band pass filter from 505 nm to 560 nm) and Cy5-biotin molecules (emission 670 nm, 532 nm long pass filter) at the tips of nanowires. After removal of the AC *E*-field, the signal of Cy5-biotin disappeared due to the detachment from the QDs (in magenta). Inset on the left: fluorescent images showing both QDs and Cy5-biotin under the AC *E*-field. Inset on the right, fluorescent images after removal of the *E*-field.

As a result, the QD-nanowire sensors operate uniquely by effectively focusing molecules to QDs before detection via specific conjugation. In comparison, if we directly incubate streptavidin conjugated QDs, spin coated on a glass substrate, with Cy5-biotin (20 nM) and detect the co-localized signals at the same conditions, only 17.2% signals showed the conjugation of QD and Cy5, which is much lower than that obtained from the QD-nanowire assemblies. The control experiments further confirm that our devices offer improved biodetection sensitivity (or efficiency) in addition to the merit of location-predictability. The improved sensitivity could be largely attributed to the concentration effect for both QDs and biotin due to the *E*-field. We also note that the plasmonic enhancement from the Au nanowires may improve the detection performance, which will be studied elsewhere.[145]

The devices demonstrated here could inspire new strategy for resolving the intrinsic problem of low throughput of nanosensors.[148] With further investigation and optimization, i.e. application of the 3D electrodes instead of 2D planar electrodes,[149] integration with a microfluidic device, automation of optical analysis, and use of multiple functionalized QDs, the QD-nanowire assemblies could detect various analyte molecules in a rational, sensitive, multiplex, and efficient manner. Among all the aforementioned improvements, it is especially interesting to assemble the nanowire-QD hybrid sensors into 3-D structures in the detection system. The 3-D assembling scheme can enhance the detection efficiency substantially owing to the more effective interaction and focus of analyte molecules to the sensing areas compared to that of the 2-D scheme. This could be achieved by generating

E-fields from designed 3-D electrodes, i.e. those made of a stack of insulator-separated plenary metals. Also note that based on our understanding of the ACEO effect, pressure driven flows, which bring the QDs to the vicinity of the nanowires, could also be employed to assist the assembling of the QD nanosensors owing to the same mechanism as that of the ACEO flows. However, the rate of the pressure driven flows should be controlled to limit the hydrodynamic force lower than the DEP force. Finally, the electric-field assisted QD assembly has its own limitation compared to the previous work,[3] where pattern microelectrodes are indispensable, which requires additional engineering and optimization when integrating with other systems, e.g. microfluidics.

In summary, QDs with a diameter of <10 nm were precisely manipulated and assembled on tips of Au nanowires. The manipulation mechanism was understood quantitatively and attributed to a synergetic ACEO and DEP effect. After modification of the surfaces of the microelectrodes and Au nanowires, the QD-nanowire assemblies can be arranged in an equally spaced array and demonstrated for biochemical detection. The device operated uniquely by focusing analytes to the QD nanosensors before detection via specific biochemical conjugation. Molecules, such as biotin, can be detected unambiguously in a location deterministic manner with much enhanced sensitivity. With further investigation and optimization, such devices could potentially be integrated with microfluidics for position deterministic biochemical sensing. The outcome of this research may not only advance the QD-based sensing technology, but also inspire a potentially scalable approach for fabricating various QD-based nanodevices.

3.2 ELECTRIC-FIELD ENHANCED MOLECULE DETECTION IN SUSPENSION ON ASSEMBLED PLASMONIC ARRAYS BY RAMAN SPECTROSCOPY

As discussed in Chapter 1, in the last decade, the technique of surface-enhanced Raman scattering (SERS) has been intensively studied due to its great potentials for label-free and multiplex detection of biomolecules [21a, 21c, 150], pollutants [25, 151], and chemical warfare agents [23, 152]. When optical light interacts with noble metal nanoparticles, the conduction-band electrons in the nanoparticle can collectively oscillate and generate localized surface plasmon resonance. As a result, substantially enhanced electric fields are created in the vicinity or junctions of the nanoparticles, which are also called hot spots. If the analyte molecules are in the hot spots, their Raman signals can be dramatically increased by 10^8 - 10^{12} times[30], which is sufficient for detecting single molecules of various species [20a, 127b]. Previously, different types of SERS substrates were fabricated including metals with roughened surfaces[17-18], nanowires[51, 153], metal nanoparticles[154], sharp tips[155] and core/shell nanospheres [37b, 156]. However, most SERS detections were carried out by drying analyte solutions on the SERS substrates to force molecules to get into hotspots before the detection. The employed drying methods can be different among individual research groups. Quantitative comparison of these results should be conducted carefully. Given the same employed equipmental conditions, it is highly desirable to directly detect molecules in suspension to accurately evaluate the performances of different SERS substrates, which will also have pivotal implications for SERS biosensing in microfluidics. However, when directly detecting from solutions, we found that with the same SERS substrate, the lowest detection limit of molecules at the same experimental and equipmental conditions, such as Rhodamine 6G (R-6G) and Nile blue - commonly used SERS probes, can be higher by a few orders of magnitudes compared to that from samples with dried molecule probes [127b, 128]. Therefore, it is of great interest to investigate new mechanisms to detect biochemicals directly from solutions with high sensitivity.

Electrokinetic phenomena due to AC and DC electric fields applied on designed microelectrodes has generated immerse interest in manipulation of nanoparticles, live cells and even biomolecules[157]. Recently, it was applied on prepatterned plasmonic substrates, such as Au nanoholes[158], microneedles[159], nanopillars[160], and nanospheres [21d, 161] to focus analyte molecules to the hotspots before optical detection. Nevertheless, most previous efforts either require complex lithography for fabricating SERS-active entities [159-161] or could not precisely control the sizes/junctions of plasmonic particles for high reproducible detection when electric fields are applied [161].

In this work, we report electric-field enhanced molecule detection from an innovative type of SERS-active nanocapsule structures. The nanocapsules can be bottom-up synthesized in a large scale, dynamic assembled into ordered arrays, and offer a large number of hotspots with controlled sizes owing to the unique design of the structures. With optimized AC frequencies, voltages and structure of the microelectrodes, biomolecules, including those having low molecular weights such as Nile blue, can be effectively concentrated on the surface of the nanocapsules. The Raman signal of Nile blue can be improved by 34.4 ± 3.1% after applying the electric field for a few minutes. This work could inspire the next generation microfluidic-based Raman sensing devices.

As mentioned in Chapter 2.3, the nanocapsules consist of a tri-layer structure with a gold nanowire in the core, a thin silica layer on the surface of the nanowire core, and high-density Ag NPs grown on the silica layer providing Raman-sensitive hot spots (Scheme 2.4). The detailed fabrication steps are covered in Chapter 2.3. In addition, in Chapter 2.3, we also demonstrated that by varying the reaction conditions, we can systematically tune the morphology and dispersion of Ag NPs. Here we characterized the corresponding SERS performance.

As aforediscussed, previously SERS characterizations were often conducted by using SERS probes naturally dried on the nanoparticles surfaces. There are many uncontrollable factors during the drying process, which could make it difficult to compare the characterizations obtained by different groups or individuals. In this work, we evaluated the SERS performances by directly immersing the as-prepared nanocapsules in a suspension of a commonly used SERS probes, R6G, with known concentrations (Acros Organics, 99%, 100 µM). A customized Raman microscope equipped with a 633 nm laser was used for Raman characterization. Well reproducible SERS signals were obtained from different nanocapsules synthesized in the same batch of $AgNO_3$ and NH_3•H_2O solution with volumes of 500 µl and 250 µl, respectively (Fig. 3.8a). Such SERS intensity is the highest among all the samples with different volumes of reactants (Fig. 3.8b). It indicates that nanocapsules with an average particle and gap sizes of 30 ±13 and 2.0 ± 0.5 nm, respectively offer the best SERS performance (Fig. 2.10c), which agrees with the simulation results reported in our previous work where the highest electric field in the hotspots is generated from Ag NPs with the narrowest junctions and diameters of 30-50 nm [128].

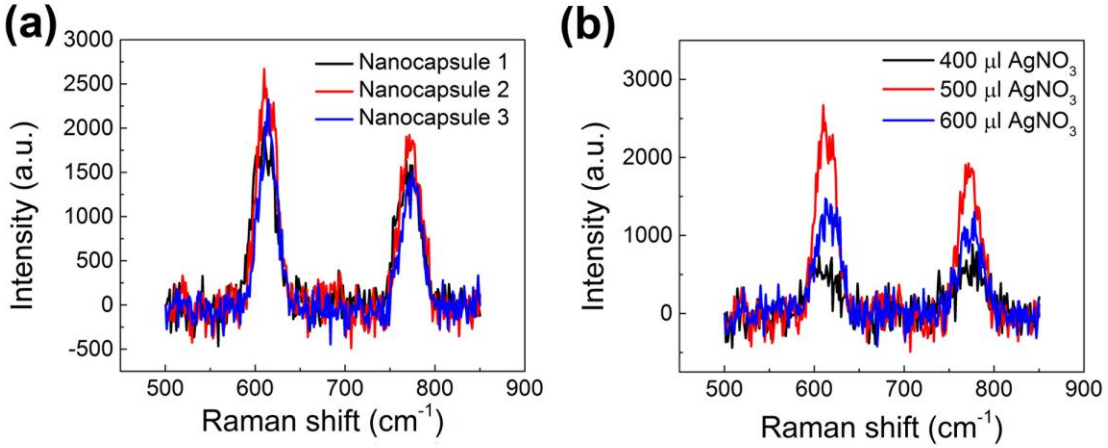

Figure 3.8. Raman detection from nanocapsules in 100 μM R6G suspension. (a) Well repeatable Raman signals from nanocapsules synthesized in the same batch with volumes of $AgNO_3$ and $NH_3•H_2O$ as 500 µl: 250 µl. (b) Comparison of Raman signals from samples fabricated at different conditions with volumes of $AgNO_3$ and $NH_3•H_2O$ as 400 µl: 200 µl (black) 500 µl: 250 µl (red), and 600:300 µl (blue).

Not only providing well reproducible SERS enhancement, the nanocapsules can be efficiently assembled into ordered arrays by electric fields owing to the strategically embedded metallic cores that can be strongly polarized in AC electric fields. Different from previous work, the feature sizes and distribution of the SERS-active components, Ag NPs, remain intact during the manipulation and assembling process[161]. Specifically, before the assembling of nanocapsules, a layer of polymethyl methacrylate (PMMA, MicroChem 950k C2) was spin-coated on the microelectrodes to maintain the mobility of the nanocapsules. Then the nanocapsules were suspended randomly in a Polydimethylsiloxane (PDMS) well. Upon the application of the electric field at 700 kHz and 20 V on the interdigital indium tin oxide (ITO) microelectrodes (gap size: 20 μm), the nanocapsules were swiftly attracted to the edges of the microelectrodes and aligned in the direction of the electric fields as shown in Fig. 3.9. Essentially, they spaced evenly with approximately 6.6 μm due to the electrostatic repulsion in neighboring nanocapsules[144, 162].

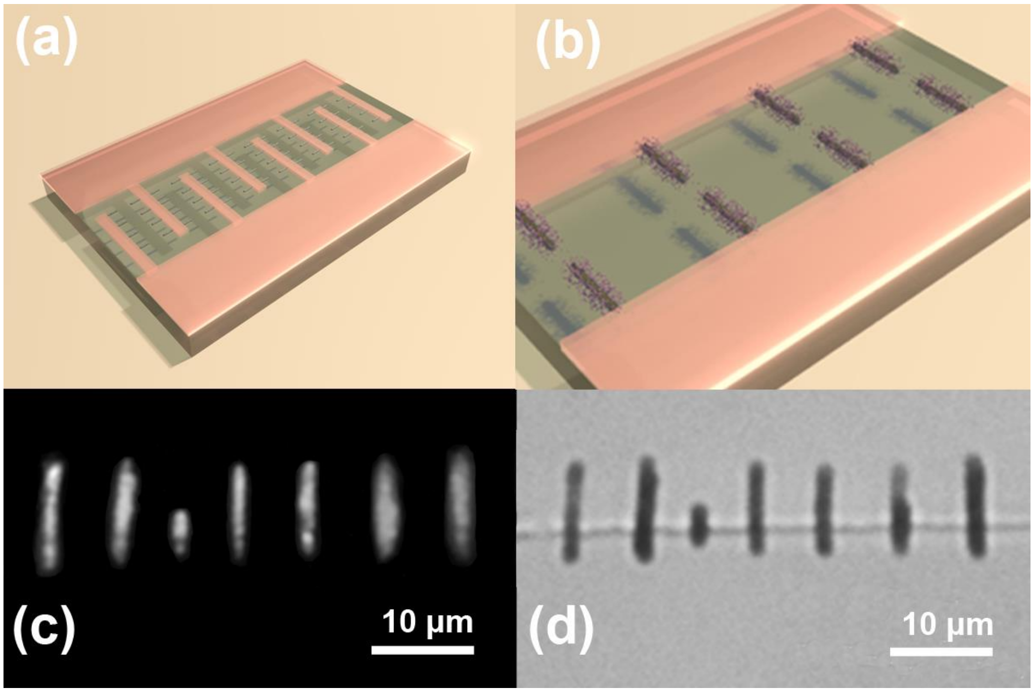

Figure 3.9 (a) Schematic diagram of nanocapsules assembled on interdigital microelectrodes. (b) The attraction of molecule to the nanocapsules with the electric fields. (c) Raman image of Nile blue molecules (with background fluorescence of Nile blue molecules and Ag nanoparticles) from assembled nanocapsule arrays on microelectrodes (enhanced image), and (d) the corresponding optical microscopy image.

The transportation and assembling of nanocapsules can be attributed to dielectrophoretic (DEP) forces resulted from the interaction between the electric field and polarized nanocapsules, given by [137]

$$F = p \cdot \nabla E, \qquad 3.3$$

where the polarization of the nanocapsules (*p*) is proportional to the applied electric fields, and depends on the chemistry and geometry of the nanocapsules. The transport and orientation of the nanocapsules are in the directions of the electric-field gradient and electric field, respectively [138].

After assembling arrays of nanocapsules, we turned off the AC voltages and carefully dispersed 10 μl Nile blue (Alfa Aesar Inc.) solution with a concentration as low as 100 nM into the PDMS well. The Raman images of Nile blue on nanocapsule arrays with fluorescent background of Nile blue and Ag NPs were collected after a 633 nm edge filter as shown in Fig. 3.9c. The corresponding optical image is shown in Fig. 3.9d. Then, the Raman spectra of Nile blue were recorded from the nanocapsules for 300 sec with an integration time of 1 or 2 s from a 50X objective lens before an AC electric field was applied. The peak height at 595 cm^{-1} was used for analysis since it was the most prominent peak and well separated from others (Fig 3.10a). AC electric fields with frequencies ranging from 100 kHz to 1 MHz were studied as shown in Fig. 3.10b. The strongest attraction was achieved at 200 kHz [Fig. 3.10b].

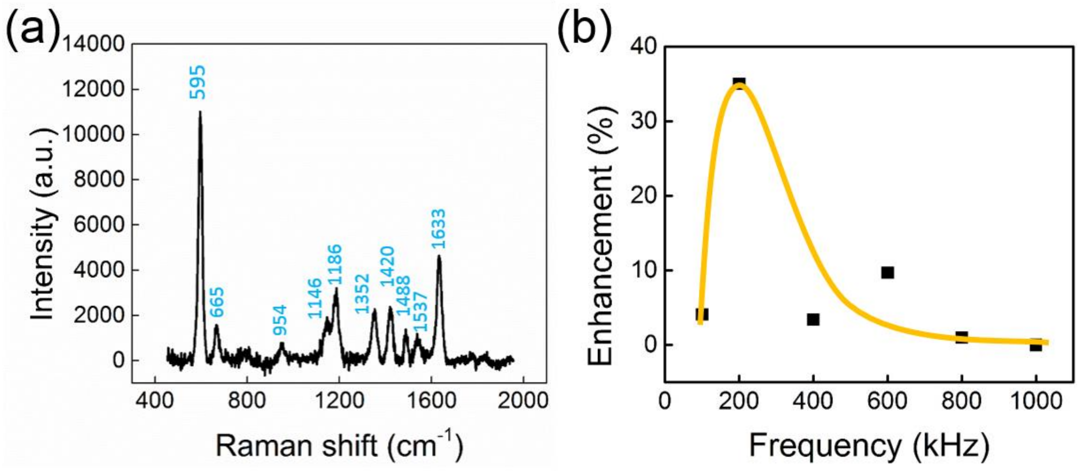

Figure 3.10 (a) Raman spectrum of Nile blue (250 nM) detected from a nanocapsule in solution, which demonstrated that 595 cm^{-1} was the most prominent Raman peak and well separated from others. (b) frequency dependent Raman intensity enhancement at 595 cm^{-1} of Nile blue molecules (100 nM) recorded after applying an electric field at 20 V and 100 kHz to 1 MHz. (The curve in orange is an eye guide.)

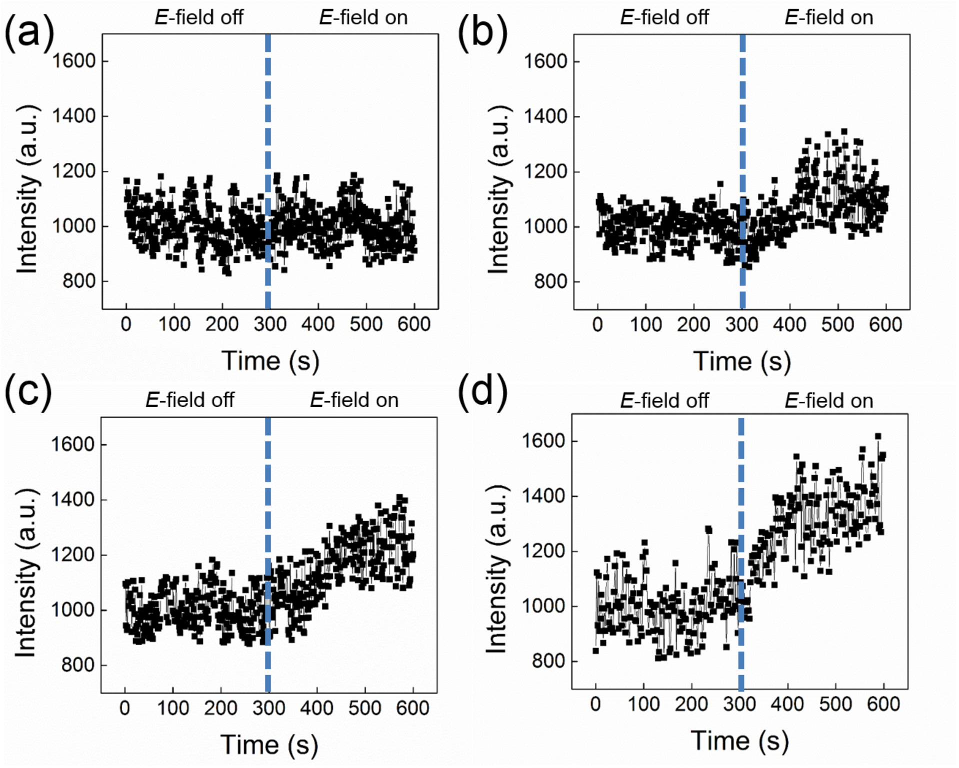

Figure 3.11. Time dependent Raman intensity at 595 cm^{-1} of Nile blue molecules (100 nM) recorded before and after applying an electric field at 200 kHz (a) 5 V, (b) 10 V, (c) 15 V. (d) 20 V.

As soon as the electric field was applied, the intensity of Raman signal rapidly increased and reached the saturation in ~100 sec at 20V (Fig 11d). Compared to the peak intensity without the electric field in the first 300 sec, the Raman peak intensity increased by ~35% in total due to the electric field. The result is well repeatable. Within different trials, the average increment of Raman intensity is 34.4 ± 3.1%. Moreover, we also systematically tuned the amplitude of the applied *E*-field at 200 kHz from 5 V to 20 V (Fig. 11). When we applied 5 V, the Raman signal did not change obviously; when we increased the applied voltage from 5 V to 10 V and 15 V, the Raman signal increased to 10.9% and

24.4%, respectively. Note that for the comparison purpose, we normalized the Raman intensity before the *E*-field is applied. To further confirm the effect of the electric field, we cycled the application of the AC *E*-field at 20 V, 200 kHz. It shows that the enhancement of Raman detection can be essentially restored when the electric field is turned on again. The enhancement values are 31.5% and 31.6% for the first and second cycle, respectively (Fig. 3.12). The enhancement is attributed to the attraction of the Nile blue molecules to the hot spots on the nanocapsules due to the induced electric fields in the narrow junctions of Ag NPs. Different electrokinetic mechanisms can play roles. First, we notice that AC electroosmosis (ACEO) flows could be induced by the electric field, where liquid flows circulate around the metallic nanoparticles due to the interactions of the electric field and the electrical double layers next to the surface of the nanoparticles [96]. Such flow can bring analyte molecules to the vicinity of the nanocapsules. When the molecules are close to the nanocapsules, the high intensity of the induced electric field at the junctions of Ag NPs can further attract them to the hotspots due to the DEP effect given by Eq. 3.3 and increase the SERS detection sensitivity. This understanding is supported by previous work [163] and quantitatively studied in the manipulation of solid-state molecules [164]. We noticed that the average Raman intensity before the *E*-field was applied in the second cycle decreased by ~5% compared to that in the first cycle, which could be attributed to the possible photo-bleaching of the dye molecules or unknown factors that need further investigation.

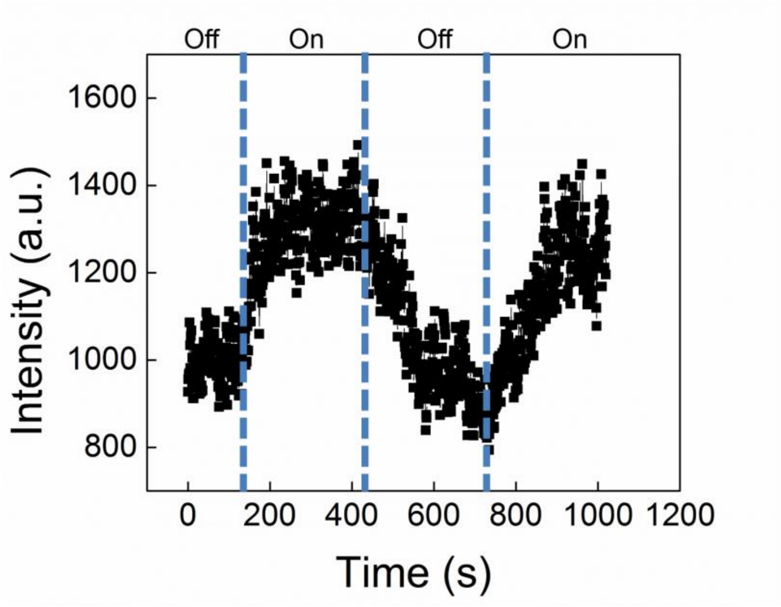

Figure 3.12. Time dependent Raman intensity of Nile blue molecules (100 nM) at 595 cm^{-1} recorded when the *E*-field is turned on and off alternatively at 20 V, 200 kHz.

In summary, we synthesized an innovative type of nanocapsule structures with large number of hotspots. By tuning the reaction conditions, we achieved optimized sizes of Ag NPs and junctions between the Ag NPs, which can detect biochemicals directly from suspensions with high reproducibility. After strategically assembling the as-grown SERS nanocapsules into ordered arrays on microelectrodes, we detected biochemicals such as Nile blue in a location deterministic manner. Moreover, assisted with electric field, we further enhanced the intensity of Raman signals by 34.4 ± 3.1% at optimal frequencies and voltages compared to those without electric fields. The enhancement mechanisms are discussed. As a result, the nanocapsules demonstrate dual functions in attraction of molecules and enhancement of their Raman signals owing to the uniquely designed structures. This work could inspire new types of microfluidic integrated SERS nanosensors.

3.3 DUAL ENHANCEMENT OF BIODETECTION FROM PLASMONIC PHOTONIC HYBRID DEVICES WITH INTEGRATED ELECTRIC FIELD MANIPULATION

Raman scattering, which was discovered in 1928 by Dr. C. V. Raman, has been utilized to unambiguously identify molecules based on their intrinsic vibrational “fingerprint” states. However, due to the relatively small Raman scattering cross-sections, the intensity of the Raman signal is usually $1/10^6$ of that of the Rayleigh scattering. The recent discovery of Surface enhanced Raman scattering (SERS) dramatically improves the Raman signal and rejuvenates this field[17-18]. Various types of SERS substrate have been developed, and mainly can be categorized to four different types: (1) roughened surface, e.g., rough Ag surface[17]; (2) nanoparticles with controlled aggregations that form nanogaps[40], e.g. dimers and trimers; (3) nanostructures with sharp tips[46]; and (4) designed core-shell nanostructures[37]. An enhancement factor (EF) as high as 10^{10} can be achieved from these specifically designed SERS substrates which can detect various single molecules[20]. The SERS technique has shown great potential in pre-stage disease detection[165], warfare agent detection[23, 152], environmental pollutant detection[25, 151], and biomolecule detection[21a, 21c, 150]. However, SERS substrates with such high EF usually suffer from reproducibility and uniformity issues. Moreover, SERS detection is still largely conducted in a passive manner, where molecules are randomly attached to the sensors, which substantially limits the detection efficiency. Therefore, a comprehensive enhancement mechanism that can provide a reproducible enhancement of Raman signals across the entire substrate and can actively focus molecules to hot spots is highly desirable for SERS detection. Recently, the photonic crystal (PC) based guided-mode resonance

(GMR) has been successfully demonstrated to couple with localized surface plasmon resonance (LSPR) from metallic nanoparticles. The coupling provides additional enhancement of the local electric field (*E*-field) which further boost Raman signal due to the E^4 dependence. However, in order to precisely integrate plasmonic nanoparticles at designated location on PC, the experimental procedure usually involves time consuming fabrication process such as electron-beam lithography (EBL). Xu[166] et al innovatively integrated plasmonic active SiO_2 nanotubes with Si_3N_4 gratings and successfully improved the EF factor by 8-10 times in addition to the existing SERS effect across the entire surface of the SiO_2 nanotubes. Although this method avoids the complex fabrication steps, it is still non-controllable, where the plasmonic active SiO_2 nanotubes are placed on the optical gratings

On the other hand, most reported SERS detections are conducted in a dry environment. Solutions containing analytes are dispersed on the SERS substrates and evaporate in the air. In this manner, the analytes in the solution are forced to deposit on the SERS substrate for detection. Since the entire evaporation process is uncontrollable, the area of the analyte solution wetting the SERS substrate can have large differences between different operations. Moreover, there is no mechanisms to position analyte molecules on specific locations, such as the hot spot on SERS substrates. The measurement results of SERS substrates strongly depend on individuals and research groups. It remains difficult to qualitatively compare results reported by different research groups. While, if one can detect analytes directly from a suspension medium with controlled concentrations, the problem of uncontrollable distribution of analyte molecules in SERS characterization can be largely reduced. Such an efforts also have important implications in microfluidics. However, when directly detect the molecules in a suspension using SERS, due to the inefficient diffusion based binding process, much less molecules can closely interact with hot spots compared to those in dried process on the same SERS substrate. As a result, the lowest detection limit can often be higher by a few orders of magnitudes compares to those obtained in a dry condition. Therefore, it is of great interest to investigate new mechanisms to detect analyte molecules directly from solutions with high sensitivity.

As introduced in Chapter 1, the effect of electrokinetics can be used to manipulate electrically charged or uncharged particles with sizes on the scale of micrometers to nanometers in suspension by applied electric fields. Recently, substantial interest has been focused on electrokinetics for applications in SERS detection. Various patterned substrates including Au nanoholes[158], microneedles electrode[159], nanopillars[160], and nanospheres[21d, 161] have been developed to preconcentrate analyte molecules to hotspots by electric fields for SERS detection. Nevertheless, most of the previous works either require complicate fabrication processes[159-161] or have little control of the sizes and junctions of the hot spot for reproducible detection when applying electric field[161]

In this dissertation, we report an integrated lab-on-a-chip system which for the first time offers two enhancement mechanisms that improve both sensitivity and efficiency in SERS detection directly from suspension. The device is made of bottom-up synthesized SERS nanocapsules (discussed in Chapter 2) and top-down electron-beam fabricated photonic crystals. The SERS-active nanocapsules are efficiently assembled on top of the photonic crystals and form ordered arrays by electric fields. The synergistic resonance of photonic crystal and plasmonic nanoparticles can effectively amplify Raman signals and enhance SERS detection. The applied electric field via integrated microelectrodes not only can be used to assemble nanocapsules into devices but also can efficiently attract analyte molecules to the nanocapsules to increase the concentration and interaction of molecules with Ag nanoparticles on the surface of nanocapsules. As a result, the device can improve the detection sensitivity and efficiency directly from suspension in a rational and designed manner. Experiments show that in addition to the SERS enhancement of 10^9- 10^{10} from the nanocapsules, the designed photonic crystal slab provides another 3-time enhancement. Also due to the isotropic structures, the plasmonic nanocapsules can be positioned in any direction with respect to the 2-D photonic crystal slab without impairing performances. Furthermore, with optimized AC frequencies and voltages, analyte molecules, including Nile blue, adenine, and melamine can be effectively concentrated on the surface of the nanocapsules, which further improves the enhancement by 19% to 45%. In total, the designed structures can robustly improve the detection sensitivity by another 4- 5 time on top of the existing SERS enhancement of 10^9 - 10^{10}. The device can also be readily integrated with microfluidics for on-chip molecule sensing by Raman spectroscopy.

The fabrication scheme of the PC slab with interdigital microelectrodes is illustrated in Fig 3.13. The fabrication begins with a fused glass substrate which is deposited with a thin layer of Si_3N_4 (thickness: 230 nm) as shown in Fig 3.13a. The two-dimensional (2-D) PC nanoholes are patterned by electron-beam lithography (EBL), followed by reactive ion beam (RIE) which creates ordered nanoholes in the Si_3N_4 (Fig 3.13b). Then, the obtained 2-D PC slab is carefully cleaned by piranha solution at 80 °C for 10 mins. This cleaning step is critical to ensure the surface is residue free and ready for the next photolithography step. Otherwise, the Au electrode cannot strongly bond to the substrate and can be peeled off when applied in the later SERS detection. Next, AZ5214 photoresist is spin coated on obtained PC slab, and patterned to the interdigital structure by photolithography. After developing the photoresist, a chromium adhesion layer with a thickness of 10 nm and a 150 nm Au layer are deposited on the substrate by electron-beam evaporation. The AZ5214 photoresist is finally removed by lift-off (Fig 3.13c) in Remover PG solution at 95 °C. The obtained PC slab with embedded interdigital microelectrodes is shown in Fig 3.13d and the zoom-in image of the obtained 2-D photonic crystal arrays is shown in Fig. 3.14.

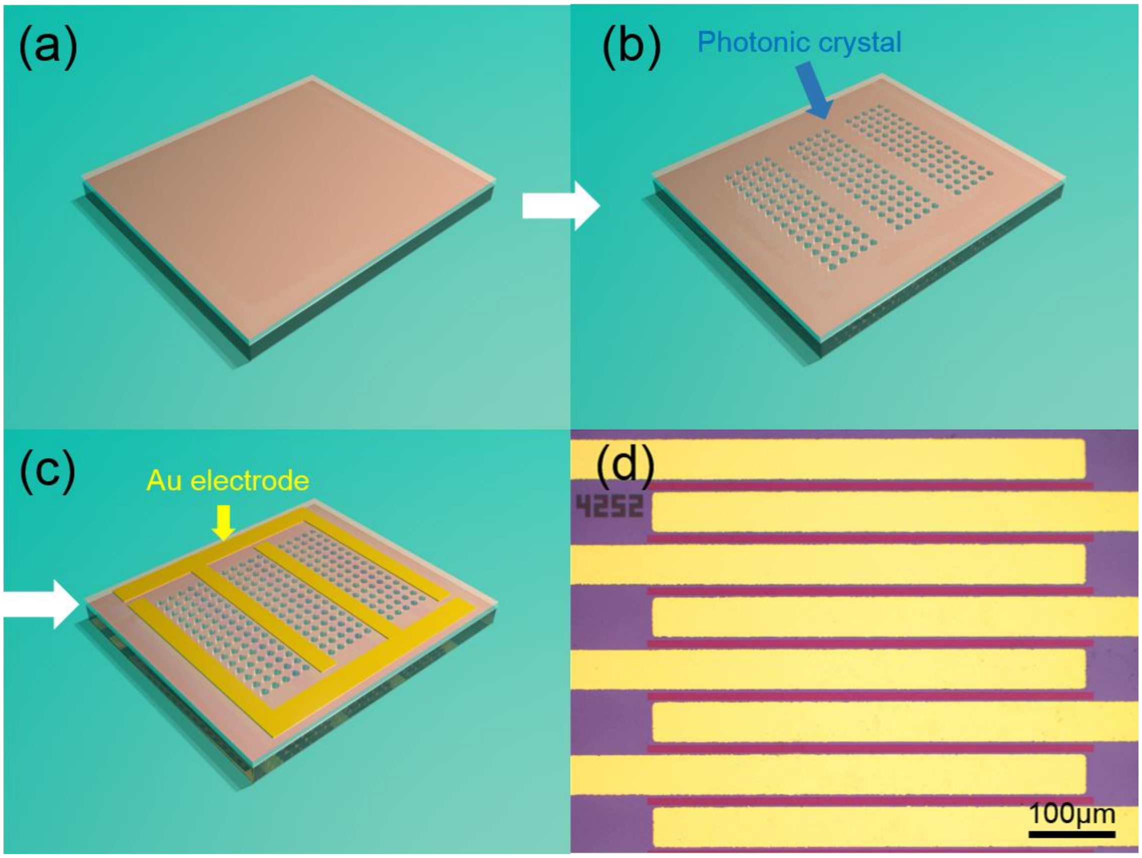

Figure 3.13 Fabrication scheme of the PC slab with embedded interdigital microelectrodes. (a) A fused glass is coated with a thin layer of Si_3N_4 (thickness: 230 nm). (b) 2-D PC slab is fabricated by EBL and RIE. (c) Au interdigital microelectrodes are patterned by the photolithography, followed by electron-beam evaporation. (d) Optical micrograph of the obtained PC slab with embedded interdigital electrodes.

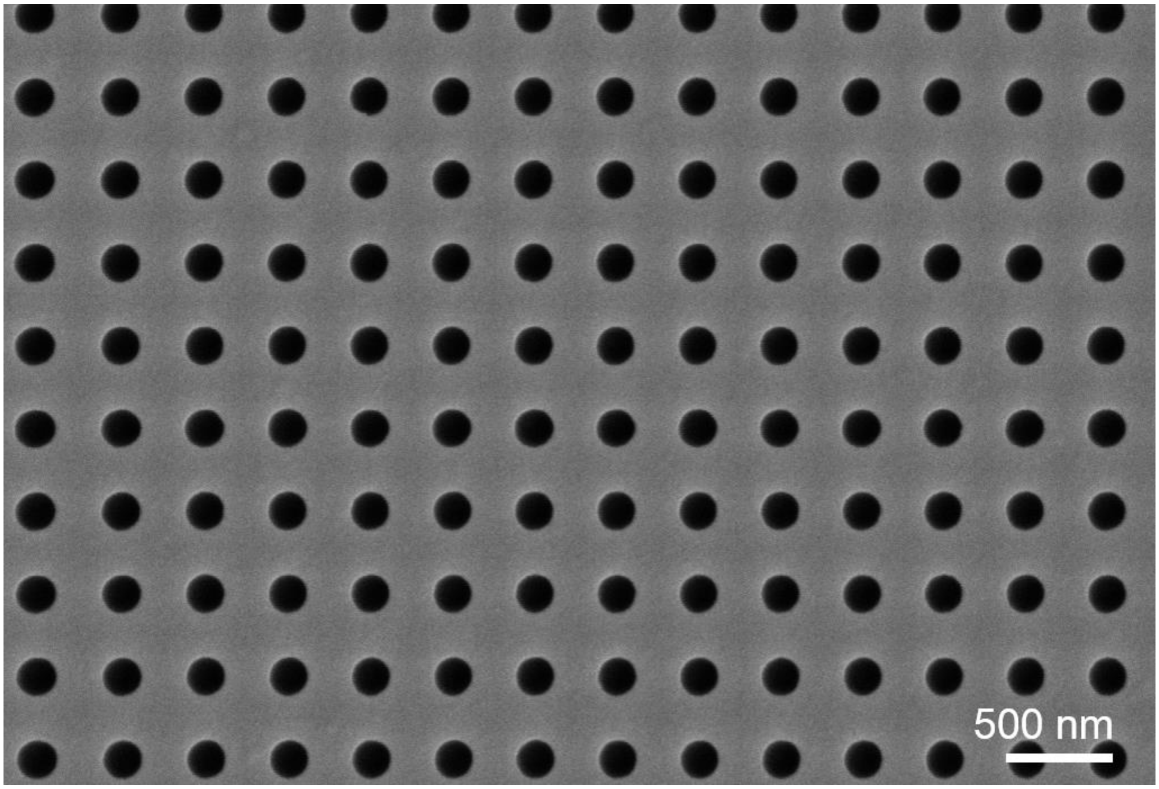

Figure 3.14 SEM image of 2-D photonic crystal with a period of 425 nm and a hole size of 213 nm.

The SERS active nanocapsules consist of a tri-layer structure with a gold nanowire in the core, a thin silica layer on the surface of the nanowire core, and high-density Ag nanoparticles (NPs) grown on the silica layer providing closely positioned hot spots. The inner gold nanowire core can be polarized and manipulated in the electric field based on the dielectrophoretic effect. The silica layer provides a substrate for the synthesis of Ag NP arrays which also effectively separates the Au nanowire core and the Ag NPs and eliminates the possible quenching effect between them. The Ag NPs in the outmost surface have optimized size, density, and uniformity and can effectively detect R6G molecules dried on the surface with single molecule sensitivity[127b, 128].

The fabrication of nanocapsules has been discussed in Chapter 2. In brief, the fabrication begins with the electrochemical deposition of Au nanowires in an anodic aluminum oxide (AAO) template with a conductive copper layer coated on the back. Au nanowires are electrochemical deposited into the AAO template from commercially available cynide based electrolyte (434 HS RTU, Technic Inc.). The diameter of the nanowires can be controlled by the pore size in the AAO template from tens of nanometers to 300 nm, and the length of the Au nanowires is adjusted based on the total amount of electric charge passing through the circuit. After dissolving the AAO template in the 2 M NaOH solution, the nanowires are resuspended and sonicated in ethanol and deionized (D. I.) water alternatively twice before redispersed in D. I. water. Billions of nanowires can be fabricated at a time with length of 9.1 μm and diameter of 300 nm as shown in Fig. 3. 15a. Next, a 180 nm thick SiO_2 layer is coated on the surface of Au nanowires via hydrolysis of tetraethyl orthosilicate (TEOS, 0.8 ml, Alfa Aesar, 99.999+%) in ammonia (0.2 ml, Fisher Scientific, Certified A.C.S. Plus), ethanol (3 ml, Pharmco-aaper, ACS/USP grade), and deionized water (1.8 ml) mixture solution under sonication for 1 hour. Finally, Ag NP arrays are synthesized on the surface of silica by mixing Au@SiO_2 nanowires with freshly prepared 500 µl, 0.06 M silver nitrate ($AgNO_3$, ACROS Organics, 99.85%), and 250 µl, 0.12 M ammonia, stirring for 1 hour before adding polyvinylpyrrolidone (PVP, 10 ml of 2.5×10^{-5} M in ethanol, Sigma-Aldrich, M_w=40000) to promote the growth of Ag NPs at 70 ^{o}C. After 7-hour reaction, dense Ag NPs were obtained on the entire surface of the nanocapsules as shown in Fig. 3.15b. The size of Ag NPs and junctions here are 26 ± 5 nm and 1.8 ± 0.4 nm, respectively.

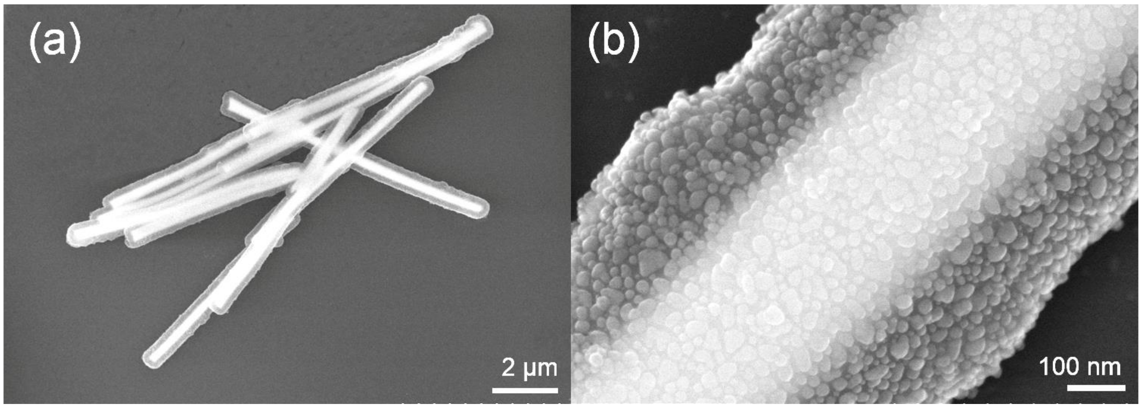

Figure 3.15 (a) SEM images of nanocapsules, (b) high density Ag nanoparticle arrays grown on the surface of nanocapsules.

In order to study and optimize the coupling between the PC slab and the nanocapsules, we designed a 2-D PC slab with periodic spherical holes on a 230 nm thick Si_3N_4 layer (the refractive index, n=2.4 at 633nm) based on a fused glass substrate (the refractive index, n=1.45 at 633nm). The effective refractive index of the nitride layer is greater than the index of the fused glass substrate, which is important for GMR. Using rigorous coupled wave analysis (RCWA), we found that as we increase the periodicity from 420nm to 430nm, a maximum reflectivity is achieved at a period of 425 nm with a hole size of 213 nm (Fig. 3.16b). The reflectivity spectrum of this design also indicates that the GMR is at 633 nm for polarized incidence that is normal to the grating surface as show in the Fig. 3.16c. Then, experiments were conducted in order to validate our simulation result. Various PC slabs with periodicities of 420 nm, 425 nm, 427 nm, 430 nm and fixed hole size of 213 nm were fabricated as described previously. The nanocapsules which were suspended in the ethanol solution were first dispersed on the PC slab within a Polydimethylsiloxane (PDMS) well. After the evaporation of the ethanol solution, 20 µL of 100 nM Nile blue solution was dispersed into the well and coved with a cover glass. After 10 mins incubation, the PC slab with the nanocapsules on it was flipped over and fixed on a customized Raman microscope. Due to the electrostatic force between the nanocapsules and the PC slab, the nanocapsules attached to PC slab firmly. The cover glass effective sealed the PDMS well, and thus prevented the leaking of Nile blue solution from the well. A 633 nm laser was used to excite molecules on the nanocapsules via a 20X objective lens. The resulting signals were collected from the same objective, filtered by a 633 nm edge filter, and analyzed by a high sensitive spectrometer. In order to compare the enhancement factor on different 2-D PC slabs, the SERS signals from nanocapsules on the GMR grating and from nanocapsules on a flat Si_3N_4 substrate were compared. As shown in Fig 3.16a, the 2-D PC slab with a periodicity of 425 nm produced the highest enhancement of ~300%. The experimental result excellently agrees with the numerical simulation.

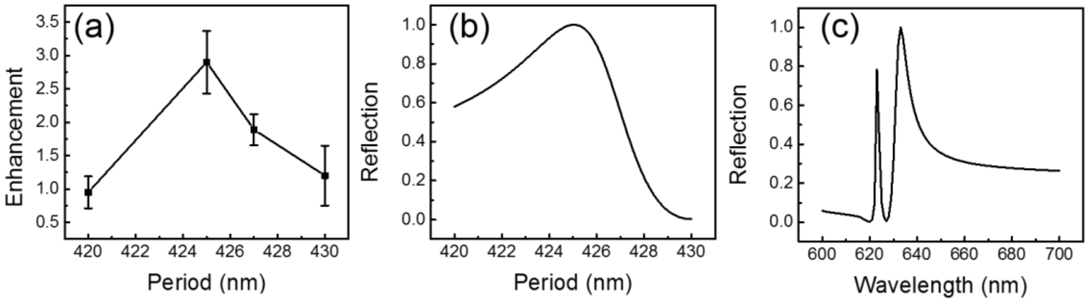

Figure 3.16 Both (a) Experimental result and (b) simulation result show that the 2-D PC slab with a periodicity of 425 nm generates the highest enhancement factor for an excitation laser at 633 nm. (c) Simulation shows that the GMR peak is at 633 nm.

Based on our previous work[167], we further improved the enhancement by concentrating the analyte molecules via electrokinetic effect. Before we integrated the same approach on our 2-D PC slab with embedded Au interdigital microelectrodes, we first tested the optimized attraction frequency for various analyte molecules on an indium tin oxide (ITO) interdigital microelectrode without photonic crystal structures. Three different types of molecules were tested, including Nile blue which is often used as SERS probe molecules, adenine which is a nucleobase, and melamine which can be a contaminant ingredient in milk. The experimental details are as follows: a 14 µL nanocapsule suspension was first dispersed in a PDMS well on an ITO interdigital microelectrode with a gap size around 20 µm. Upon the application of the electric field at 700 kHz and 20 V, the nanocapsules were swiftly attracted to the edges of the microelectrodes and aligned along the direction of the electric fields.

The migration and assembling of nanocapsules can be attributed to dielectrophoretic (DEP) force resulting from the interaction between the AC electric field and polarized nanocapsules, given by [137]

$$F = p \cdot \nabla E, \tag{3.4}$$

where the polarization of the nanocapsules (p) is proportional to the applied electric fields, DEP force also depends on the materials and geometry of the nanocapsules. The transport and orientation of the nanocapsules are in the directions of the electric-field gradient and electric field, respectively [138].

After assembling arrays of nanocapsules, we turned off the AC voltage and carefully dispersed 14 μl adenine solution with a concentration as low as 10 μM into the PDMS well and sealed with a cover glass. Again, the nanocapsules attached to the ITO glass even without the electric field due to the electrostatic interactions between nanocapsule and the substrate. Then, the time dependent Raman spectra of adenine were recorded from the nanocapsule for 480 s with an integration time of 2 s. The peak height at 736 cm^{-1} was used in the analysis since it is one of the strongest peaks and well separated from others. For comparison purpose, the average peak heights before applying E-fields were normalized to 1000. AC electric fields with frequencies ranging from 70 kHz to 400 kHz were studied as shown in Fig. 3.17. The strongest attraction was achieved at 70 kHz [Fig. 3.17a]. Upon the application of the electric field, the intensity of Raman signal rapidly increases and becomes saturated in ~200 s at 20 V (Fig 3.17). Compared to the average intensity without electric field in the first 3 mins, the Raman peak intensity increased by

~20% in total due to the electric field. The enhancement is due to the attraction of the adenine molecules to the hot spots on the nanocapsules by the electrokinetic effect.

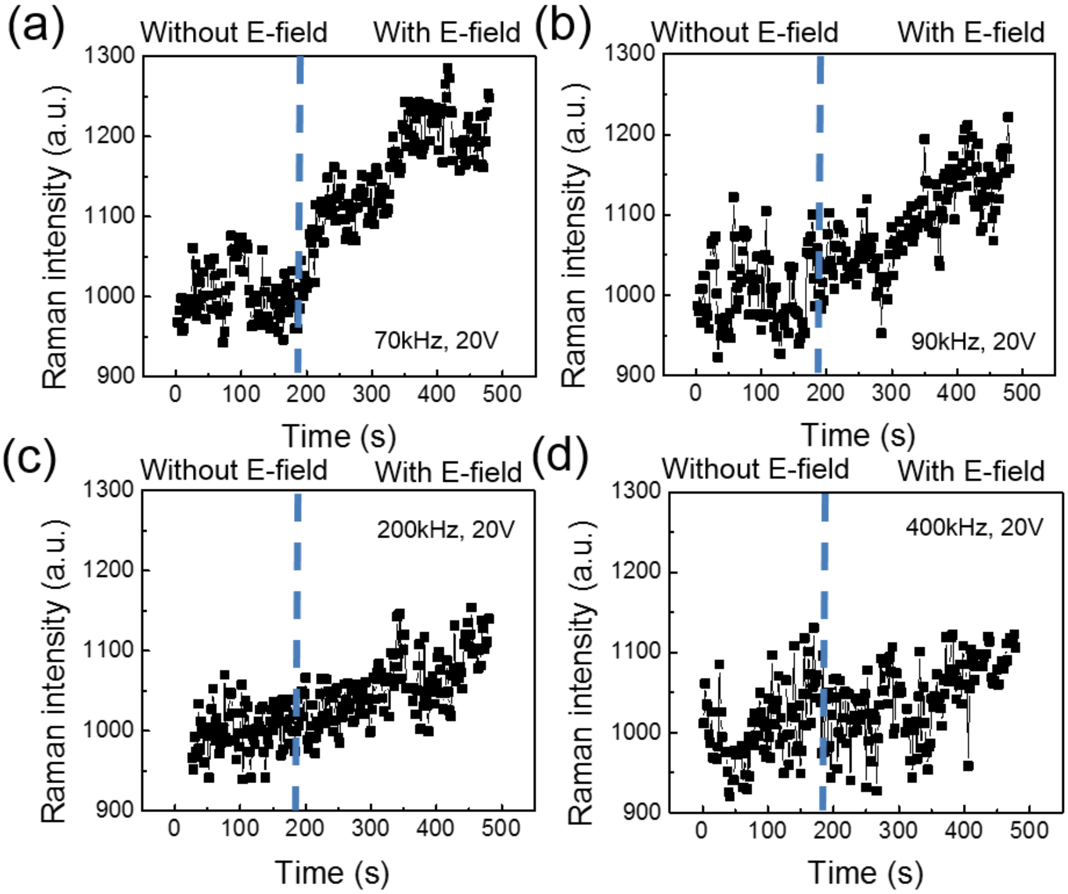

Figure 3.17 Time dependent Raman intensity at 736 cm^{-1} of adenine molecules (10 µM) recorded before and after applying an electric field at 20 V and (a) 70 kHz, (b) 90 kHz, (c) 200 kHz and (d) 400 kHz. The average Raman intensities are normalized to 1000 before applying the electric field.

The alternating current electroosmosis (ACEO) and DEP effects can be attributed to the observed molecule concentration. As discussed in Chapter 1, ACEO effect can generate circulating flows around the nanocapsules due to the interaction of the electric double layer and the electric field along the tangential direction[96]. Such vortex flow can compel analyte molecules to the vicinity of the nanocapsules. When the molecules approach the nanocapsules, the high intensity induced electric field at the junctions of Ag NPs can further attract them to the hotspots due to the DEP effect and increase the SERS signal. This mechanism has been proposed and confirmed in our previous study in the manipulation of molecular sized quantum dots[164]. Experimentally, we found that for different analyte molecules, the optimized attraction frequency is different. For instance, the optimized attraction frequency for Nile blue and melamine is at 200 kHz. The different optimized frequency can be due to the intrinsic properties of the analyte molecules including the conductivity and the permittivity which could influence the DEP forces in focusing the molecules.

Finally, we carried out the molecule attraction on a 2-D PC slab with embedded Au interdigital microelectrodes. The experimental procedure is similar to that of SERS detection on the non-PC ITO interdigital microelectrodes. On the PC, we designed Au interdigital microelectrodes with a gap size of 15 µm. The SEM images in Fig. 3.18 clearly demonstrate the assembled ordered nanocapsule arrays, the slightly tilted nanocapsules are due to the surface tension from the evaporated solution. In the zoom-in SEM images, the 2-D PC structures can be clearly seen supporting the nanocapsules. As demonstrated in Fig. 3.19, upon the application of the electric field, analyte molecules were attracted to the nanocapsules and the SERS signal increased accordingly. For 100 nM Nile blue, 10 µM adenine molecules and 1 mM melamine molecules, after applying the optimized attraction frequency at 200 kHz, 70 kHz, and 200 kHz, the SERS signal increased by 19%; 19% and 45% respectively. As a result, the total enhancement factor generated by the combined effects of GMR and electric concentration is around 4-5 times.

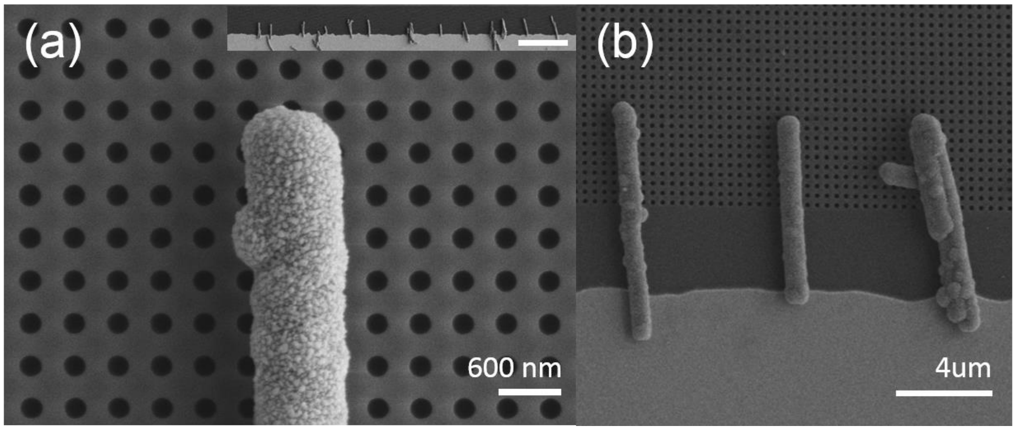

Figure 3.18 (a) Zoom-in SEM image of assembled nanocapsule on the 2-D PC substrate embedded with Au interdigital microelectrodes. (Inset: SEM image of assembled nanocapsule arrays on the 2-D PC substrate embedded with Au interdigital microelectrodes, the scale bar is 30 µm) (b) SEM image of assembled nanocapsule arrays.

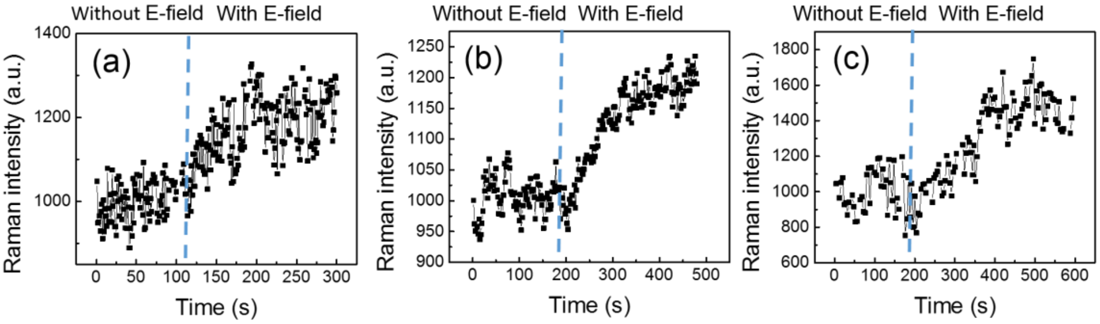

Figure 3.19 Time dependent Raman intensity of (a) Nile blue molecules (100 nM), (b) adenine molecules (10 µM), and (c) melamine molecules (1 mM) recorded before and after applying an electric field at 20 V and 200 kHz; 70 kHz and 200 kHz, respectively. The average Raman intensities are normalized to 1000 before the application of the electric field.

In summary, we demonstrate an innovative type of SERS-photonic-crystal-slab device by integrating plasmonic nanocapsules into 2-D photonic crystal substrates via controlled manipulation by electric fields. A total enhancement factor of 4-5 times in addition to the 10^9-10^{10} SERS effects from the plasmonic nanocapsules is achieved in suspensions. Such new enhancement is a compound of two factors: in addition to the enhancement by plasmonic-photonic resonances, which provides ~3 time improvement, by applying electric field, various biological and environmental interesting molecules, including Nile blue, adenine, and melamine, can be efficiently focused on the surface of the nanocapsules that further improved the enhancement by 19% to 45%. This work could inspire the next generation microfluidic-based Raman sensing devices.

Chapter 4: Conclusion

In summary, I rationally designed and synthesized various types of nanostructures, including ZnO, Si, and Au nanowires, ZnO nanosuperstructures, and hybrid nanocapsules. Such materials have unique optical/plasmonic properties and could be used in various applications, particularly in biochemical sensing. Two types of optical nanobiosensors have been designed, fabricated, characterized, and investigated. They are fluorescence-based QD-on-nanowire assemblies and SERS-photonic-crystal hybrid nanosensors. The QD-on-nanowire florescent nanosensors operated uniquely by focusing analyte molecules to the assembled QDs on tips of nanowires before detection via specific biochemical conjugation. Molecules, such as biotin, can be revealed unambiguously in a location deterministic manner with substantially enhanced sensitivity. In the development of SERS-photonic-crystal hybrid nanosensors, two enhancement mechanisms, including GMR and electrokinetic effect, were studied and applied in improving the sensitivity and efficiency of molecule detection, respectively. Such a hybrid device has been proposed and studied for the first time, which can readily improve the detection sensitivity by a robust 4-5 times in addition to the 10^9-10^{10} SERS enhancement. This dissertation work, exploring innovative materials design, synthesis, and manipulation, has made an important forward step in the next-generation biochemical detection platform.

Appendix A: List of Journal Publications

1 **Chao Liu**$^{\#}$, Zheng Wang$^{\#}$, Ray T. Chen, and D. L. Fan, "Dual Enhancement of Biodetection from Plasmonic Photonic Hybrid Devices with Integrated Electric Field Manipulation", in preparation.

2 Zheng Wang$^{\#}$, **Chao Liu**$^{\#}$, Erwen Li, Alan X. Wang and Ray T. Chen, and D. L. Fan, "Universal Enhancement of Raman Scattering Sensing by Plasmonic Photonic Hybrid structure", in preparation

3 **Chao Liu**, Xiaobin Xu, and D. L. Fan, "Rational Synthesis of Three Dimensional Nanosuperstructures for Applications in Energy Storage and Conversion Devices", ***IEEE-Transactions on Device and Materials Reliability***, in press (2016) DOI: 10.1109/TDMR.2015.2514238

4 Zheng Wang$^{\#}$, **Chao Liu**$^{\#}$, Swapnajit Chakravarty, D. L. Fan, Alan X. Wang and Ray T. Chen, "Universal Enhancement of Raman Scattering Sensing by Plasmonic Nanotubes Coupled with Photonic Crystal Slab", ***in CLEO: 2015, OSA Technical Digest*** (online) (Optical Society of America, 2015), paper SM3O.3.

5 Longjun Li, **Chao Liu**, Guang He, D. L. Fan and Arumugam Manthiram, "Hierarchical pore-in-pore and wire-in-wire catalysts for rechargeable Zn- and Li-air batteries with ultra-long cycle life and high cell efficiency", ***Energy & Environmental Science***, 8, (2015), 3274-3282.

6 **Chao Liu**, Xiaobin Xu and D. L. Fan, “Electric-Field Enhanced Molecule Detection in Suspension on Assembled Plasmonic Arrays by Raman Spectroscopy”, ***ASME-Journal of Nanotechnology in Engineering and Medicine***, 5, (2015), 040906

7 Xiaobin Xu, Kwanoh. Kim, **Chao Liu** and D. L. Fan, “Ultrasensitive Robotized Plasmonic Nanosensors for Biochemical Detection with Raman Spectroscopy”, ***Sensors***, 15, (2015), 10422-10451

8 **Chao Liu**, Kwanoh Kim and D. L. Fan, “Location Deterministic Biosensing from Quantum-Dot-Nanowire Assemblies”, ***Applied Physics Letters***, 105, (2014), 083123.

9 Jing Ning[#], Xiaobin Xu[#], **Chao Liu** and D. L. Fan, “Three-Dimensional Multilevel Porous Thin Graphite Nanosuperstructures for $Ni(OH)_2$-based Energy Storage Devices”, ***Journal of Materials Chemistry A***, 2, (2014), 15768-15773. (**Featured on the inside front cover**)

10 Xiaobin Xu[#], **Chao Liu[#]**, Kwanoh Kim, and D. L. Fan, “Electric-Driven Rotation of Silicon Nanowires and Silicon Nanowire Motors”, ***Advanced Functional Materials***, 24, (2014), 4843–4850.

11 **Chao Liu**, Xiaobin Xu, Alexander John Edward Rettie, Charles B. Mullins and D. L. Fan, “One-step waferscale synthesis of 3-D ZnO Nanosuperstructures by Designed Catalysts for Substantial Improvement of Solar Water Oxidation Efficiency”, ***Journal of Materials Chemistry A***,1, (2013), 8111-8117. (**Featured on the front cover**)

[#] contributed equally**.**

Appendix B: List of Conference Presentations

1. **Chao Liu**, Kwanoh Kim, D. L. Fan "Location Deterministic Biosensingfrom Quantum-Dot-Nanowire Assemblies" ***NanoTechnology for Defense Conference,*** industry, CA (2015)

2. Jing Ning, Xiaobin. Xu, **Chao Liu** and D. L. Fan "Free Standing Three-Dimensional Porous Graphite/Ni(OH)$_2$ Foam for Supercapacitors" ***2014 MRS Spring Meeting & Exhibit,*** San Francisco, CA

3. Jing Ning, Xiaobin Xu, **Chao Liu** and D. L. Fan, "Three Dimensional Graphene/Graphite Structures Templated on Engineered Highly Porous Ni/Cu Foams" ***NanoTechnology for Defense Conference***, Tucson, AZ (2013)

4. **Chao Liu**, Xiaobin Xu, Alexander John Edward Rettie, Charles Buddie Mullins and D. L. Fan, "One-step waferscale synthesis of 3-D ZnO nanosuperstructures by designed catalysts for substantial improvement of solar water oxidation efficiency", ***2013 Nanotechnology for defense conference***

5. **Chao Liu**, Xiaobin Xu, Alexander John Edward Rettie, Charles Buddie Mullins and D. L. Fan, "Waferscale synthesis of 3-D ZnO nanosuperstructures in a single step for 150% enhancement of solar water splitting efficiency", ***2013 Defense Energy Summit, Poster presentation***

6. **Chao Liu**, Pengfei Zhang, Kwanoh Kim, James H. Werner and D. L. Fan, "Coupling and Fluorescent Enhancement of Semiconductor Nanoemitters on the Tips of Plasmonic Nanoantennas", ***2013 MRS Fall Meeting & Exhibit,*** Boston, MA
7. **Chao Liu**, Xiaobin Xu, Alexander John Rettie, Charles Buddie Mullins and D. L. Fan, "Rational one–step synthesis of three-dimensional ZnO nanosuperstructures by engineered catalysts for 150% improvement of solar water splitting efficiency", ***2012 MRS Fall Meeting & Exhibit,*** Boston, MA.

Reference

1. Michalet, X.; Pinaud, F. F.; Bentolila, L. A.; Tsay, J. M.; Doose, S.; Li, J. J.; Sundaresan, G.; Wu, A. M.; Gambhir, S. S.; Weiss, S., Quantum dots for live cells, in vivo imaging, and diagnostics. *Science* **2005,** *307* (5709), 538-544.

2. (a) Wilson, R.; Cossins, A. R.; Spiller, D. G., Encoded microcarriers for high-throughput multiplexed detection. *Angew. Chem. Int. Ed.* **2006,** *45* (37), 6104-6117; (b) Klostranec, J. M.; Xiang, Q.; Farcas, G. A.; Lee, J. A.; Rhee, A.; Lafferty, E. I.; Perrault, S. D.; Kain, K. C.; Chan, W. C. W., Convergence of quantum dot barcodes with microfluidics and signal processing for multiplexed high-throughput infectious disease diagnostics. *Nano Lett* **2007,** *7* (9), 2812-2818.

3. (a) Pellegrino, T.; Parak, W. J.; Boudreau, R.; Le Gros, M. A.; Gerion, D.; Alivisatos, A. P.; Larabell, C. A., Quantum dot-based cell motility assay. *Differentiation* **2003,** *71* (9-10), 542-548; (b) Gao, J. H.; Chen, X. Y.; Cheng, Z., Near-Infrared Quantum Dots as Optical Probes for Tumor Imaging. *Curr Top Med Chem* **2010,** *10* (12), 1147-1157.

4. (a) Medintz, I. L.; Clapp, A. R.; Brunel, F. M.; Tiefenbrunn, T.; Uyeda, H. T.; Chang, E. L.; Deschamps, J. R.; Dawson, P. E.; Mattoussi, H., Proteolytic activity monitored by fluorescence resonance energy transfer through quantum-dot-peptide conjugates. *Nat Mater* **2006,** *5* (7), 581-589; (b) Algar, W. R.; Ancona, M. G.; Malanoski, A. P.; Susumu, K.; Medintz, I. L., Assembly of a Concentric Forster Resonance Energy Transfer Relay on a Quantum Dot Scaffold: Characterization and Application to Multiplexed Protease Sensing. *ACS Nano* **2012,** *6* (12), 11044-11058.

5. (a) Biju, V.; Muraleedharan, D.; Nakayama, K.; Shinohara, Y.; Itoh, T.; Baba, Y.; Ishikawa, M., Quantum dot-insect neuropeptide conjugates for fluorescence imaging, transfection, and nucleus targeting of living cells. *Langmuir* **2007,** *23* (20), 10254-10261; (b) Zhou, M.; Nakatani, E.; Gronenberg, L. S.; Tokimoto, T.; Wirth, M. J.; Hruby, V. J.; Roberts, A.; Lynch, R. M.; Ghosh, I., Peptide-labeled quantum dots for imaging GPCRs in whole cells and as single molecules. *Bioconjugate Chem* **2007,** *18* (2), 323-332.

6. (a) Kim, Y. G.; Moon, S.; Kuritzkes, D. R.; Demirci, U., Quantum dot-based HIV capture and imaging in a microfluidic channel. *Biosens. Bioelectron* **2009,** *25* (1), 253-258; (b) Deng, Z. T.; Zhang, Y.; Yue, J. C.; Tang, F. Q.; Wei, Q., Green and orange CdTe quantum dots as effective pH-sensitive fluorescent probes for dual simultaneous and independent detection of viruses. *J Phys Chem B* **2007,** *111* (41), 12024-12031.

7. (a) Karwa, A.; Papazoglou, E.; Pourrezaei, K.; Tyagi, S.; Murthy, S., Imaging biomarkers of inflammation in situ with functionalized quantum dots in the dextran sodium sulfate (DSS) model of mouse colitis. *Inflamm Res* **2007,** *56* (12), 502-510; (b) Zajac, A.; Song, D. S.; Qian, W.; Zhukov, T., Protein microarrays and quantum dot probes for early cancer detection. *Colloid Surface B* **2007,** *58* (2), 309-314.

8. Medintz, I. L.; Stewart, M. H.; Trammell, S. A.; Susumu, K.; Delehanty, J. B.; Mei, B. C.; Melinger, J. S.; Blanco-Canosa, J. B.; Dawson, P. E.; Mattoussi, H., Quantum-dot/dopamine bioconjugates function as redox coupled assemblies for in vitro and intracellular pH sensing. *Nat Mater* **2010,** *9* (8), 676-84.

9. Stanisavljevic, M.; Krizkova, S.; Vaculovicova, M.; Kizek, R.; Adam, V., Quantum dots-fluorescence resonance energy transfer-based nanosensors and their application. *Biosens. Bioelectron* **2015,** *74*, 562-574.

10. Willard, D. M.; Carillo, L. L.; Jung, J.; Van Orden, A., CdSe-ZnS quantum dots as resonance energy transfer donors in a model protein-protein binding assay. *Nano Lett* **2001,** *1* (9), 469-474.

11. Snee, P. T.; Somers, R. C.; Nair, G.; Zimmer, J. P.; Bawendi, M. G.; Nocera, D. G., A ratiometric CdSe/ZnS nanocrystal pH sensor. *J. Am. Chem. Soc* **2006,** *128* (41), 13320-13321.

12. (a) Li, J.; Mei, F.; Li, W. Y.; He, X. W.; Zhang, Y. K., Study on the fluorescence resonance energy transfer between CdTe QDs and butyl-rhodamine B in the presence of CTMAB and its application on the detection of Hg(II). *Spectrochim Acta A* **2008,** *70* (4), 811-817; (b) Liu, B. Y.; Zeng, F.; Wu, G. F.; Wu, S. Z., Nanoparticles as scaffolds for FRET-based ratiometric detection of mercury ions in water with QDs as donors. *Analyst* **2012,** *137* (16), 3717-3724.

13. Dennis, A. M.; Rhee, W. J.; Sotto, D.; Dublin, S. N.; Bao, G., Quantum Dot-Fluorescent Protein FRET Probes for Sensing Intracellular pH. *ACS Nano* **2012,** *6* (4), 2917-2924.

14. Xia, Z. Y.; Xing, Y.; So, M. K.; Koh, A. L.; Sinclair, R.; Rao, J. H., Multiplex Detection of Protease Activity with Quantum Dot Nanosensors Prepared by Intein-Mediated Specific Bioconjugation. *Anal Chem* **2008,** *80* (22), 8649-8655.

15. Pfleger, K. D. G.; Eidne, K. A., Illuminating insights into protein-protein interactions using bioluminescence resonance energy transfer (BRET). *Nat Methods* **2006,** *3* (3), 165-174.

16. Xie, Q.; Soutto, M.; Xu, X.; Zhang, Y.; Johnson, C. H., Bioluminescence resonance energy transfer (BRET) imaging in plant seedlings and mammalian cells. *Molecular Imaging: Methods and Protocols* **2011**, 3-28.

17. Fleischmann, M.; Hendra, P. J.; Mcquilla.Aj, Raman-Spectra of Pyridine Adsorbed at a Silver Electrode. *Chem Phys Lett* **1974,** *26* (2), 163-166.

18. (a) Jeanmaire, D. L.; Van Duyne, R. P., Surface Raman spectroelectrochemistry: Part I. Heterocyclic, aromatic, and aliphatic amines adsorbed on the anodized silver electrode. *Journal of Electroanalytical Chemistry and Interfacial Electrochemistry* **1977,** *84* (1), 1-20; (b) Albrecht, M. G.; Creighton, J. A., Anomalously intense Raman spectra of pyridine at a silver electrode. *J. Am. Chem. Soc* **1977,** *99* (15), 5215-5217.

19. (a) Sharma, B.; Frontiera, R. R.; Henry, A. I.; Ringe, E.; Van Duyne, R. P., SERS: Materials, applications, and the future. *Mater Today* **2012,** *15* (1-2), 16-25; (b) Fan, M. K.; Andrade, G. F. S.; Brolo, A. G., A review on the fabrication of substrates for surface

enhanced Raman spectroscopy and their applications in analytical chemistry. *Anal Chim Acta* **2011,** *693* (1-2), 7-25.

20. (a) Nie, S. M.; Emery, S. R., Probing single molecules and single nanoparticles by surface-enhanced Raman scattering. *Science* **1997,** *275* (5303), 1102-1106; (b) Kneipp, K.; Wang, Y.; Kneipp, H.; Perelman, L. T.; Itzkan, I.; Dasari, R.; Feld, M. S., Single molecule detection using surface-enhanced Raman scattering (SERS). *Phys Rev Lett* **1997,** *78* (9), 1667-1670.

21. (a) Kang, T.; Yoo, S. M.; Yoon, I.; Lee, S. Y.; Kim, B., Patterned Multiplex Pathogen DNA Detection by Au Particle-on-Wire SERS Sensor. *Nano Lett* **2010,** *10* (4), 1189-1193; (b) Barhoumi, A.; Halas, N. J., Label-free detection of DNA hybridization using surface enhanced Raman spectroscopy. *J Am Chem Soc* **2010,** *132* (37), 12792-3; (c) Bell, S. E. J.; Sirimuthu, N. M. S., Surface-enhanced Raman spectroscopy (SERS) for sub-micromolar detection of DNA/RNA mononucleotides. *J. Am. Chem. Soc* **2006,** *128* (49), 15580-15581; (d) Cho, H. S.; Lee, B.; Liu, G. L.; Agarwal, A.; Lee, L. P., Label-free and highly sensitive biomolecular detection using SERS and electrokinetic preconcentration. *Lab Chip* **2009,** *9* (23), 3360-3363.

22. Zhang, X.; Young, M. A.; Lyandres, O.; Van Duyne, R. P., Rapid Detection of an Anthrax Biomarker by Surface-Enhanced Raman Spectroscopy. *J. Am. Chem. Soc* **2005,** *127* (12), 4484-4489.

23. Stuart, D. A.; Biggs, K. B.; Van Duyne, R. P., Surface-enhanced Raman spectroscopy of half-mustard agent. *Analyst* **2006,** *131* (4), 568-572.

24. Shafer-Peltier, K. E.; Haynes, C. L.; Glucksberg, M. R.; Van Duyne, R. P., Toward a glucose biosensor based on surface-enhanced Raman scattering. *J. Am. Chem. Soc* **2003,** *125* (2), 588-593.

25. Bhandari, D.; Walworth, M. J.; Sepaniak, M. J., Dual Function Surface-Enhanced Raman Active Extractor for the Detection of Environmental Contaminants. *Appl. Spectrosc.* **2009,** *63* (5), 571-578.

26. Kim, H.; Kosuda, K. M.; Van Duyne, R. P.; Stair, P. C., Resonance Raman and surface- and tip-enhanced Raman spectroscopy methods to study solid catalysts and heterogeneous catalytic reactions. *Chem Soc Rev* **2010,** *39* (12), 4820-44.

27. Chou, A.; Jaatinen, E.; Buividas, R.; Seniutinas, G.; Juodkazis, S.; Izake, E. L.; Fredericks, P. M., SERS substrate for detection of explosives. *Nanoscale* **2012,** *4* (23), 7419.

28. Le Ru, E. C.; Etchegoin, P. G., *Principles of Surface-Enhanced Raman Spectroscopy: And Related Plasmonic Effects*. Elsevier Science: Amsterdam, The Netherlands, 2008.

29. Stiles, P. L.; Dieringer, J. A.; Shah, N. C.; Van Duyne, R. P., Surface-Enhanced Raman Spectroscopy. *Annual Review of Analytical Chemistry* **2008,** *1* (1), 601-626.

30. Le Ru, E. C.; Blackie, E.; Meyer, M.; Etchegoin, P. G., Surface enhanced Raman scattering enhancement factors: a comprehensive study. *J Phys Chem C* **2007,** *111* (37), 13794-13803.

31. McFarland, A. D.; Young, M. A.; Dieringer, J. A.; Van Duyne, R. P., Wavelength-scanned surface-enhanced Raman excitation spectroscopy. *J Phys Chem B* **2005,** *109* (22), 11279-11285.

32. Camden, J. P.; Dieringer, J. A.; Zhao, J.; Van Duyne, R. P., Controlled Plasmonic Nanostructures for Surface-Enhanced Spectroscopy and Sensing. *Accounts Chem Res* **2008,** *41* (12), 1653-1661.

33. Campion, A.; Kambhampati, P., Surface-enhanced Raman scattering. *Chem Soc Rev* **1998,** *27* (4), 241-250.

34. Lombardi, J. R.; Birke, R. L., A Unified View of Surface-Enhanced Raman Scattering. *Accounts Chem Res* **2009,** *42* (6), 734-742.

35. Valley, N.; Greeneltch, N.; Van Duyne, R. P.; Schatz, G. C., A Look at the Origin and Magnitude of the Chemical Contribution to the Enhancement Mechanism of Surface-Enhanced Raman Spectroscopy (SERS): Theory and Experiment. *J Phys Chem Lett* **2013,** *4* (16), 2599-2604.

36. Banholzer, M. J.; Millstone, J. E.; Qin, L. D.; Mirkin, C. A., Rationally designed nanostructures for surface-enhanced Raman spectroscopy. *Chem Soc Rev* **2008,** *37* (5), 885-897.

37. (a) Zhu, Y. F.; Shi, J. L.; Shen, W. H.; Dong, X. P.; Feng, J. W.; Ruan, M. L.; Li, Y. S., Stimuli-responsive controlled drug release from a hollow mesoporous silica sphere/polyelectrolyte multilayer core-shell structure. *Angew. Chem. Int. Ed.* **2005,** *44* (32),

5083-5087; (b) Prokes, S. M.; Glembocki, O. J.; Rendell, R. W.; Ancona, M. G., Enhanced plasmon coupling in crossed dielectric/metal nanowire composite geometries and applications to surface-enhanced Raman spectroscopy. *Appl Phys Lett* **2007,** *90* (9), 093105; (c) Prokes, S. M.; Alexson, D. A.; Glembocki, O. J.; Park, H. D.; Rendell, R. W., Effect of crossing geometry on the plasmonic behavior of dielectric core/metal sheath nanowires. *Appl Phys Lett* **2009,** *94* (9), 093105; (d) Xu, Z. C.; Hou, Y. L.; Sun, S. H., Magnetic core/shell Fe_3O_4/Au and Fe_3O_4/Au/Ag nanoparticles with tunable plasmonic properties. *J. Am. Chem. Soc* **2007,** *129* (28), 8698-8699; (e) Wang, C.; Peng, S.; Chan, R.; Sun, S. H., Synthesis of AuAg Alloy Nanoparticles from Core/Shell-Structured Ag/Au. *Small* **2009,** *5* (5), 567-570.

38. (a) Sharma, B.; Fernanda Cardinal, M.; Kleinman, S. L.; Greeneltch, N. G.; Frontiera, R. R.; Blaber, M. G.; Schatz, G. C.; Van Duyne, R. P., High-performance SERS substrates: Advances and challenges. *Mrs Bull* **2013,** *38* (08), 615-624; (b) Zhu, W. L.; Michalsky, R.; Metin, O.; Lv, H. F.; Guo, S. J.; Wright, C. J.; Sun, X. L.; Peterson, A. A.; Sun, S. H., Monodisperse Au Nanoparticles for Selective Electrocatalytic Reduction of CO_2 to CO. *J. Am. Chem. Soc* **2013,** *135* (45), 16833-16836.

39. Michaels, A. M.; Jiang, J.; Brus, L., Ag nanocrystal junctions as the site for surface-enhanced Raman scattering of single Rhodamine 6G molecules. *J Phys Chem B* **2000,** *104* (50), 11965-11971.

40. (a) Wang, H. L.; Schaefer, K.; Moeller, M., In situ immobilization of gold nanoparticle dimers in silica nanoshell by microemulsion coalescence. *J Phys Chem C*

2008, *112* (9), 3175-3178; (b) Wang, X. J.; Li, G. P.; Chen, T.; Yang, M. X.; Zhang, Z.; Wu, T.; Chen, H. Y., Polymer-encapsulated gold-nanoparticle dimers: Facile preparation and catalytical application in guided growth of dimeric ZnO-nanowires. *Nano Lett* **2008,** *8* (9), 2643-2647; (c) Pazos-Perez, N.; Wagner, C. S.; Romo-Herrera, J. M.; Liz-Marzan, L. M.; de Abajo, F. J. G.; Wittemann, A.; Fery, A.; Alvarez-Puebla, R. A., Organized Plasmonic Clusters with High Coordination Number and Extraordinary Enhancement in Surface-Enhanced Raman Scattering (SERS). *Angew. Chem. Int. Ed.* **2012,** *51* (51), 12688-12693.

41. Cong, V. T.; Ganbold, E. O.; Saha, J. K.; Jang, J.; Min, J.; Choo, J.; Kim, S.; Song, N. W.; Son, S. J.; Lee, S. B.; Joo, S. W., Gold Nanoparticle Silica Nanopeapods. *J. Am. Chem. Soc* **2014,** *136* (10), 3833-3841.

42. Kang, H.; Jeong, S.; Park, Y.; Yim, J.; Jun, B. H.; Kyeong, S.; Yang, J. K.; Kim, G.; Hong, S.; Lee, L. P.; Kim, J. H.; Lee, H. Y.; Jeong, D. H.; Lee, Y. S., Near-Infrared SERS Nanoprobes with Plasmonic Au/Ag Hollow-Shell Assemblies for In Vivo Multiplex Detection. *Adv Funct Mater* **2013,** *23* (30), 3719-3727.

43. Li, J. F.; Huang, Y. F.; Ding, Y.; Yang, Z. L.; Li, S. B.; Zhou, X. S.; Fan, F. R.; Zhang, W.; Zhou, Z. Y.; Wu, D. Y.; Ren, B.; Wang, Z. L.; Tian, Z. Q., Shell-isolated nanoparticle-enhanced Raman spectroscopy. *Nature* **2010,** *464* (7287), 392-395.

44. Ayala-Orozco, C.; Liu, J. G.; Knight, M. W.; Wang, Y. M.; Day, J. K.; Nordlander, P.; Halas, N. J., Fluorescence Enhancement of Molecules Inside a Gold Nanomatryoshka. *Nano Lett* **2014,** *14* (5), 2926-2933.

45. (a) Oldenburg, S. J.; Averitt, R. D.; Westcott, S. L.; Halas, N. J., Nanoengineering of optical resonances. *Chem Phys Lett* **1998,** *288* (2-4), 243-247; (b) Jackson, J. B.; Halas, N. J., Silver Nanoshells: Variations in Morphologies and Optical Properties. *The Journal of Physical Chemistry B* **2001,** *105* (14), 2743-2746; (c) Prodan, E.; Nordlander, P., Structural Tunability of the Plasmon Resonances in Metallic Nanoshells. *Nano Lett* **2003,** *3* (4), 543-547.

46. (a) Xie, W.; Herrmann, C.; Kompe, K.; Haase, M.; Schlucker, S., Synthesis of Bifunctional Au/Pt/Au Core/Shell Nanoraspberries for in Situ SERS Monitoring of Platinum-Catalyzed Reactions. *J. Am. Chem. Soc* **2011,** *133* (48), 19302-19305; (b) Lee, J. P.; Chen, D. C.; Li, X. X.; Yoo, S.; Bottomley, L. A.; El-Sayed, M. A.; Park, S.; Liu, M. L., Well-organized raspberry-like Ag@Cu bimetal nanoparticles for highly reliable and reproducible surface-enhanced Raman scattering. *Nanoscale* **2013,** *5* (23), 11620-11624.

47. Zhang, L. F.; Zhong, S. L.; Xu, A. W., Highly Branched Concave Au/Pd Bimetallic Nanocrystals with Superior Electrocatalytic Activity and Highly Efficient SERS Enhancement. *Angew. Chem. Int. Ed.* **2013,** *52* (2), 645-649.

48. Yang, S. C.; Luo, X., Mesoporous nano/micro noble metal particles: synthesis and applications. *Nanoscale* **2014,** *6* (9), 4438-4457.

49. Xu, P.; Han, X. J.; Zhang, B.; Du, Y. C.; Wang, H. L., Multifunctional polymer-metal nanocomposites via direct chemical reduction by conjugated polymers. *Chem Soc Rev* **2014,** *43* (5), 1349-1360.

50. Hu, M.; Ou, F. S.; Wu, W.; Naumov, I.; Li, X.; Bratkovsky, A. M.; Williams, R. S.; Li, Z., Gold Nanofingers for Molecule Trapping and Detection. *J. Am. Chem. Soc* **2010,** *132* (37), 12820-12822.

51. Banholzer, M. J.; Qin, L. D.; Millstone, J. E.; Osberg, K. D.; Mirkin, C. A., On-wire lithography: synthesis, encoding and biological applications. *Nature Protocols* **2009,** *4* (6), 838-848.

52. Haynes, C. L.; Van Duyne, R. P., Nanosphere lithography: A versatile nanofabrication tool for studies of size-dependent nanoparticle optics. *J Phys Chem B* **2001,** *105* (24), 5599-5611.

53. Lim, D.-K.; Jeon, K.-S.; Hwang, J.-H.; Kim, H.; Kwon, S.; Suh, Y. D.; Nam, J.-M., Highly uniform and reproducible surface-enhanced Raman scattering from DNA-tailorable nanoparticles with 1-nm interior gap. *Nature Nanotech.* **2011,** *6* (7), 452-460.

54. Kühler, P.; Roller, E.-M.; Schreiber, R.; Liedl, T.; Lohmüller, T.; Feldmann, J., Plasmonic DNA-Origami Nanoantennas for Surface-Enhanced Raman Spectroscopy. *Nano Lett* **2014,** *14* (5), 2914-2919.

55. Huebner, U.; Schneidewind, H.; Cialla, D.; Weber, K.; Zeisberger, M.; Mattheis, R.; Moeller, R.; Popp, J., Fabrication of regular patterned SERS arrays by electron beam lithography. *Biophotonics: Photonic Solutions for Better Health Care Ii* **2010,** *7715*.

56. Gartia, M. R.; Xu, Z. D.; Behymer, E.; Nguyen, H.; Britten, J. A.; Larson, C.; Miles, R.; Bora, M.; Chang, A. S. P.; Bond, T. C.; Liu, G. L., Rigorous surface enhanced Raman

spectral characterization of large-area high-uniformity silver-coated tapered silica nanopillar arrays. *Nanotechnology* **2010,** *21* (39), 395701.

57. Chang, A. S. P.; Maiti, A.; Ileri, N.; Bora, M.; Larson, C. C.; Britten, J. A.; Bond, T. C. In *Detection of volatile organic compounds by surface enhanced Raman scattering*, Baltimore, Maryland, Baltimore, Maryland, 2012; pp 83660S-83660S-8.

58. Chou, S. Y.; Krauss, P. R.; Renstrom, P. J., Imprint lithography with 25-nanometer resolution. *Science* **1996,** *272* (5258), 85-87.

59. Ou, F. S.; Hu, M.; Naumov, I.; Kim, A.; Wu, W.; Bratkovsky, A. M.; Li, X.; Williams, R. S.; Li, Z., Hot-Spot Engineering in Polygonal Nanofinger Assemblies for Surface Enhanced Raman Spectroscopy. *Nano Lett* **2011,** *11* (6), 2538-2542.

60. Schmidt, M. S.; Hübner, J.; Boisen, A., Large Area Fabrication of Leaning Silicon Nanopillars for Surface Enhanced Raman Spectroscopy. *Adv Mater* **2012,** *24* (10), OP11-OP18.

61. Wang, D.; Zhu, W.; Best, M. D.; Camden, J. P.; Crozier, K. B., Wafer-scale metasurface for total power absorption, local field enhancement and single molecule Raman spectroscopy. *Sci. Rep.* **2013,** *3*, 2867.

62. (a) Jones, M. R.; Osberg, K. D.; Macfarlane, R. J.; Langille, M. R.; Mirkin, C. A., Templated techniques for the synthesis and assembly of plasmonic nanostructures. *Chem Rev* **2011,** *111* (6), 3736-827; (b) Qin, L. D.; Park, S.; Huang, L.; Mirkin, C. A., On-wire lithography. *Science* **2005,** *309* (5731), 113-115; (c) Qin, L. D.; Zou, S. L.; Xue, C.;

Atkinson, A.; Schatz, G. C.; Mirkin, C. A., Designing, fabricating, and imaging Raman hot spots. *P Natl Acad Sci USA* **2006,** *103* (36), 13300-13303.

63. Qin, L.; Banholzer, M. J.; Millstone, J. E.; Mirkin, C. A., Nanodisk Codes. *Nano Lett* **2007,** *7* (12), 3849-3853.

64. Banholzer, M. J.; Osberg, K. D.; Li, S.; Mangelson, B. F.; Schatz, G. C.; Mirkin, C. A., Silver-Based Nanodisk Codes. *ACS Nano* **2010,** *4* (9), 5446-5452.

65. (a) Lee, S. J.; Morrill, A. R.; Moskovits, M., Hot spots in silver nanowire bundles for surface-enhanced Raman spectroscopy. *J. Am. Chem. Soc* **2006,** *128* (7), 2200-2201; (b) Choi, D.; Choi, Y.; Hong, S.; Kang, T.; Lee, L. P., Self-Organized Hexagonal-Nanopore SERS Array. *Small* **2010,** *6* (16), 1741-1744.

66. Liu, G. L.; Lu, Y.; Kim, J.; Doll, J. C.; Lee, L. P., Magnetic Nanocrescents as Controllable Surface-Enhanced Raman Scattering Nanoprobes for Biomolecular Imaging. *Adv Mater* **2005,** *17* (22), 2683-2688.

67. Pilo-Pais, M.; Watson, A.; Demers, S.; LaBean, T. H.; Finkelstein, G., Surface-Enhanced Raman Scattering Plasmonic Enhancement Using DNA Origami-Based Complex Metallic Nanostructures. *Nano Lett* **2014,** *14* (4), 2099-2104.

68. Hermanson, K. D.; Lumsdon, S. O.; Williams, J. P.; Kaler, E. W.; Velev, O. D., Dielectrophoretic assembly of electrically functional microwires from nanoparticle suspensions. *Science* **2001,** *294* (5544), 1082-1086.

69. (a) Zhao, C. L.; Yang, C., Advances in electrokinetics and their applications in micro/nano fluidics. *Microfluid Nanofluid* **2012,** *13* (2), 179-203; (b) Ramos, A.; Morgan, H.; Green, N. G.; Castellanos, A., AC electric-field-induced fluid flow in microelectrodes. *J Colloid Interf Sci* **1999,** *217* (2), 420-422.

70. (a) Weber, K.; Osborn, M., Reliability of Molecular Weight Determinations by Dodecyl Sulfate-Polyacrylamide Gel Electrophoresis. *J Biol Chem* **1969,** *244* (16), 4406-4412; (b) Southern, E. M., Detection of Specific Sequences among DNA Fragments Separated by Gel-Electrophoresis. *J Mol Biol* **1975,** *98* (3), 503-517.

71. Gascoyne, P. R. C.; Vykoukal, J., Particle separation by dielectrophoresis. *Electrophoresis* **2002,** *23* (13), 1973-1983.

72. Haeberle, S.; Zengerle, R., Microfluidic platforms for lab-on-a-chip applications. *Lab Chip* **2007,** *7* (9), 1094-1110.

73. Pohl, H. A., The Motion and Precipitation of Suspensoids in Divergent Electric Fields. *J Appl Phys* **1951,** *22* (7), 869-871.

74. (a) Fiedler, S.; Shirley, S. G.; Schnelle, T.; Fuhr, G., Dielectrophoretic sorting of particles and cells in a microsystem. *Anal Chem* **1998,** *70* (9), 1909-1915; (b) Gascoyne, P. R. C.; Wang, X. B.; Huang, Y.; Becker, F. F., Dielectrophoretic separation of cancer cells from blood. *Ieee T Ind Appl* **1997,** *33* (3), 670-678.

75. (a) Cummings, E. B.; Singh, A. K., Dielectrophoresis in microchips containing arrays of insulating posts: Theoretical and experimental results. *Anal Chem* **2003,** *75* (18),

4724-4731; (b) Kang, Y. J.; Li, D. Q.; Kalams, S. A.; Eid, J. E., DC-Dielectrophoretic separation of biological cells by size. *Biomed Microdevices* **2008,** *10* (2), 243-249.

76. (a) Hawkins, B. G.; Smith, A. E.; Syed, Y. A.; Kirby, B. J., Continuous-flow particle separation by 3D insulative dielectrophoresis using coherently shaped, dc-biased, ac electric fields. *Anal Chem* **2007,** *79* (19), 7291-7300; (b) Zellner, P.; Shake, T.; Hosseini, Y.; Nakidde, D.; Riquelme, M. V.; Sahari, A.; Pruden, A.; Behkam, B.; Agah, M., 3D Insulator-based dielectrophoresis using DC-biased, AC electric fields for selective bacterial trapping. *Electrophoresis* **2015,** *36* (2), 277-283.

77. (a) Morgan, H.; Green, N. G.; Hughes, M. P.; Monaghan, W.; Tan, T. C., Large-area travelling-wave dielectrophoresis particle separator. *J Micromech Microeng* **1997,** *7* (2), 65-70; (b) Cheng, I. F.; Froude, V. E.; Zhu, Y. X.; Chang, H. C.; Chang, H. C., A continuous high-throughput bioparticle sorter based on 3D traveling-wave dielectrophoresis. *Lab Chip* **2009,** *9* (22), 3193-3201.

78. Jones, T. B., *Electromechanics of particles*. Digitally printed 1st pbk. ed.; Cambridge University Press: Cambridge ; New York, 2005; p xxii, 265 p.

79. (a) Lapizco-Encinas, B. H.; Simmons, B. A.; Cummings, E. B.; Fintschenko, Y., Dielectrophoretic concentration and separation of live and dead bacteria in an array of insulators. *Anal Chem* **2004,** *76* (6), 1571-1579; (b) Pethig, R.; Talary, M. S., Dielectrophoretic detection of membrane morphology changes in Jurkat T-cells undergoing etoposide-induced apoptosis. *Iet Nanobiotechnol* **2007,** *1* (1), 2-9.

80. Pethig, R., Dielectrophoresis: An assessment of its potential to aid the research and practice of drug discovery and delivery. *Adv Drug Deliver Rev* **2013,** *65* (11-12), 1589-1599.

81. Suehiro, J.; Hamada, R.; Noutomi, D.; Shutou, M.; Hara, M., Selective detection of viable bacteria using dielectrophoretic impedance measurement method. *J Electrostat* **2003,** *57* (2), 157-168.

82. Morgan, H.; Hughes, M. P.; Green, N. G., Separation of submicron bioparticles by dielectrophoresis. *Biophys J* **1999,** *77* (1), 516-525.

83. Ermolina, I.; Milner, J.; Morgan, H., Dielectrophoretic investigation of plant virus particles: Cow Pea Mosaic Virus and Tobacco Mosaic Virus. *Electrophoresis* **2006,** *27* (20), 3939-3948.

84. (a) Sonnenberg, A.; Marciniak, J. Y.; Krishnan, R.; Heller, M. J., Dielectrophoretic isolation of DNA and nanoparticles from blood. *Electrophoresis* **2012,** *33* (16), 2482-2490; (b) Chou, C. F.; Tegenfeldt, J. O.; Bakajin, O.; Chan, S. S.; Cox, E. C.; Darnton, N.; Duke, T.; Austin, R. H., Electrodeless dielectrophoresis of single- and double-stranded DNA. *Biophys J* **2002,** *83* (4), 2170-2179.

85. (a) Lapizco-Encinas, B. H.; Ozuna-Chacon, S.; Rito-Palomares, M., Protein manipulation with insulator-based dielectrophoresis and direct current electric fields. *J Chromatogr A* **2008,** *1206* (1), 45-51; (b) Nakano, A.; Chao, T. C.; Camacho-Alanis, F.;

Ros, A., Immunoglobulin G and bovine serum albumin streaming dielectrophoresis in a microfluidic device. *Electrophoresis* **2011,** *32* (17), 2314-2322.

86. Yunus, N. A. M.; Nili, H.; Green, N. G., Continuous separation of colloidal particles using dielectrophoresis. *Electrophoresis* **2013,** *34* (7), 969-978.

87. Lewpiriyawong, N.; Yang, C.; Lam, Y. C., Continuous sorting and separation of microparticles by size using AC dielectrophoresis in a PDMS microfluidic device with 3-D conducting PDMS composite electrodes. *Electrophoresis* **2010,** *31* (15), 2622-2631.

88. Edwards, T. D.; Bevan, M. A., Controlling Colloidal Particles with Electric Fields. *Langmuir* **2014,** *30* (36), 10793-10803.

89. Reuss, F. F., Sur un nouvel effet de l'électricité galvanique. *Mem. Soc. Imp. Natur. Moscou* **1809,** *2*, 327-337.

90. Helmholtz, H. v., Ueber einige Gesetze der Vertheilung elektrischer Ströme in körperlichen Leitern mit Anwendung auf die thierisch-elektrischen Versuche. *Annalen der Physik* **1853,** *165* (6), 211-233.

91. Gouy, G., Sur la constitution de la charge electrique a la surface d’un electrolyte. *J. phys* **1910,** *9* (4), 457-468.

92. Chapman, D. L., A Contribution to the Theory of Electrocapillarity. *Philos Mag* **1913,** *25* (148), 475-481.

93. Stern, O., Zur theorie der elektrolytischen doppelschicht. *Zeitschrift für Elektrochemie und angewandte physikalische Chemie* **1924,** *30* (21-22), 508-516.

94. Probstein, R. F., *Physicochemical hydrodynamics : an introduction*. 2nd ed.; Wiley: New York, 1994; p xv, 400 p.

95. (a) Green, N. G.; Ramos, A.; Gonzalez, A.; Morgan, H.; Castellanos, A., Fluid flow induced by nonuniform ac electric fields in electrolytes on microelectrodes. I. Experimental measurements. *Phys Rev E* **2000,** *61* (4), 4011-4018; (b) Gonzalez, A.; Ramos, A.; Green, N. G.; Castellanos, A.; Morgan, H., Fluid flow induced by nonuniform ac electric fields in electrolytes on microelectrodes. II. A linear double-layer analysis. *Phys Rev E* **2000,** *61* (4), 4019-4028; (c) Green, N. G.; Ramos, A.; Gonzalez, A.; Morgan, H.; Castellanos, A., Fluid flow induced by nonuniform ac electric fields in electrolytes on microelectrodes. III. Observation of streamlines and numerical simulation. *Phys Rev E* **2002,** *66* (2).

96. Li, D., *Encyclopedia of microfluidics and nanofluidics*. Springer: New York, 2008.

97. Ajdari, A., Pumping liquids using asymmetric electrode arrays. *Phys Rev E* **2000,** *61* (1), R45-R48.

98. Brown, A. B. D.; Smith, C. G.; Rennie, A. R., Pumping of water with ac electric fields applied to asymmetric pairs of microelectrodes. *Phys Rev E* **2001,** *63* (1).

99. Mpholo, M.; Smith, C. G.; Brown, A. B. D., Low voltage plug flow pumping using anisotropic electrode arrays. *Sensor Actuat B-Chem* **2003,** *92* (3), 262-268.

100. Wu, J., ac electro-osmotic micropump by asymmetric electrode polarization. *J Appl Phys* **2008,** *103* (2).

101. Ng, W. Y.; Goh, S.; Lam, Y. C.; Yang, C.; Rodriguez, I., DC-biased AC-electroosmotic and AC-electrothermal flow mixing in microchannels. *Lab Chip* **2009,** *9* (6), 802-809.

102. Wu, J.; Ben, Y. X.; Battigelli, D.; Chang, H. C., Long-range AC electroosmotic trapping and detection of bioparticles. *Ind Eng Chem Res* **2005,** *44* (8), 2815-2822.

103. Huang, M. H.; Mao, S.; Feick, H.; Yan, H. Q.; Wu, Y. Y.; Kind, H.; Weber, E.; Russo, R.; Yang, P. D., Room-temperature ultraviolet nanowire nanolasers. *Science* **2001,** *292* (5523), 1897-1899.

104. Kong, X. Y.; Ding, Y.; Yang, R.; Wang, Z. L., Single-crystal nanorings formed by epitaxial self-coiling of polar nanobelts. *Science* **2004,** *303* (5662), 1348-1351.

105. Zhang, H. J.; Wu, D. H.; Tang, Q.; Liu, L.; Zhou, Z., ZnO-GaN heterostructured nanosheets for solar energy harvesting: computational studies based on hybrid density functional theory. *J Mater Chem A* **2013,** *1* (6), 2231-2237.

106. (a) Shen, G.; Bando, Y.; Lee, C. J., Growth of self-organized hierarchical ZnO nanoarchitectures by a simple In/In2S3 controlled thermal evaporation process. *J Phys Chem B* **2005,** *109* (21), 10779-10785; (b) Lu, F.; Cai, W. P.; Zhang, Y. G., ZnO hierarchical micro/nanoarchitectures: Solvothermal synthesis and structurally enhanced photocatalytic performance. *Adv Funct Mater* **2008,** *18* (7), 1047-1056; (c) Xu, X. B.; Wu, M.; Asoro, M.; Ferreira, P. J.; Fan, D. L., One-Step Hydrothermal Synthesis of Comb-Like ZnO Nanostructures. *Cryst Growth Des* **2012,** *12* (10), 4829-4833.

107. (a) Sounart, T. L.; Liu, J.; Voigt, J. A.; Huo, M.; Spoerke, E. D.; McKenzie, B., Secondary nucleation and growth of ZnO. *J Am Chem Soc* **2007,** *129* (51), 15786-15793; (b) Vayssieres, L., Growth of arrayed nanorods and nanowires of ZnO from aqueous solutions. *Adv Mater* **2003,** *15* (5), 464-466; (c) Ko, S. H.; Lee, D.; Kang, H. W.; Nam, K. H.; Yeo, J. Y.; Hong, S. J.; Grigoropoulos, C. P.; Sung, H. J., Nanoforest of Hydrothermally Grown Hierarchical ZnO Nanowires for a High Efficiency Dye-Sensitized Solar Cell. *Nano Lett* **2011,** *11* (2), 666-671.

108. Sun, K.; Jing, Y.; Li, C.; Zhang, X.; Aguinaldo, R.; Kargar, A.; Madsen, K.; Banu, K.; Zhou, Y.; Bando, Y.; Liu, Z.; Wang, D., 3D branched nanowire heterojunction photoelectrodes for high-efficiency solar water splitting and H_2 generation. *Nanoscale* **2012,** *4* (5), 1515-21.

109. (a) Zhang, T. R.; Dong, W. J.; Keeter-Brewer, M.; Konar, S.; Njabon, R. N.; Tian, Z. R., Site-specific nucleation and growth kinetics in hierarchical nanosyntheses of branched ZnO crystallites. *J Am Chem Soc* **2006,** *128* (33), 10960-10968; (b) Lao, J. Y.; Wen, J. G.; Ren, Z. F., Hierarchical ZnO nanostructures. *Nano Lett* **2002,** *2* (11), 1287-1291; (c) Doerk, G. S.; Ferralis, N.; Carraro, C.; Maboudian, R., Growth of branching Si nanowires seeded by Au-Si surface migration. *J Mater Chem* **2008,** *18* (44), 5376-5381; (d) Sun, K.; Jing, Y.; Park, N.; Li, C.; Bando, Y.; Wang, D. L., Solution Synthesis of Large-Scale, High-Sensitivity ZnO/Si Hierarchical Nanoheterostructure Photodetectors. *J. Am. Chem. Soc* **2010,** *132* (44), 15465-15467.

110. Sugavaneshwar, R. P.; Nanda, K. K., Uninterrupted and reusable source for the controlled growth of nanowires. *Sci Rep-Uk* **2013,** *3*, 1172

111. Mazeina, L.; Picard, Y. N.; Prokes, S. M., Controlled Growth of Parallel Oriented ZnO Nanostructural Arrays on Ga_2O_3 Nanowires. *Cryst Growth Des* **2009,** *9* (2), 1164-1169.

112. (a) Chen, C. C.; Yeh, C. C.; Chen, C. H.; Yu, M. Y.; Liu, H. L.; Wu, J. J.; Chen, K. H.; Chen, L. C.; Peng, J. Y.; Chen, Y. F., Catalytic growth and characterization of gallium nitride nanowires. *J. Am. Chem. Soc* **2001,** *123* (12), 2791-2798; (b) Johnson, J. C.; Choi, H. J.; Knutsen, K. P.; Schaller, R. D.; Yang, P. D.; Saykally, R. J., Single gallium nitride nanowire lasers. *Nat Mater* **2002,** *1* (2), 106-110; (c) Morales, A. M.; Lieber, C. M., A laser ablation method for the synthesis of crystalline semiconductor nanowires. *Science* **1998,** *279* (5348), 208-211.

113. (a) Borchers, C.; Muller, S.; Stichtenoth, D.; Schwen, D.; Ronning, C., Catalyst-nanostructure interaction in the growth of 1-D ZnO nanostructures. *J Phys Chem B* **2006,** *110* (4), 1656-1660; (b) Song, J. H.; Wang, X. D.; Riedo, E.; Wang, Z. L., Systematic study on experimental conditions for large-scale growth of aligned ZnO nanwires on nitrides. *J Phys Chem B* **2005,** *109* (20), 9869-9872; (c) Chik, H.; Liang, J.; Cloutier, S. G.; Kouklin, N.; Xu, J. M., Periodic array of uniform ZnO nanorods by second-order self-assembly. *Appl Phys Lett* **2004,** *84* (17), 3376-3378.

114. Fan, H. J.; Lee, W.; Hauschild, R.; Alexe, M.; Le Rhun, G.; Scholz, R.; Dadgar, A.; Nielsch, K.; Kalt, H.; Krost, A.; Zacharias, M.; Gosele, U., Template-assisted large-scale

ordered arrays of ZnO pillars for optical and piezoelectric applications. *Small* **2006,** *2* (4), 561-568.

115. Kirkham, M.; Wang, X. D.; Wang, Z. L.; Snyder, R. L., Solid Au nanoparticles as a catalyst for growing aligned ZnO nanowires: a new understanding of the vapour-liquid-solid process. *Nanotechnology* **2007,** *18* (36), 365304.

116. Campos, L. C.; Tonezzer, M.; Ferlauto, A. S.; Grillo, V.; Magalhaes-Paniago, R.; Oliveira, S.; Ladeira, L. O.; Lacerda, R. G., Vapor-solid-solid growth mechanism driven by epitaxial match between solid AuZn alloy catalyst particles and ZnO nanowires at low temperatures. *Adv Mater* **2008,** *20* (8), 1499-1504.

117. (a) Wang, X. D.; Summers, C. J.; Wang, Z. L., Large-scale hexagonal-patterned growth of aligned ZnO nanorods for nano-optoelectronics and nanosensor arrays. *Nano Lett* **2004,** *4* (3), 423-426; (b) Wang, X. D.; Song, J. H.; Li, P.; Ryou, J. H.; Dupuis, R. D.; Summers, C. J.; Wang, Z. L., Growth of uniformly aligned ZnO nanowire heterojunction arrays on GaN, AIN, and $Al_{0.5}Ga_{0.5}N$ substrates. *J. Am. Chem. Soc* **2005,** *127* (21), 7920-7923.

118. Zhang, Z.; Wang, S. J.; Yu, T.; Wu, T., Controlling the growth mechanism of ZnO nanowires by selecting catalysts. *J Phys Chem C* **2007,** *111* (47), 17500-17505.

119. Alonso, C.; Salvarezza, R. C.; Vara, J. M.; Arvia, A. J.; Vazquez, L.; Bartolome, A.; Baro, A. M., The Evaluation of Surface-Diffusion Coefficients of Gold and Platinum

Atoms at Electrochemical Interfaces from Combined STM-SEM Imaging and Electrochemical Techniques. *J Electrochem Soc* **1990,** *137* (7), 2161-2166.

120. Wang, H. Y.; Fischman, G. S., Role of Liquid Droplet Surface-Diffusion in the Vapor-Liquid-Solid Whisker Growth Mechanism. *J Appl Phys* **1994,** *76* (3), 1557-1562.

121. Ding, Y.; Kim, Y. J.; Erlebacher, J., Nanoporous gold leaf: "Ancient technology"/advanced material. *Adv Mater* **2004,** *16* (21), 1897-1900.

122. (a) Huang, Y.; Duan, X. F.; Cui, Y.; Lauhon, L. J.; Kim, K. H.; Lieber, C. M., Logic gates and computation from assembled nanowire building blocks. *Science* **2001,** *294* (5545), 1313-1317; (b) Cui, Y.; Wei, Q. Q.; Park, H. K.; Lieber, C. M., Nanowire nanosensors for highly sensitive and selective detection of biological and chemical species. *Science* **2001,** *293* (5533), 1289-1292; (c) Tian, B. Z.; Zheng, X. L.; Kempa, T. J.; Fang, Y.; Yu, N. F.; Yu, G. H.; Huang, J. L.; Lieber, C. M., Coaxial silicon nanowires as solar cells and nanoelectronic power sources. *Nature* **2007,** *449* (7164), 885-U8; (d) Qu, Y. Q.; Liao, L.; Li, Y. J.; Zhang, H.; Huang, Y.; Duan, X. F., Electrically Conductive and Optically Active Porous Silicon Nanowires. *Nano Lett* **2009,** *9* (12), 4539-4543.

123. (a) Hwang, Y. J.; Boukai, A.; Yang, P. D., High Density n-Si/n-TiO2 Core/Shell Nanowire Arrays with Enhanced Photoactivity. *Nano Lett* **2009,** *9* (1), 410-415; (b) Hsieh, Y. P.; Chen, H. Y.; Lin, M. Z.; Shiu, S. C.; Hofmann, M.; Chern, M. Y.; Jia, X. T.; Yang, Y. J.; Chang, H. J.; Huang, H. M.; Tseng, S. C.; Chen, L. C.; Chen, K. H.; Lin, C. F.; Liang, C. T.; Chen, Y. F., Electroluminescence from ZnO/Si-Nanotips Light-Emitting Diodes. *Nano Lett* **2009,** *9* (5), 1839-1843; (c) Zhong, Z. H.; Wang, D. L.; Cui, Y.; Bockrath, M.

W.; Lieber, C. M., Nanowire crossbar arrays as address decoders for integrated nanosystems. *Science* **2003,** *302* (5649), 1377-1379; (d) Hochbaum, A. I.; Chen, R. K.; Delgado, R. D.; Liang, W. J.; Garnett, E. C.; Najarian, M.; Majumdar, A.; Yang, P. D., Enhanced thermoelectric performance of rough silicon nanowires. *Nature* **2008,** *451* (7175), 163-U5.

124. Huang, Z. P.; Geyer, N.; Werner, P.; de Boor, J.; Gosele, U., Metal-Assisted Chemical Etching of Silicon: A Review. *Adv Mater* **2011,** *23* (2), 285-308.

125. Zhu, F. Q.; Fan, D. L.; Zhu, X. C.; Zhu, J. G.; Cammarata, R. C.; Chien, C. L., Ultrahigh-Density Arrays of ferromagnetic nanorings on macroscopic areas. *Adv Mater* **2004,** *16* (23-24), 2155-2159.

126. Chartier, C.; Bastide, S.; Levy-Clement, C., Metal-assisted chemical etching of silicon in HF-H_2O_2. *Electrochim Acta* **2008,** *53* (17), 5509-5516.

127. (a) Fan, D. L.; Cammarata, R. C.; Chien, C. L., Precision transport and assembling of nanowires in suspension by electric fields. *Appl Phys Lett* **2008,** *92* (9), 093115; (b) Xu, X. B.; Kim, K.; Li, H. F.; Fan, D. L., Ordered Arrays of Raman Nanosensors for Ultrasensitive and Location Predictable Biochemical Detection. *Adv Mater* **2012,** *24* (40), 5457-5463.

128. Xu, X. B.; Li, H. F.; Hasan, D.; Ruoff, R. S.; Wang, A. X.; Fan, D. L., Near-Field Enhanced Plasmonic-Magnetic Bifunctional Nanotubes for Single Cell Bioanalysis. *Adv Funct Mater* **2013,** *23* (35), 4332-4338.

129. Xu, X. B.; Hasan, D. H.; Wang, L.; Chakravarty, S.; Chen, R. T.; Fan, D. L.; Wang, A. X., Guided-mode-resonance-coupled plasmonic-active SiO2 nanotubes for surface enhanced Raman spectroscopy (vol 100, 191114, 2012). *Appl Phys Lett* **2012,** *101* (5), 191114.

130. (a) Gao, X. H.; Cui, Y. Y.; Levenson, R. M.; Chung, L. W. K.; Nie, S. M., In vivo cancer targeting and imaging with semiconductor quantum dots. *Nat Biotechnol* **2004,** *22* (8), 969-976; (b) Chan, W. C. W.; Nie, S. M., Quantum dot bioconjugates for ultrasensitive nonisotopic detection. *Science* **1998,** *281* (5385), 2016-2018.

131. Zhang, C. Y.; Yeh, H. C.; Kuroki, M. T.; Wang, T. H., Single-quantum-dot-based DNA nanosensor. *Nat Mater* **2005,** *4* (11), 826-31.

132. (a) Chen, H. H.; Ho, Y. P.; Jiang, X.; Mao, H. Q.; Wang, T. H.; Leong, K. W., Quantitative comparison of intracellular unpacking kinetics of polyplexes by a model constructed from quantum Dot-FRET. *Mol Ther* **2008,** *16* (2), 324-332; (b) Grigsby, C. L.; Ho, Y. P.; Leong, K. W., Understanding nonviral nucleic acid delivery with quantum dot-FRET nanosensors. *Nanomedicine-Uk* **2012,** *7* (4), 565-577.

133. Cai, W. B.; Hsu, A. R.; Li, Z. B.; Chen, X. Y., Are quantum dots ready for in vivo imaging in human subjects? *Nanoscale Res Lett* **2007,** *2* (6), 265-281.

134. Medintz, I. L.; Clapp, A. R.; Brunel, F. M.; Tiefenbrunn, T.; Uyeda, H. T.; Chang, E. L.; Deschamps, J. R.; Dawson, P. E.; Mattoussi, H., Proteolytic activity monitored by

fluorescence resonance energy transfer through quantum-dot-peptide conjugates. *Nat Mater* **2006,** *5* (7), 581-9.

135. Fan, D. L.; Zhu, F. Q.; Cammarata, R. C.; Chien, C. L., Efficiency of assembling of nanowires in suspension by ac electric fields. *Appl Phys Lett* **2006,** *89* (22).

136. Pohl, H. A., *Dielectrophoresis : the behavior of neutral matter in nonuniform electric fields*. Cambridge University Press: Cambridge ; New York, 1978; p xii, 579 p.

137. Jones, T. B., *Electromechanics of particles*. Cambridge University Press: Cambridge ; New York, 1995; p xxii, 265 p.

138. Fan, D. L.; Zhu, F. Q.; Cammarata, R. C.; Chien, C. L., Manipulation of nanowires in suspension by ac electric fields. *Appl Phys Lett* **2004,** *85* (18), 4175-4177.

139. Kim, K.; Zhu, F. Q.; Fan, D. L., Innovative Mechanisms for Precision Assembly and Actuation of Arrays of Nanowire Oscillators. *ACS Nano* **2013,** *7* (4), 3476-3483.

140. Sin, M. L. Y.; Gau, V.; Liao, J. C.; Haake, D. A.; Wong, P. K., Active Manipulation of Quantum Dots using AC Electrokinetics. *J Phys Chem C* **2009,** *113* (16), 6561-6565.

141. Castellanos, A.; Ramos, A.; Gonzalez, A.; Green, N. G.; Morgan, H., Electrohydrodynamics and dielectrophoresis in microsystems: scaling laws. *J Phys D Appl Phys* **2003,** *36* (20), 2584-2597.

142. (a) Huang, C. C.; Bazant, M. Z.; Thorsen, T., Ultrafast high-pressure AC electro-osmotic pumps for portable biomedical microfluidics. *Lab Chip* **2010,** *10* (1), 80-85; (b) Bazant, M. Z.; Ben, Y. X., Theoretical prediction of fast 3D AC electro-osmotic pumps.

Lab Chip **2006,** *6* (11), 1455-1461; (c) Debesset, S.; Hayden, C. J.; Dalton, C.; Eijkel, J. C. T.; Manz, A., An AC electroosmotic micropump for circular chromatographic applications. *Lab Chip* **2004,** *4* (4), 396-400.

143. Dulkeith, E.; Morteani, A. C.; Niedereichholz, T.; Klar, T. A.; Feldmann, J.; Levi, S. A.; van Veggel, F.; Reinhoudt, D. N.; Moller, M.; Gittins, D. I., Fluorescence quenching of dye molecules near gold nanoparticles: Radiative and nonradiative effects. *Phys Rev Lett* **2002,** *89* (20).

144. Li, M. W.; Bhiladvala, R. B.; Morrow, T. J.; Sioss, J. A.; Lew, K. K.; Redwing, J. M.; Keating, C. D.; Mayer, T. S., Bottom-up assembly of large-area nanowire resonator arrays. *Nature Nanotech.* **2008,** *3* (2), 88-92.

145. Liu, C.; Zhang, P. F.; Kim, K.; Werner, J. H.; Fan, D. L., Coupling and Fluorescent Enhancement of Semiconductor Nanoemitters on the Tips of Plasmonic Nanoantennas. In preparation.

146. Niemeyer, C. M., *Bioconjugation protocols: strategies and methods*. Springer: 2004; Vol. 283.

147. (a) Lidke, D. S.; Nagy, P.; Heintzmann, R.; Arndt-Jovin, D. J.; Post, J. N.; Grecco, H. E.; Jares-Erijman, E. A.; Jovin, T. M., Quantum dot ligands provide new insights into erbB/HER receptor-mediated signal transduction. *Nat Biotechnol* **2004,** *22* (2), 198-203; (b) Lieleg, O.; Lopez-Garcia, M.; Semmrich, C.; Auernheimer, J.; Kessler, H.; Bausch, A.

R., Specific Integrin Labeling in Living Cells Using Functionalized Nanocrystals. *Small* **2007,** *3* (9), 1560-1565.

148. Sheehan, P. E.; Whitman, L. J., Detection limits for nanoscale biosensors. *Nano Lett* **2005,** *5* (4), 803-807.

149. (a) Rouabah, H. A.; Park, B. Y.; Zaouk, R. B.; Morgan, H.; Madou, M. J.; Green, N. G., Design and fabrication of an ac-electro-osmosis micropump with 3D high-aspect-ratio electrodes using only SU-8. *J Micromech Microeng* **2011,** *21* (3), 035018; (b) Martinez-Duarte, R.; Gorkin III, R. A.; Abi-Samra, K.; Madou, M. J., The integration of 3D carbon-electrode dielectrophoresis on a CD-like centrifugal microfluidic platform. *Lab Chip* **2010,** *10* (8), 1030-1043.

150. Barhoumi, A.; Halas, N. J., Label-Free Detection of DNA Hybridization Using Surface Enhanced Raman Spectroscopy. *J. Am. Chem. Soc* **2010,** *132* (37), 12792-12793.

151. Alvarez-Puebla, R. A.; Dos Santos, D. S.; Aroca, R. F., SERS detection of environmental pollutants in humic acid-gold nanoparticle composite materials. *Analyst* **2007,** *132* (12), 1210-1214.

152. (a) Chou, A.; Jaatinen, E.; Buividas, R.; Seniutinas, G.; Juodkazis, S.; Izake, E. L.; Fredericks, P. M., SERS substrate for detection of explosives. *Nanoscale* **2012,** *4* (23), 7419-7424; (b) Demeritte, T.; Kanchanapally, R.; Fan, Z.; Singh, A. K.; Senapati, D.; Dubey, M.; Zakar, E.; Ray, P. C., Highly efficient SERS substrate for direct detection of

explosive TNT using popcorn-shaped gold nanoparticle-functionalized SWCNT hybrid. *Analyst* **2012,** *137* (21), 5041-5045.

153. Tao, A.; Kim, F.; Hess, C.; Goldberger, J.; He, R.; Sun, Y.; Xia, Y.; Yang, P., Langmuir-Blodgett silver nanowire monolayers for molecular sensing using surface-enhanced Raman spectroscopy. *Nano Lett* **2003,** *3* (9), 1229-1233.

154. (a) Wang, Y. L.; Lee, K.; Irudayaraj, J., Silver Nanosphere SERS Probes for Sensitive Identification of Pathogens. *J Phys Chem C* **2010,** *114* (39), 16122-16128; (b) Chon, H.; Lee, S.; Son, S. W.; Oh, C. H.; Choo, J., Highly Sensitive Immunoassay of Lung Cancer Marker Carcinoembryonic Antigen Using Surface-Enhanced Raman Scattering of Hallow Gold Nanospheres. *Anal Chem* **2009,** *81* (8), 3029-3034.

155. (a) Stockle, R. M.; Suh, Y. D.; Deckert, V.; Zenobi, R., Nanoscale chemical analysis by tip-enhanced Raman spectroscopy. *Chem Phys Lett* **2000,** *318* (1-3), 131-136; (b) Sonntag, M. D.; Klingsporn, J. M.; Garibay, L. K.; Roberts, J. M.; Dieringer, J. A.; Seideman, T.; Scheidt, K. A.; Jensen, L.; Schatz, G. C.; Van Duyne, R. P., Single-Molecule Tip-Enhanced Raman Spectroscopy. *J Phys Chem C* **2012,** *116* (1), 478-483.

156. Shen, A. G.; Chen, L. F.; Xie, W.; Hu, J. C.; Zeng, A.; Richards, R.; Hu, J. M., Triplex Au-Ag-C Core Shell Nanoparticles as a Novel Raman Label. *Adv Funct Mater* **2010,** *20* (6), 969-975.

157. Hughes, M. P., *Nanoelectromechanics in engineering and biology*. CRC Press: Boca Raton, 2003; p 322 p.

158. Barik, A.; Otto, L. M.; Yoo, D.; Jose, J.; Johnson, T. W.; Oh, S. H., Dielectrophoresis-Enhanced Plasmonic Sensing with Gold Nanohole Arrays. *Nano Lett* **2014,** *14* (4), 2006-2012.

159. Deng, Y. L.; Juang, Y. J., Electrokinetic trapping and surface enhanced Raman scattering detection of biomolecules using optofluidic device integrated with a microneedles array. *Biomicrofluidics* **2013,** *7* (1), 014111.

160. Park, M.; Oh, Y.-J.; Jeong, K.-H. In *Electrophoretic preconcentration on plasmonic nanopillar arrays for highly intense surface-enhanced Raman scattering*, Solid-State Sensors, Actuators and Microsystems (TRANSDUCERS & EUROSENSORS XXVII), 2013 Transducers & Eurosensors XXVII: The 17th International Conference on, IEEE: 2013; pp 1803-1806.

161. Cherukulappurath, S.; Lee, S. H.; Campos, A.; Haynes, C. L.; Oh, S.-H., Rapid and sensitive in situ SERS detection using dielectrophoresis. *Chem Mater* **2014,** *26* (7), 2445-2452.

162. Smith, B. D.; Mayer, T. S.; Keating, C. D., Deterministic Assembly of Functional Nanostructures Using Nonuniform Electric Fields. *Annu Rev Phys Chem* **2012,** *63*, 241-263.

163. Cheng, I.-F.; Chen, T.-Y.; Lu, R.-J.; Wu, H.-W., Rapid identification of bacteria utilizing amplified dielectrophoretic force-assisted nanoparticle-induced surface-enhanced Raman spectroscopy. *Nanoscale Res Lett* **2014,** *9* (1), 1-8.

164. Liu, C.; Kim, K.; Fan, D. L., Location deterministic biosensing from quantum-dot-nanowire assemblies. *Appl Phys Lett* **2014,** *105* (8), 083123.

165. Zengin, A.; Tamer, U.; Caykara, T., A SERS-Based Sandwich Assay for Ultrasensitive and Selective Detection of Alzheimer's Tau Protein. *Biomacromolecules* **2013,** *14* (9), 3001-3009.

166. Xu, X. B.; Hasan, D. H.; Wang, L.; Chakravarty, S.; Chen, R. T.; Fan, D. L.; Wang, A. X., Guided-mode-resonance-coupled plasmonic-active SiO_2 nanotubes for surface enhanced Raman spectroscopy. *Appl Phys Lett* **2012,** *100* (19), 191114.

167. Liu, C.; Kim, K.; Fan, D. L., Location deterministic biosensing from quantum-dot-nanowire assemblies. *Appl Phys Lett* **2014,** *105* (8).